

Electronic Thesis and Dissertation Repository

4-28-2015 12:00 AM

Force Sensing in Arthroscopic Instruments using Fiber Bragg Gratings

Daniel S. Yurkewich, *The University of Western Ontario*

Supervisor: Dr. Patel, *The University of Western Ontario*

Joint Supervisor: Dr. Naish, *The University of Western Ontario*

A thesis submitted in partial fulfillment of the requirements for the Master of Engineering Science degree in Electrical and Computer Engineering

© Daniel S. Yurkewich 2015

Follow this and additional works at: <https://ir.lib.uwo.ca/etd>



Part of the [Biomechanical Engineering Commons](#), [Biomedical Commons](#), [Biomedical Devices and Instrumentation Commons](#), [Electrical and Electronics Commons](#), and the [Signal Processing Commons](#)

Recommended Citation

Yurkewich, Daniel S., "Force Sensing in Arthroscopic Instruments using Fiber Bragg Gratings" (2015). *Electronic Thesis and Dissertation Repository*. 2857.
<https://ir.lib.uwo.ca/etd/2857>

This Dissertation/Thesis is brought to you for free and open access by Scholarship@Western. It has been accepted for inclusion in Electronic Thesis and Dissertation Repository by an authorized administrator of Scholarship@Western. For more information, please contact wlsadmin@uwo.ca.

FORCE SENSING IN ARTHROSCOPIC INSTRUMENTS USING FIBER BRAGG GRATINGS

(Spine title: Force Sensing in Arthroscopic Instruments using Fiber Bragg Gratings)

(Thesis format: Monograph)

by

Daniel S. Yurkewich

Graduate Program in Engineering Science

Department of Electrical and Computer Engineering

Submitted in partial fulfillment

of the requirements for the degree of

Masters of Engineering Science

Faculty of Graduate Studies

The University of Western Ontario

London, Ontario, Canada

© Copyright by Daniel Scott Yurkewich 2015

Abstract

Minimally-invasive surgery has revolutionized many medical procedures; however, it also impedes the ability to feel the interaction between the surgical tool and the anatomical part being operated on. In order to address this problem, it is necessary to obtain accurate measurements of the interaction forces exerted on the surgical tools during surgery. These forces can then be manifested to the surgeon via a haptic device or presented visually (visual-force feedback). This thesis describes the use of a fiber optic device to measure and display to the surgeon interaction forces acting on an arthroscopic tool. The sensorization of the tool involves a simple, highly efficient and robust design and is ideally suited for use in a surgical training environment aimed at narrowing the gap between trainees and expert surgeons before the trainees proceed to their first surgery *in vivo*. The major advantages of using fiber optics include their small size, their local simplicity, their ease of sterilization, and their high sensitivity. In this thesis, a complete low-cost sensing solution is described, including 1) the use of fiber Bragg grating and long period grating sensors, 2) design of a low-cost optical interrogator, 3) high resolution electronic signal processing, and 4) fabrication of the tool using wire EDM, CNC, and 3D metal sintering technologies. The full design of an arthroscopic grasper is presented, along with the preliminary design and manufacturing of an arthroscopic probe and shaver. The designed low-cost system was compared with a commercially-available optical interrogator. The calibration and experimental results for this system are presented and discussed for accuracy and performance of the sensorized tool before and after an axial element was added for increased sensitivity. Sources of error and methods of improvement for the optical system, arthroscopic tool, and testing procedures are discussed to inform the design of future generations of these instruments.

Keywords: Bragg gratings, fiber optic, arthroscopic, minimally-invasive surgery, design, low-cost, force sensing

Acknowledgements

I have been privileged to become a part of the CSTAR team here at Western University, and to have the full support of our minimally invasive arthroscopy group composed of Dr. Rajni V. Patel, Dr. Michael Naish, Dr. Marie-Eve LeBel, Dr. Ana Luisa Trejos, and Abelardo Escoto. With their help, I was able to expand my thinking and designs to capture the full process behind developing an arthroscopic grasper capable of sensing minute tissue forces. Their mechanical knowledge on calibration, stress analysis, manufacturing and assembly; their medical knowledge on sterilization, tool performance, and surgical practices; and their expert help in reviewing and editing, helped my work reach recognized levels in the medical and engineering community.

This research was graciously supported financially by the Natural Sciences and Engineering Research Council (NSERC) of Canada under grants RGPIN-1345 and 312393-2010; by the Ontario Research Fund—Research Excellence Grant RE-05-049, and by infrastructure grants from the Canada Foundation for Innovation awarded to the London Health Sciences Centre (Canadian Surgical Technologies & Advanced Robotics (CSTAR)). Similarly, technical and administrative support from all of the staff at CSTAR and in the Electrical and Computer Engineering department was key to building and maintaining the structure of this degree.

Excellent technical company support was given by Thorlabs, National Instruments, and Micron Optics for fiber optic specifications and design, and by MicroGroup for detailed specifications on their hypodermic stainless steel tubing. I would also like to acknowledge the vendors used for each of the various low-cost products that make up this complete system described below: OSHPark (printed circuit boards), Thorlabs (SLD broadband source), Micron Optics (FBG sensors), Texas Instruments (ADC samples), Newfocus (circulators), Newport (Splitter), and Digikey (Electrical components).

Abelardo (Abe) Escoto and Chris Ward were two of the many supportive students and research assistants at CSTAR. With his training, Abe helped a lot on the EDM machine, cutting out and fine tuning complex incisions. He had great design ideas, augmented by the thorough knowledge he had of all the other MIS work previously done in the lab. Abe helped me stay on track, and

kept me focused on always moving forward. Chris was always prepared to pause his own work and provide 100% of his attention to all of my never-ending questions. He helped me many times on debugging my coding errors, and always had an answer for my electrical struggles. Both Chris and Abe also put in a lot of time and work on micromachining the sensor slots at the initial phase of the project. Together, they are any lab's dream team.

I would like to thank everyone at the University Machine Shop for their help in using the EDM, and for advice throughout the years. I would also like to thank Hristo Nikolov at Robarts for his assistance on 3D metal sintering; and Dr. Sabarinathan, who taught the Photonics course, for her advice on fiber optic principles.

Special acknowledgement goes out to a few individuals who went out of their way to provide me with every available resource including their time and specialized knowledge. Daniele Tosi, PhD, at the University of Limerick, was the author of one of the first papers I reviewed on fiber optic interrogation. After initiating correspondence with him, he enthusiastically shared many important details on his work with FBGs. His constant help allowed me to pursue this high-tech area of force sensing that I previously had no knowledge of. Eugen Porter at the Electronics Shop in the Thompson Engineering Building is the current staff head of the Western Engineering Robotics (WEBots) club on campus that runs for 5 hours every Wednesday. By joining this club at the very start of my thesis project, Eugen assisted me in every area of Electrical Engineering that I required. Starting with the proper use of a resistor, and ending with the complete design of the circuit board shown below, Eugen guided me at every turn. I would like to thank Chris Vandelaar at the University Machine Shop in TEB for his willingness to humor the impossible in machining and fabrication. The precise measurements, complex techniques, and minute cuts required to make this medical tool were almost unthinkable, but his help, constant support, and trust in my determination allowed everything to come together remarkably well. Finally, to my brother Aaron Yurkewich, whose CSTAR summer NSERC volunteering brought me into contact with Dr. Patel and Dr. Naish, and helped me become a part of the CSTAR team. Now on his own M.E.Sc. degree at CSTAR, he helps me day in and day out by letting me bounce ideas off of him, by giving me motivation to strive to achieve higher goals, by supporting me when I hit mental roadblocks, and by being there to share in each success no matter how small. I could not have done this without him.

Table of Contents

Abstract ii

Acknowledgements iii

Table of Contents v

List of Figures ix

List of Tables xii

Nomenclature and Acronyms xiii

1 Introduction

1.1 Motivation	1
1.2 Current Techniques	1
1.3 Project Goals	2
1.4 Research Objectives	2
1.5 Scope	3
1.6 Overview of the Thesis	3

2 Literature Review

2.1 Introduction	5
2.2 Force Sensing Medical Devices	5
2.3 Optical Fiber Technology	12
2.3.1 Optical Fiber Overview	12
2.3.2 Grating Analysis	13
2.3.3 Theoretical FBG Calculations	14
2.3.4 Spectrum Analysis Techniques	15
2.3.5 Benefits and Challenges	17
2.4 Interrogation Systems	18
2.4.1 Fiber Optic Components and Losses	18

2.4.2 Systems	20
2.5 Summary	28
3 Fiber Optic, Electrical, Mechanical and Software Design	
3.1 Introduction	29
3.2 Design Specifications	29
3.3 Low-Cost Interrogation Design	30
3.4 Electrical Circuit Board Design	35
3.5 Grasper Design	37
3.6 Shaver and Probe Design	47
3.6.1 Shaver Design	47
3.6.2 Probe Design	49
3.6.3 Preliminary Manufacturing.	50
3.7 Software Design	53
3.7.1 Final Design	53
3.7.2 Software Version Development	55
3.8 Summary.	57
4 First-Generation Prototype Evaluation	
4.1 Introduction	58
4.2 Calibration	58
4.2.1 Sensor Shaft Calibration (Axial)	58
4.2.2 Sensor Shaft Calibration (Bending)	59
4.2.3 Grasping Calibration	60
4.3 Performance Assessment	62
4.4 Validation of Force Calibration	63
4.4.1 Sensor Shaft	63
4.4.2 Grasping	65

4.4.3 Overall System Performance	65
4.4.4 Auto Zero-Drift Compensation Method	66
4.5 Summary	66
5 Evaluation and Discussion – Second Generation Instrument	
5.1 Introduction	67
5.2 Design Changes	68
5.3 Calibration Changes	70
5.3.1 Bending Calibration	70
5.3.2 Grasper Calibration.	74
5.3.3 Axial Calibration	75
5.3.4 Signal Coupling	77
5.3.5 Noise and Drift	79
5.4 Performance Assessment	82
5.5 Validation of Force Calibration	83
5.5.1 Bending Forces.	83
5.5.2 Grasping Forces	85
5.5.3 Axial Forces.	85
5.5.4 Coupling Offsets.	86
5.6 Summary	87
6 Conclusions and Future Work	
6.1 Introduction	88
6.2 Contributions	88
6.3 Recommendations and Future Work	89
References	94
Appendices	

I Software Interface	98
II EM Tracker Design Concept.	104
III SLD Power and Voltage Curves	105
IV Material Decision Table.	106
V Calculation Example using Coupling Biasing	107
VI Permissions and Approvals	111

Curriculum Vitae	125
-------------------------	------------

List of Figures

2.1	Forces acting on minimally invasive instruments	6
2.2	Motor driven current-based laparoscopic grasper prototype	7
2.3	Piezoelectric tactile sensor	7
2.4	Vibrational tactile piezoelectric sensor measurement system	8
2.5	5mm diameter tri-axial tool	9
2.6	Fabry-Perot retinal probe	10
2.7	2-DOF force sensing micro-forceps	10
2.8	Fiber attachment method	11
2.9	FBG retinal probe	11
2.10	FBG structure, with refractive index profile and spectral response	14
2.11	FBG spectral wavelength shift showing reflective light intensity	17
2.12	Cost-effective strain interrogation system	21
2.13	Wavelength division coupler interrogation system	21
2.14	Arrayed waveguide interrogation unit	22
2.15	Matched filter interrogation unit	23
2.16	Temperature independent interrogation system	24
2.17	Long period grating interrogation system	25
2.18	Hybrid long period/fiber Bragg grating system	26
2.19	Bi-conical filter interrogation system	27
3.1	Fiber optic instrumentation schematic	31
3.2	SLD and laser spectrums	32
3.3	FBG response curve with applied weight	35
3.4	Circuit board design	37
3.5	Full arthroscopic grasper with 4 extruding fibers	38
3.6	Triangle jig assembly for sensor slot micro-machining	39
3.7	Sensor Shaft	40
3.8	Axial amplification element	42
3.9	Grasper jaws	43

3.10	SolidWorks jaw model	44
3.11	SolidWorks handle model	45
3.12	Actuating rod	45
3.13	Reference fiber vice	46
3.14	Grasper assembly view	47
3.15	CAD shaver assembly view	48
3.16	CAD Probe assembly view	49
3.17	Shaver assembly	50
3.18	Probe assembly	51
3.19	Shaver mounted in motor	52
3.20	Probe clamp	52
3.21	Software interface showing 3 signals	55
4.1	Axial calibration apparatus	59
4.2	Bending calibration apparatus	60
4.3	FBG calibration curves	60
4.4	Grasper calibration apparatus	61
4.5	Grasper force calibration	61
4.6	Force and angle prediction at 60 degree applied load	63
4.7	Accuracy errors vs. angle of applied force	64
5.1	Second generation instrument with stress relief cable	67
5.2	1” thinned sensor guide cut apparatus	68
5.3	FBG pre-straining apparatus	69
5.4	Fusion splicing apparatus	70
5.5	Micron Optics bending calibration curves (Sensors 1 – 3)	72
5.6	Low-Cost System bending calibration curves (Sensors 1 – 3)	73
5.7	Grasper calibration curve	74
5.8	Axial strain calibration apparatus	75
5.9	Low-Cost System axial tuning	76
5.10	Axial calibration curve	77
5.11	Micron Optics coupling curves	78

5.12	Low-Cost System coupling curves	79
5.13	Micron Optics noise and drift data	80
5.14	Low-Cost System noise and drift data	81
6.1	5N grasping force over 1 second intervals	93
A.1	Raw data voltage plot showing synced vs. unsynced signals	98
A.2	Bending, axial, and grasping force calibration	99
A.3	Bending and axial calibration curves	100
A.4	Grasping force calibration curve	101
A.5	Visual bar graph force output with recording option	102
A.6	Additional options for port control and zero estimation	103
A.7	EM tracker design	104
A.8	Benchtop SLD power and voltage curves	105
A.9	Tool testing condition on knee simulator.	107
A.10	Predictive bending force technique	110

List of Tables

Table 2.1	Costs for Primary System Instrumentation Components	20
Table 3.1	MicroGroup Hypodermic Tubing Listing and Specifications	41
Table 4.1	FBG Sensor Calibration Assessment	63
Table 5.1	Micron Optics Calibration Assessment	83
Table 5.2	Low-Cost System Calibration Assessment	83
Table A.1	Bending and Shear Stress Material Analysis	106

Nomenclature and Acronyms

Acronyms

ADC	Analog to Digital Converter
BW	Bandwidth
BFF	Bi-conical Fiber Filter
CAD	Computer-Aided Design
CFBG	Chirped Fiber Bragg Grating
CSTAR	Canadian Surgical Technologies and Advanced Robotics
DAQ	Data Acquisition
DOF	Degree of Freedom
EDM	Electrical Discharge Machine
EM	Electro Magnetic
FBG	Fiber Bragg Grating
FC-APC	Ferrule Connector – Angled Physical Contact (angled face)
FC-UPC	Ferrule Connector – Ultra Physical Contact (flat face)
FP	Fabry-Perot
FPI-FS	Fabry-Perot Interferometric Force Sensor
F/T	Force/Torque
FTDI	Future Technology Devices International
GUI	Graphical User Interface
I ² C	Inter-Integrated Circuit
ID	Inner Diameter
I/O	Input/Output
LCD	Liquid Crystal Display
LED	Light-Emitting Diode
LPG	Long Period Grating
MIS	Minimally Invasive Surgery
MMC	Micromachining Centre
MRI	Magnetic Resonance Imaging
NA	Neutral Axis
OD	Outer Diameter
OEM	Original Equipment Manufacturer

OR	Operating Room
OSA	Optical Spectrum Analyzer
PC	Personal Computer
PCB	Printed Circuit Board
PD	Photodiode
PVDF	Polyvinylidene Fluoride
SC	Standard Connector (Fiber Optic)
SLD	Super-Luminescent Diode
SP	Signal Processing
SPI	Serial Peripheral Interface
RLS	Recursive Least Squares
RMS	Root Mean Squared
SIMIS	Sensorized Instrument-based Minimally Invasive Surgery
UART	Universal Asynchronous Receiver/Transmitter
USB	Universal Serial Bus
WDC	Wavelength Division Coupler

Variables

Λ	Grating period spacing
λ_B	Bragg wavelength
n	Refractive index
P_{11}, P_{12}	Pockel's coefficients of the stress optic tensor
ε	Applied strain
ν	Poisson's ratio
α	Coefficient of thermal expansion
σ	Standard deviation
T	Temperature
x, y, z	Cartesian coordinates corresponding to bending (x, y) and axial (z) stresses
F_{distrib}	Distributed force
D_{moment}	Length of moment arm/tool shaft
E	Young's Modulus
D_o	Outer diameter
D_i	Inner diameter

Y_s	Yield strength
Q	First moment of area

Units

cm	centimeters
mm	millimeters
μm	micrometers
pm	picometers
nm	nanometers
Nm	newton-meters
g	grams
GB	gigabytes
Hz	hertz
mN	millinewtons
N	newtons
s	seconds
ms	milliseconds
pC	pico-coulombs
$^{\circ}\text{C}$	degrees celsius
M Ω	megaohms
mA	milliamps
dB	decibels
n ϵ	nanostrain
$\mu\epsilon$	microstrain
mW	milliWatts
V	volts
VAC	volts alternating current

Chapter 1

Introduction

1.1 Motivation

Minimally-invasive surgery (MIS) has become a widely accepted alternative to open surgery in a broad number of surgical specialties. Certain orthopedic procedures, such as meniscectomies and ligament reconstructions [1,2], are now mostly performed arthroscopically. There are many benefits of using small access points as opposed to the large incisions used in open surgeries. These include, but are not limited to, better cosmesis [3,4], reduced blood loss [5,6], less pain [5], reduced infection rates [7,8], faster recovery and shorter hospital stay [6,9]. The major hindrances in MIS, however, are reduced haptic (tactile/force) feedback [10,11] and a steep learning curve [12]. If excessive force is applied due to the lack of force feedback, there can be increased damage and trauma to healthy tissue. Conversely, if insufficient grasping force is applied to tissue, this can lead to slippage, loss of control, and loose intracorporeal knots. While expert surgeons have risen to these challenges through deliberate practice, the novice surgeon or trainee has limited opportunities to practice their skills before operating on their first patient. In the last decade, multiple simulators have been developed to address this problem, but the simulated haptic feedback is not always representative of the real surgical situations. Therefore, the development of force-sensing arthroscopic instruments may assist in training novice orthopedic surgeons, as well as allow for surgical force data to be collected for both novices and experts. This data may prove useful for the objective assessment of surgical skills.

1.2 Current Techniques

In traditional arthroscopic surgery the force exerted on the soft tissue is estimated by the surgeon both visually through the endoscopic camera, based on perceived tissue deformation, and by feeling the resistive force exerted across the instrument shaft to the tool handle. Over a period of time, a firm understanding of the proper forces for each surgery can be firmly grasped. In surgical training, however, the experienced surgeon must attempt to convey his or her perception

of these small forces verbally, without any direct, immediate force feedback. This increases the training time and decreases the overall effectiveness.

1.3 Project Goals

The goal of this work is to design a robust, sterilizable, cleanable arthroscopic grasper that can measure the forces acting on it during use. While a selected few instruments feature either small size, high sensitivity/resolution, or applications in arthroscopy, no existing tool demonstrates all of these features in a contained, surgery-ready, aesthetic grasper design using a fiber Bragg grating approach. With insertion into a minimally invasive incision or trocar, the translation of the tool is restricted to axial motion while the rotational movement of the tool around the entry point has freedom about all 3 axes. It also contains an additional degree of freedom for actuation of the grasping jaws. Due to the small size of tissue being grasped, small jaws, and small shaft, torsion caused by off-center x , y and z forces are initially hypothesized to be negligible. The current grasper design is able to measure x and y bending forces (tissue side forces), z axial forces (tissue prodding/pulling), and grasping force. Torsion forces, corresponding to twisting the tissue, were not included in this design to decrease the complexity in these early generations of the tool.

1.4 Research Objectives

The main goal of this research is to develop force sensing arthroscopic tools that are similar in appearance to current surgical tools. To achieve this objective, the development has focused on the following objectives:

- To design and build a low-cost fiber optic sensing system capable of reading reflected light signals from Bragg grating fibers for lab use.
- To design, manufacture, and test a series of arthroscopic instruments containing fiber optic sensors to measure the tissue-forces on the instrument.
- To develop a photo-electrical system that converts light signal from the fibers into a high-resolution low-noise digital electrical signal.
- To develop software to assist in calibration and force calculation from the given electrical signals.

1.5 Scope

Research-based projects at Canadian Surgical Technologies and Advanced Robotics (CSTAR) are currently exploring the necessity of kinesthetic information in surgical and therapeutic applications. They have identified that force information recorded during MIS procedures can be used both to effectively develop metrics in surgical simulators, and to assist in skills assessment. This thesis therefore assumes the importance of force feedback, and specifically focuses on the mechanical development of the arthroscopic tools and the formation of a corresponding force sensing system. The potential of the complete system will be evaluated based on the precision, accuracy, and usability of the tool. Previous arthroscopic instruments have been developed to sense forces in just 1 direction of force using externally attached strain gauges; therefore, the tools presented in this thesis will be designed to measure 4 DOF (grasper) and 3 DOF (shaver and probe) using internal fiber optic sensors.

1.6 Overview of the Thesis

The structure of this thesis is as follows:

- Chapter 2** Literature Review: Summarizes the state of the art in fiber optic minimally invasive instruments and FBG interrogation systems, and provides background information on fiber optic principles and Bragg gratings.
- Chapter 3** System Design: Presents the detailed work done on the fiber optic, electrical, mechanical and software subsystems of the design.
- Chapter 4** Evaluation and Discussion: Describes the calibration process of the system, and discusses the results obtained and their significance.
- Chapter 5** Evaluation and Discussion – Second Generation Instrument: Describes design, calibration and assessment changes of the system between February 2014 and December 2014, and discusses the results obtained and their significance.
- Chapter 6** Conclusions and Future Work: Highlights the contributions of the thesis and suggests future areas of research.
- Appendix I** Software Interface: Presents the user interface used to read and formulate the FBG signals. Calibration curves, buttons, and final forces are presented,
- Appendix II** EM Tracker Design Concept: The design concept and placement of an EM tracker on the arthroscopic grasper is shown.

- Appendix III** SLD Power and Voltage Curves: ThorLabs SLD bench-top source specifications
- Appendix IV** Initial Bending/Shear Stress, Strain, Force, and Material Decision Table: This table calculates the forces on the tool based on a variety of dimensional and material selections.
- Appendix V** Calculation Example using Coupling Biasing: This thorough calculation example shows the complete process of reading a set of voltages, and using the bending, grasping, axial, and coupling calibration curves to equate resultant forces.
- Appendix VI** Permissions and Approvals: Presents approval letters for copyrighted figures and material.

Chapter 2

Literature Review

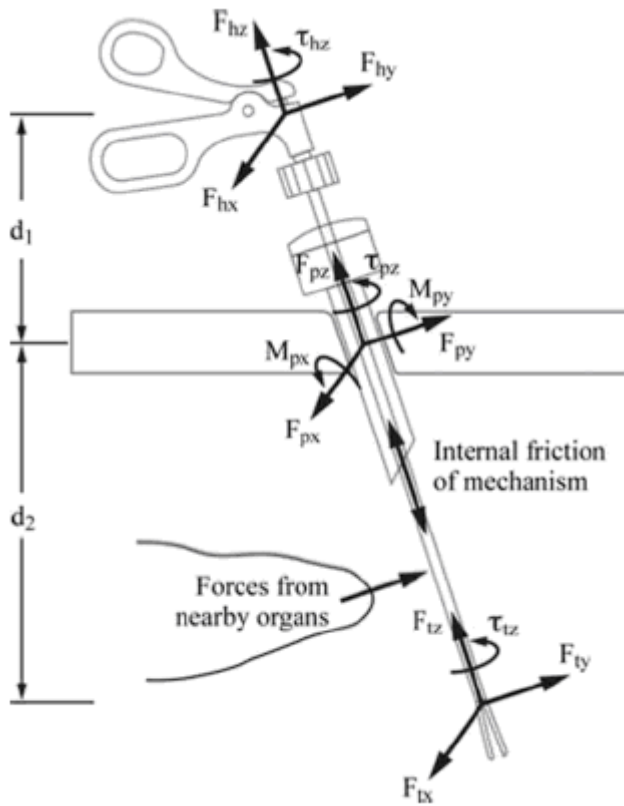
2.1 Introduction

In the initial discovery phase of the research, various medical tools and their specifications, medical sensors, and arthroscopic procedures were investigated. Focus was then placed on fiber optic force sensors, and additional research was begun on the development of low-cost interrogation systems, fiber optic components, optical power and corresponding losses, light sources (laser and SLD), and fiber optic Bragg gratings. Following this initial research time period, regular literature review was conducted to discover emerging medical tools, new fiber optic concepts, and technical procedures for connecting, cleaning, attaching, and interrogating the fibers. The subsequent review starts off with a state-of-the-art summary of force sensing minimally invasive tools. Fiber optics have been incorporated into a vast variety of medical sensors, and while these will be touched upon, more emphasis will be put on applications involving minimally invasive tools and FBG-specific sensors. Next, an introduction to the technology and fundamentals of fiber optics is discussed, with emphasis on various types of FBG gratings, and some of their applications. Finally, a separate review on current low-cost fiber Bragg grating interrogation systems is included. The development of new low-cost approaches to read the FBG light signals is currently one of the most complex and heavily researched areas in FBG sensors.

2.2 Force Sensing Medical Devices

Force sensing feedback can indicate if the surgeon is applying the right amount of force to an area within the surgical site. In orthopedic surgery, since contact can occur between either soft tissue or bone, tactile force feedback can augment the image from the arthroscope to help characterize the stiffness of the tissue in contact with the instrument, and to gauge the appropriate forces to apply. In related papers by Trejos *et al.* [13,14], a laparoscopic instrument was developed to measure all degrees of freedom acting on the instrument during surgery. As

illustrated in this paper, Figure 2.1 shows the percentage of total forces applied to each section of the tool during surgery.



Forces at the handle are 2 to 6 times greater than tip forces [15].

Friction at the trocar: 0.25 – 3 N [16,17].

Torques created by the abdominal wall: up to 0.7 Nm [17].

Internal instrument friction losses: 58% to 92% [18].

Forces and torques at the tip: 0.5 to 10 N, 0 to 0.1 N [17].

Figure 2.1: Forces acting on minimally invasive instruments [14].

In the field of MIS, there has already been significant research in sensor development. “State-of-the-art in force and tactile sensing for minimally invasive surgery” by Puangmali *et al.* [19] organizes a broad range of these design ideas. Of special note is a servo-driven springless encoder developed by Rosen *et al.* [20] that actuates the jaws of a tele-operated grasper. The failings of displacement sensors usually lie in frictional losses and in backlash of drive mechanisms; therefore by replacing the elastic element, these errors can be eliminated. Another device to point out in this MIS review was developed by Tholey *et al.* [21]. The current measuring approach shown in Figure 2.2 incorporates a motor driven cable on a custom made laparoscopic grasper. The total accuracy of the system was however diminished by errors due to friction, inertial resistance, mechanical backlash,

change in armature quality, and current variances between other joints, and by the limited calibration techniques available for relating the change in current to force.

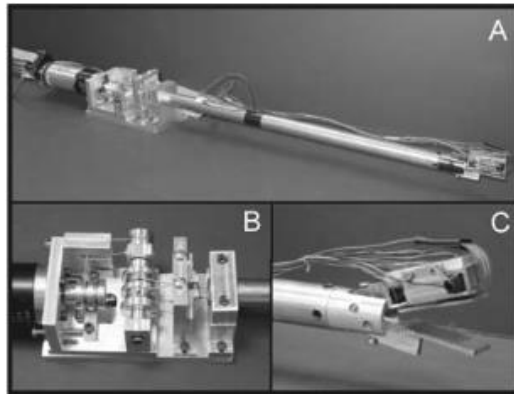


Figure 2.2: Motor driven current-based laparoscopic grasper prototype [21].

Piezoelectrics have also become a very popular technique for force sensing devices. Sakanvar *et al.* [22] developed the tactile sensor in Figure 2.3 for an arthroscopic minimally invasive tool to sense grasping forces. The PVDF (Polyvinylidene fluoride) film used in this design has a 10 times larger piezoelectricity than many other polymers, with 6-7 pC/N. Another benefit of this design is that the piezoelectric sensors also act as teeth for the grasper. In this way there is no medium between the forces and the film, just direct transference. A novel aspect of this design is that by measuring the resultant deflection as well as the amplitude of the applied load, it can sense the softness of the object as well. For example, a rigid object would essentially not bend the sensor at all, but just stretch across the teeth. By changing the Young's Modulus, thickness, and length of the flexible substrate, the force sensor can be designed for a specific range of loads.

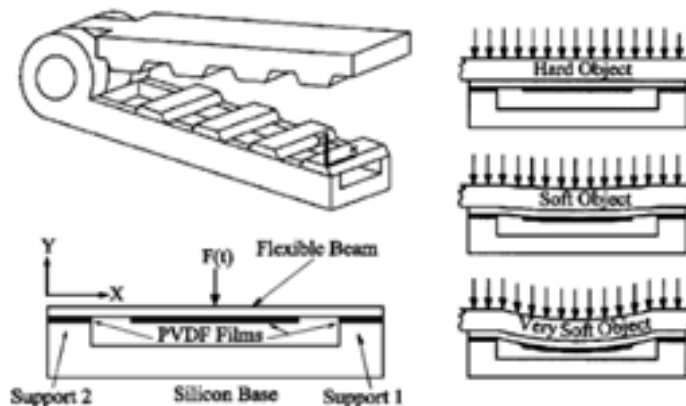


Figure 2.3: Piezoelectric tactile sensor [22].

Ohtsuka *et al.* [23] developed a vibrational-based sensor that is constructed of a sensor probe, amplifier, filter, and frequency counter (Figure 2.4). The sensor probe is acoustically connected to a piezoelectric transducer composed of lead zirconate-barium titanate ceramics. The transducer has a 92 Hz base resonant frequency that changes based on the softness of the tissue it comes into contact with. A sudden upward spike in the computer feedback system would mean that a hard spot was found in the lungs. The main need that this system addresses is to locate deeper lung nodules. While a surgeon can usually distinguish these nodes with his or her fingers, this is an invasive procedure.

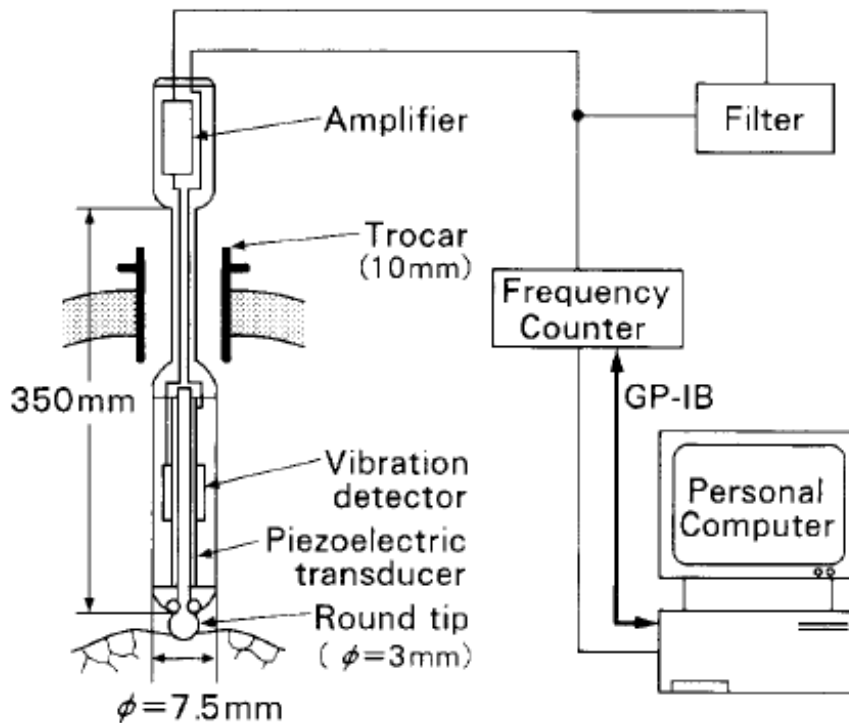


Figure 2.4: Vibrational tactile piezoelectric sensor measurement system [23].

Piers *et al.* [24] designed a 5 mm diameter tri-axial tool that by sending light down the length with 3 optical fibers would reflect off of a flat mirror on a flexible element (Figure 2.5). The spacing between the fibers and mirror was set to be $100\ \mu\text{m}$. A 2 mm diameter hole along the center allows for various tools to be passed through. Experimental results yielded a force range of 2.5 N with a resolution of 0.01 N. The figure also shows the path of the fiber returning to the receiver. Instead of using separate fibers to send and receive the signal, a circulator/optocoupler was used so that the emitting and receiving signal could be sent down the same fiber, and properly channeled to their separate destinations. The benefit of this is that it halves the separate paths needing to be designed in

the tool. With size as a limiting factor in MIS tools, minimizing instrument size is essential. Additionally, a Fabry-Perot interferometric force sensor (FPI-FS) device was created by Liu *et al.* [25] to outfit a probe for vitreo-retinal microsurgery (Figure 2.6). He et al. [26, 27] developed a miniaturized vitreo-retinal grasper capable of sensing forces imperceptible to human touch (Figures 2.7 and 2.8). It uses three Bragg grating fibers attached to a stiff titanium wire to take measurements. This allowed sensing in two degrees of bending with axial force being out of range. Figure 2.9 shows the earlier conceptual design of a similar sub-millimetric vitreo-retinal tool [28, 29].

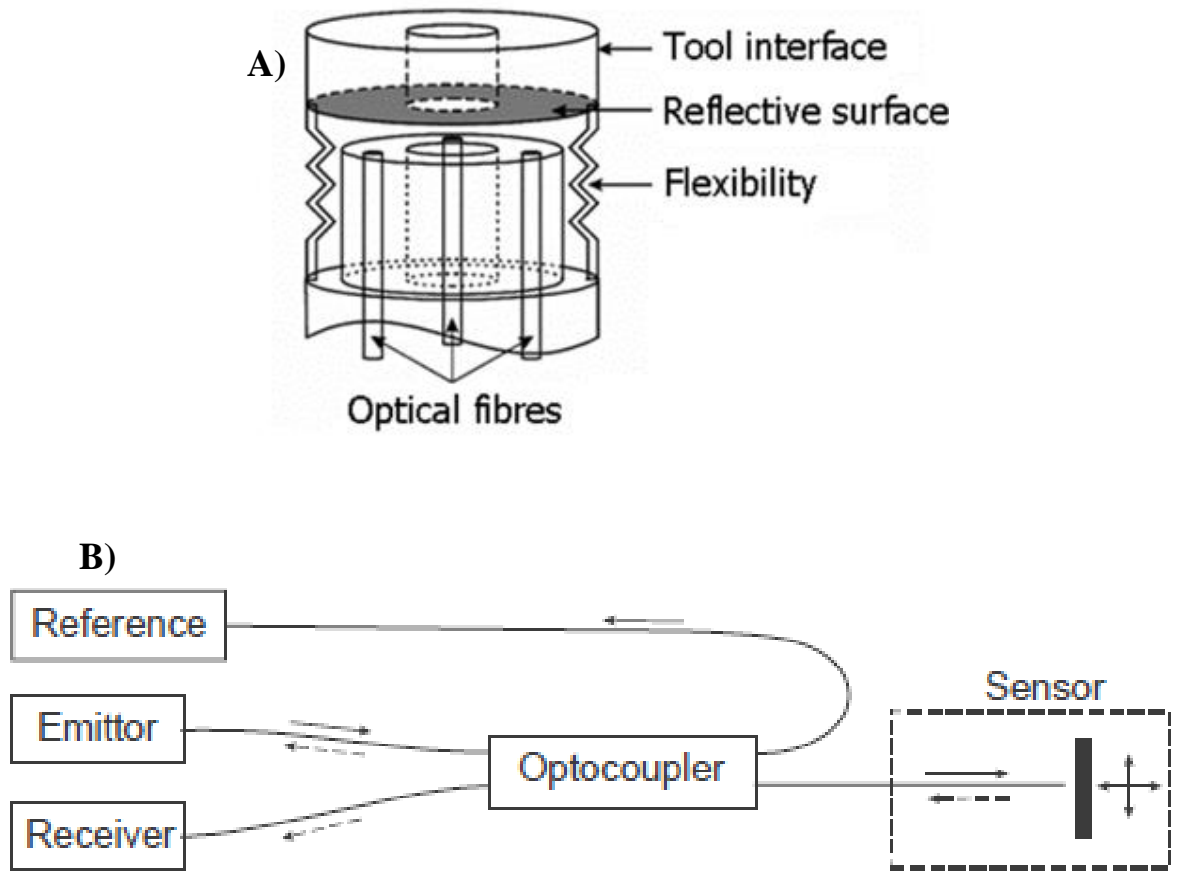


Figure 2.5: 5mm diameter tri-axial tool (a) three optical fibers measure deformation of the flexible structure; (b) reflective position measurement configuration [24].

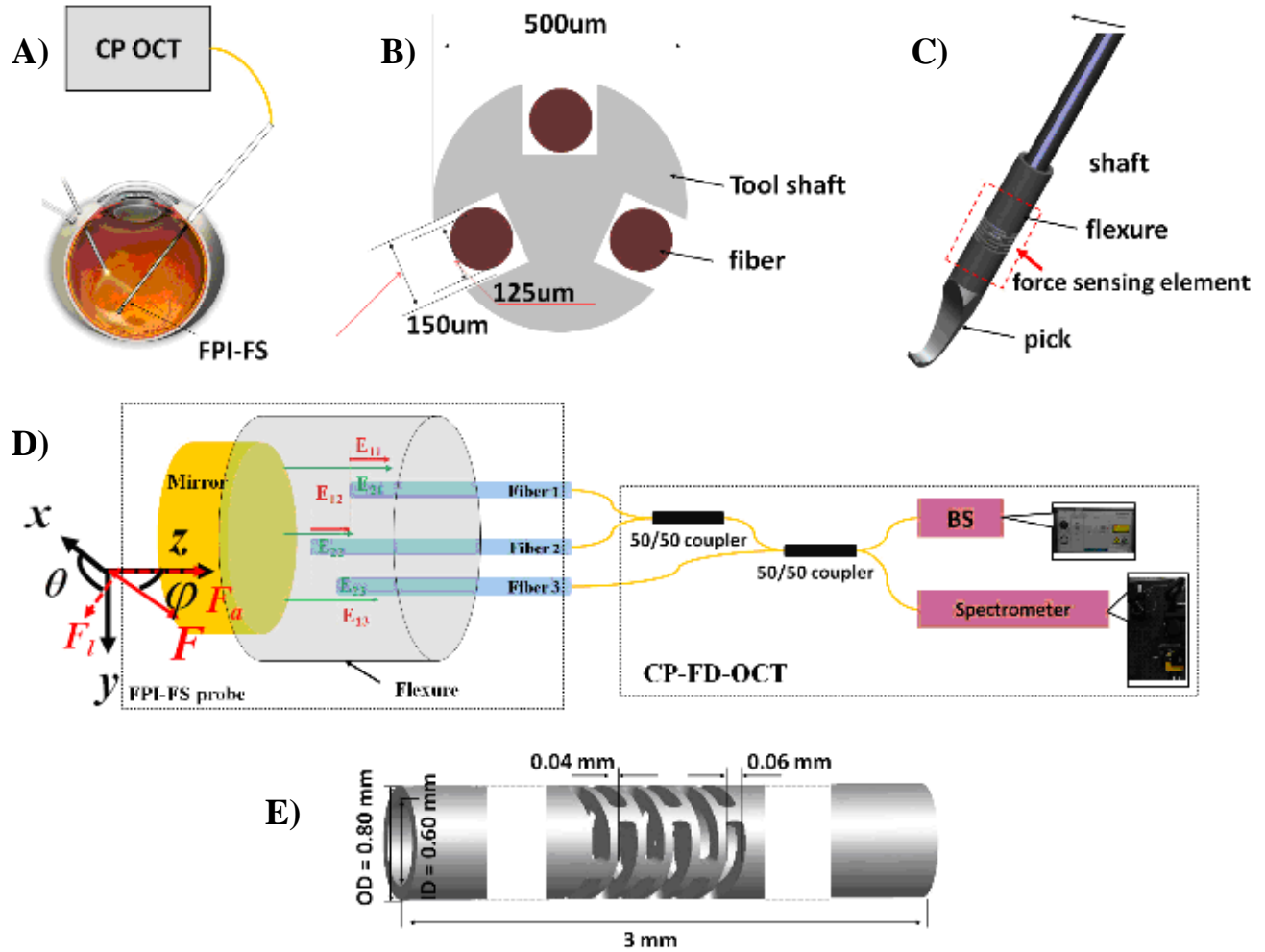


Figure 2.6: Fabry-Perot retinal probe (a) system schematic of FPI-FS; (b) cross section of tool shaft with embedded fiber; (c) CAD model of FPI-FS probe on probe handle (d) detailed schematic of the system with FPI-FS and CP-OCT interrogation; (e) CAD model for the Nitinol flexure [25].



Figure 2.7: 2-DOF force sensing micro-forceps [27].

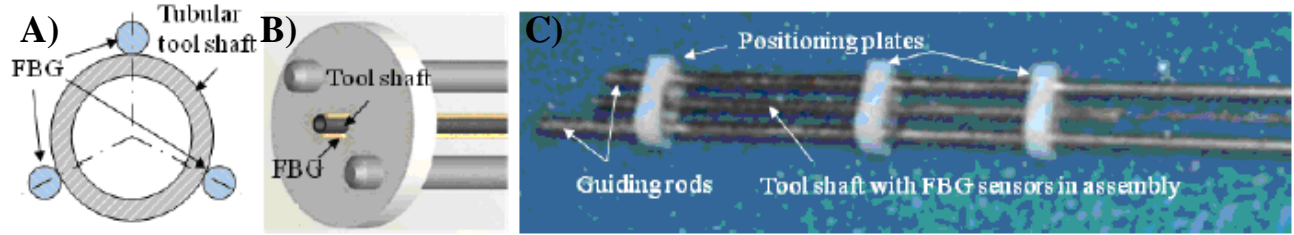


Figure 2.8: Fiber attachment method (a) section view of the tubular tool shaft with the FBG sensors; (b) close-up of the guiding jig for FBG alignment; and (c) the guiding jig in assembly [27].

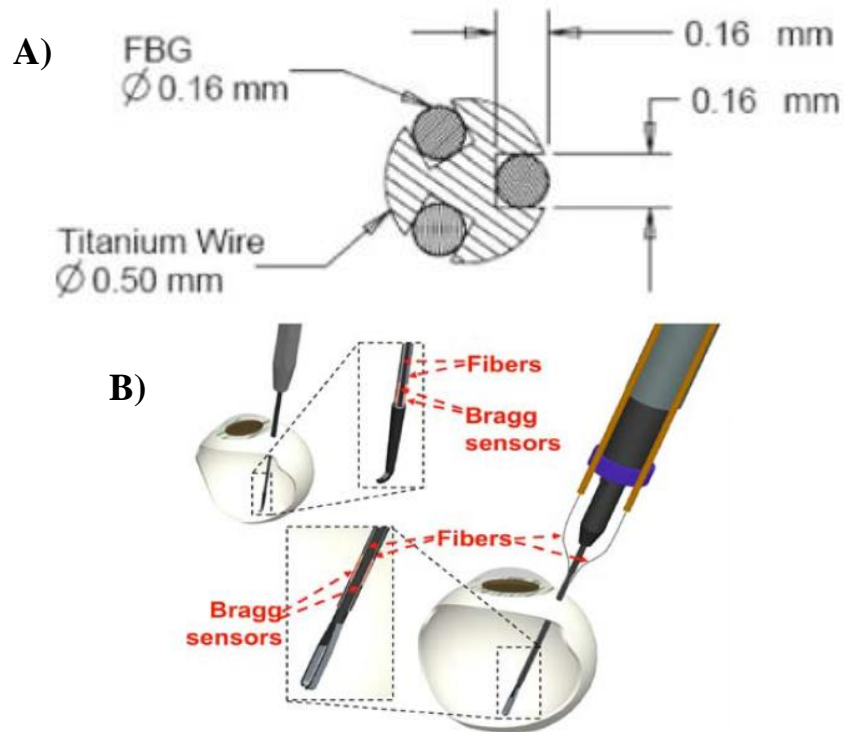


Figure 2.9: FBG retinal probe (a) cross-section diagram of 2-DOF force-sensing tool; (b) conceptual design of optical fiber force-sensing tool [28].

US Patent 20070151390 A1 [30] (Force and torque sensing for surgical instruments) by Blumenkranz and Larkin introduces the theory of threading sensors along a surgical tool shaft for force and torque measurement. US Patent 8561473 B2 [31] (Force sensor temperature compensation) again under inventor Blumenkranz but published later, broadly describes the possibility of using either wire leads or fiber-optic-based strain gauges along a surgical instrument to measure force; it additionally describes a temperature-compensation method. To compensate for temperature, a negative thermo-optic coefficient optical fiber material could be used, a reference unstrained fiber could be added, or various thermo-optic coefficient materials could be used and

compared. The recommended application is for teleoperated medical tools operated at a remote location from the patient. US Patent 20110224689 A1 [32] (Robotic surgery system including position sensors using fiber Bragg gratings) by Larkin and Shafer adds on to the previous patents by describing the use of the strain characteristics of the FBG sensors to calculate the position of the tool end-effector. US Patent 20090123111 A1 [33] (Optical fiber grating sensors and methods of manufacture) by Udd evolves the development of FBG strain sensors on medical tools by recommending alternative grating manufacturing and application techniques to increase resolution.

For a comprehensive reading on various other uses of fiber Bragg gratings in medicine, the paper by Mishra *et al.* [34] “Fiber grating sensors in medicine: Current and emerging applications” describes many different applications:

- Thermal mapping of cardio-vasculature
- Pressure mapping of orthopedic joints
- Low temperature monitoring
- Immunosensing
- Monitoring foot pressure and gait analysis for diabetics
- Temperature and pressure sensing in a dental splint
- Monitoring of handgrip strength for physical disorders
- Heartbeat and respiratory monitoring
- Urinary incontinence & pelvic floor disorders
- Measuring of ultrasonic waves
- Tactile, temperature, and strain sensing
- Lab-on-chip technologies
- Robotic surgery

2.3 Optical Fiber Technology

2.3.1 Optical Fiber Overview

The fibers used for fiber optic sensing are first categorized into either multi-mode or single-mode depending on their core size, and how many propagation modes can be handled. Single-mode fibers are typically used for scientific sensors since they only allow one mode, and as such are not limited by modal dispersion. This allows the light to be focused more precisely. Multi-mode fibers however

require a lower-cost light source and have a lower percentage loss when connecting the fibers. In the context of FBGs, single-mode fibers are primarily used since they return a single distinct peak wavelength. As discussed by Lu and Cui [35], it is possible to create an FBG out of a multi-mode fiber with a greater degree of numerical calculation. Their research may further help to decrease the overall cost of the current FBG interrogation system.

The two main methods for using fiber optic sensors as strain sensors are either to internally manipulate the wavelength spectrum of the light in the fiber (FBG); or to send light out of the fiber and to reflect the light off of a surface (Fabry-Perot). There are four further main methods to read the returning light signals. The first is to use a reference fiber and compare light intensities. The second is to use an optical spectrum analyzer to read the actual spectrum of light returned. The third is to split the returning light signal and recombine it out of phase to determine wavelength properties (interferometry). Fourth, a swept-laser source can be used to pinpoint the current wavelength of the system.

2.3.2 Grating Analysis

The grating on a FBG fiber is similar to a series of internal mirrors running along a small 1–3 cm section of the fiber. These “mirrors” are in fact periodic variations in the refractive index of the fiber core, which cause a specific wavelength of light to be reflected internally. These gratings are added either with a single high-powered laser in conjunction with a precise phase mask, or with two interfering lasers that produce a grating according to their interference pattern. The grating on a fiber is characterized by its grating period, and how this period changes along the fiber. The most basic grating type is the uniform fiber Bragg grating (FBG), where the period is uniform along the length of the affected length of fiber, and is approximately 500 μm . Another common grating type is termed a long-period grating (LPG), due to its much longer period length of 0.1 to 1 mm rather than 500 nm. This greatly simplifies the grating inscription process. Instead of measuring the reflection of light restricted to within the core, forward propagating modes are employed, and transmission through the cladding is instead measured. The response spectrum is also much broader than with FBGs, giving it unique applications in band-rejection, and gain-flattening, filters. As will be described in Chapter 5, the broad spectrum provides a larger unique linear range at the cost of a weaker signal. A third type of grating is a chirped fiber Bragg grating (CFBG), which has a linear increase or decrease in the grating period. Instead of reflecting a single wavelength, this allows a

broader range of wavelengths to be reflected, resulting in greater dispersion. This also means that each chirped wavelength will return at a different measurable time delay. With more costly interrogation equipment, this would increase the precision of each fiber and the corresponding output signal. A fourth type, apodized gratings, reduce the period to zero on either side of the grating, aiding in side-lobe suppression. These four types of gratings are currently the main focus of current FBG sensing technology; however, other types exist such as discrete phase shift gratings, and superstructure gratings.

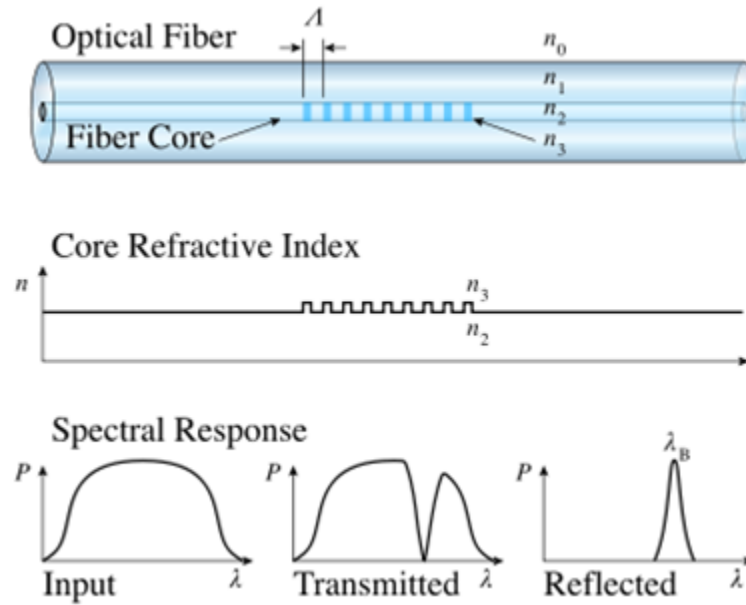


Figure 2.10: FBG structure, with refractive index profile and spectral response [36].

2.3.3 Theoretical FBG Calculations

The equations below show the dependency on various optical, thermal, and strain properties for calculating the Bragg wavelength [37,38]. On an FBG that is unstressed by external forces (strain, pressure, temperature, displacement, acceleration), the period spacing, denoted by Λ , can be related to the Bragg wavelength λ_B , through the refractive index, n (n_2 in Figure 2.10) of the fiber core material according to

$$\lambda_B = 2n\Lambda \quad (1)$$

Therefore, in using a Bragg wavelength of 1544 nm, with the refractive index of fused silica being approximately 1.444 [39], the grating period is approximately 534.6 nm. Equation 2 [38] represents

the extended Bragg wavelength formulation under axial strain and thermal stress where P_{11} and P_{12} are Pockel's coefficients of the stress optic tensor, ε is the applied strain, ν is Poisson's ratio, dn/dT represents the thermo-optic coefficient, and α is the coefficient of thermal expansion of the fiber material.

$$\lambda_B = 2n\Lambda \left\{ \left(1 - \frac{n^2}{2} (P_{12} - \nu(P_{11} + P_{12})) \right) \varepsilon + \left[\alpha + \frac{dn}{dT} \right] \Delta T \right\} \quad (2)$$

The Pockel's coefficients quantify the polarization on the application of a stress, and can be equated as polarization/stress. A numerical value of 0.22 can be assumed for this term [37,38], dependent on the properties of the fused silica fiber. Simplifying Equation 2 gives Equation 3 [37,38]:

$$\lambda_B = 2n\Lambda \left\{ (1 - .22) \varepsilon + \left[\alpha + \frac{dn}{dT} \right] \Delta T \right\} \quad (3)$$

Further research has gone into determining the properties of the fiber sensor at constant strain or constant temperature. This method is useful when the material is to be used at thermal or strain equilibrium. The measured strain response in thermal equilibrium and strain equilibrium are shown by Equations 4 and 5 respectively [38].

$$\frac{1}{\lambda_B} \frac{\delta\lambda_B}{\delta T} = 6.67 \times 10^{-6} \text{ } ^\circ\text{C}^{-1} \quad (4)$$

$$\frac{1}{\lambda_B} \frac{\delta\lambda_B}{\delta \varepsilon} = 0.78 \times 10^{-6} \text{ } \mu\text{E}^{-1} \quad (5)$$

Interpreting these responsivities, a resolution of 0.001 nm (1 pm) is required to measure either a temperature change of 0.1 °C or a strain change of 1 μ strain. This precision is typically only possible with systems consisting of Optical Spectrum Analyzer (OSA) or FBG Interrogator technologies.

2.3.4 Spectrum Analysis Techniques

The silica glass core of a FBG is typically 6–8 μ m, the cladding is typically 125 μ m and has a lower refractive index than the core, the coating is 250 μ m, and the jacket varies between 400 and 900 μ m. When light is directed down the length of the fiber, it interacts with the gratings, and the full wavelength spectrum of the light is split between transmitted light and reflected light according to the grating and incident light wavelengths. Depending on whether the incident light is a narrow

wavelength specific laser, or a broadband super-luminescent diode (SLD) source, the fraction of reflected light will vary. The laser option is typically used in a swept manner with an OSA. Single probes of light are sent one at a time over a certain wavelength range until the reflected light becomes a maximum. The wavelength that corresponds to the maximal reflection is read by the OSA, and can then be related to the Bragg period of the fiber. The SLD source technique sends a parabolic power spectrum into the fiber. When the light refracts on the grating, it will remove a slice of the SLD spectrum corresponding to the Bragg period of the fiber. Since the SLD spectrum is parabolic in nature, the returning power will be directly relatable to the Bragg period. The method used in this thesis incorporates the SLD approach, but uses a first FBG to initially narrow the broad spectrum of the SLD, and then uses another FBG to further dissect the spectrum.

Figure 2.11 shows the spectrums of 1546.1 nm and 1544.9 nm centered FBGs. As strain is applied to the 1544.9 nm FBG, its spectrum is pushed to the right and overlaps that of the 1546.1 nm FBG. The area under the overlapping spectrum (in light blue) represents the reflected optical power. After the 1544.9 nm FBG is overstrained, its spectrum passes to the right of the 1546.1 nm FBG and the power will again drop off back to zero. By restricting the strain to either the increasing or decreasing side of the reference fiber spectrum, a discrete strain value can always be reached depending on the FBG signal response. The importance of discovering the Bragg period of the fiber, is that this is the property that changes with strain, acceleration, pressure, displacement, and temperature. With increased levels of either measurand, the spacing between the gratings or the refractive index of the silica core will increase, resulting in a larger Bragg period. By formulating a direct correlation between the measurand of the system and the Bragg period, a value can always be determined for the Bragg period.

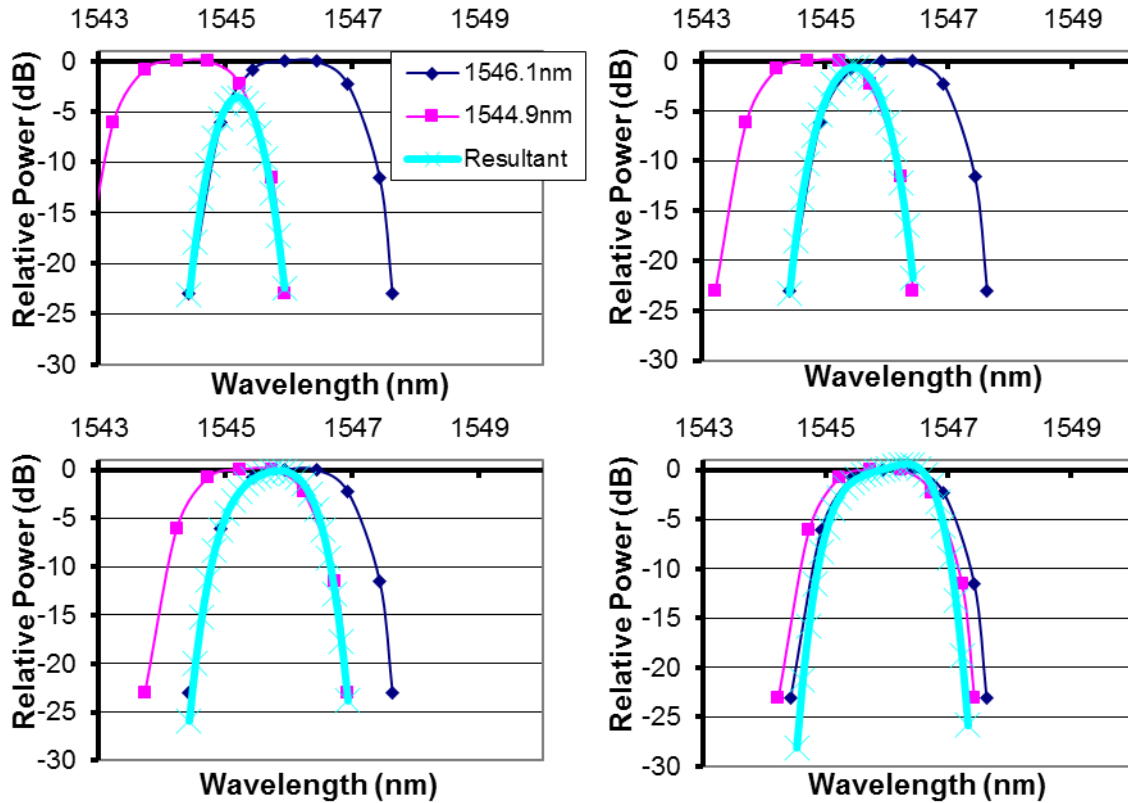


Figure 2.11: FBG spectral wavelength shift showing reflective light intensity.

2.3.5 Benefits and Challenges

The choice to use optical methods over other force sensing techniques is based on the following benefits:

- The thin diameter (200 to 250 μm) is essential as new minimally invasive tools decrease in diameter to access harder to reach joint locations and reduce port size.
- The long, thin dimensions of optical fibers are ideal for tools with shaft-like geometry. Compared to capacitance, pressure, and piezoelectric-based methods which rely upon a distinct area of contact, the fibers are much more economical in size as they are only 160–250 μm in diameter.
- The complex instrumentation can be kept outside, and far away from the tool. This is more relevant to the use of fiber Bragg gratings as the only complex part is the internal mirrors, making the sensor identical in every dimension to a simple fiber insert.
- As the wavelength carried by light is on the order of nanometers, they have a high sensitivity as it only takes minimal bending to increase or decrease the fiber on a similar order. The use of

fibers is therefore critical for the determination of forces that are imperceptible even to human recognition.

- While optical fibers have such high sensitivity, it is useless without high resolutions; conveniently, this is another property of fibers. With the sole dependency on light, opposed to each of the other above sensors, these fibers are immune to electrostatic and electromagnetic noise. In addition to this benefit of high precision, this immunity also makes the corresponding tools useable in MRI machines. This provides immutable value to procedures requiring a combination of high tool precision and high resolution imaging.
- The silica fibers are easily sterilized since they contain no crevices and are resistant to high temperatures. This gives them high biocompatibility. Further benefits in this area are that they have a high chemical inertness, and are non-toxic.

While optics and fiber Bragg gratings have many benefits and applications, the following challenges still need to be addressed while using the technology:

- The fiber needs to be linked to a readout unit. If the device being measured is portable, or frequently in non-fragile environments, the link can be cumbersome, or sensitive to breakage.
- A way to interpret the optical sensor signals being returned must be available at an acceptable cost. The resolution must be maintained, and lower cost, lower accuracy interrogation devices may not be acceptable.
- Fiber Bragg gratings are sensitive to strain, temperature, acceleration, pressure, and refractive index. Isolating one of these parameters from the others, especially when multiplexing the same fiber, is essential to minimizing error.

2.4 Interrogation Systems

2.4.1 Fiber Optic Components and Losses

Isolator – An isolator is a directional component that prevents any internally reflected light from reversing direction and lasing the light emitting system. This could damage internal components and/or change the spectrum being emitted. Especially with the large percentage of reflection with Bragg gratings, this item becomes all the more essential

Circulator – The circulator shown is a directional component with three optical ports that allows transmission of light from Port 1 to Port 2, and Port 2 to Port 3. A circulator allows the reflected

strain-affected light from the fiber Bragg grating sensor to be isolated from the transmitted light. In this way, only a single fiber can be used for both transmissive and reflective light. With small diameter tools, the need for only one fiber path through the tool simplifies the design.

Splitter – A splitter is an optical device that allows a signal to be divided into any number of paths, while also dividing the intensity conversely. This is essential in a ratiometric intensity-based design as it allows one path to act as a reference point, while the other is used for sensing. One novel design, which will be seen in the following sections, is based on the use of a Wavelength Division Splitter, which changes its splitting ratio intensity depending on input wavelength.

Light Source – Every optical system requires a light source. Two main types for sensor applications include swept-source lasers, and super-luminescent diodes (SLD). Swept lasers send out one specific wavelength at a time to the system and locate the current wavelength of maximum light intensity in the system. SLDs send a continuous parabolic spectrum of light over a range of wavelengths. These are used frequently in intensity-based systems, where each returned light intensity corresponds directly to a unique wavelength.

Photodiodes – On the receiving end, photodiodes convert the optical intensity to an electrical signal. By manipulating p-n bandgaps with various materials and fabrication methods, photodiodes can be made increasingly sensitive to specific wavelengths of light. The photodiode takes in the sensor light intensity and returns a proportional current. The ratio between a reference path and signal path can be calculated with this method.

Optical Spectrum Analyzer – An alternative method to photodiodes is the use of an Optical Spectrum Analyzer (OSA). OSAs are able to recognize the exact light spectrum in the fiber with a single fiber input. However, as can be seen in Table 2.1, the cost of this equipment is comparatively very high. Optical spectrum analyzers work by matching the intensity and frequency of the input signal to its full frequency range. An internal transducer is necessary to change the optical signal into an electrical signal.

Interrogator – An interrogator is a “black box” device that internalizes a combination of these necessary components and returns the strain output in a converted, readable, user-friendly form. It simply requires the attachment of one end of a FBG to complete its measurements.

Table 2.1: Costs for primary system instrumentation components.

Optical Component	Cost
Interrogator	\$23,000
Optical Spectrum Analyzer	\$19,240
Tunable Laser	\$2,800
SLD Broadband Source	\$3,000
Long Period Bragg Grating	\$100
Fiber Bragg Grating	\$100

2.4.2 Systems

As the potential of fiber Bragg gratings has been realized, several researchers have investigated the benefits of creating an all-fiber interrogation unit in order to reduce cost. Kersey et al. [38] provides a thorough state-of-the-art discussion on various system developments in the area of FBG sensors. With high signal quality compared to common strain gauges, their range of use has extended from simple proof of concept lab tests, to expensive industrial applications. With the current cost of fiber optic interrogation units, there is a need for developing a low-cost interrogation system in parallel with the fiber optic tools described in this thesis. While the quality of the high-priced off-the-shelf product could be significantly better than the in-lab built system, the specifications of system sensitivity, resolution, and range may be much higher than is required for the arthroscopic application. The following state-of-the-art designs address the issues of temperature-sensitivity of FBGs, strain-sensitivity, resolution, complexity, feedback control, and cost.

Tosi et al. [40] have introduced an in-line sensing system to test the lowest cost system that can still give a good signal. As can be seen in Figure 2.12, the light, which is controlled by a thermoelectric controller, passes through the isolator to protect the laser from self-lasing and then enters the fiber Bragg gratings. They made use of a set of photodiodes paired up with a conditioning unit to amplify signal and reduce noise, and a data acquisition unit to convert signals into strain readings. By using an intricate method of signal processing, the setup costing about \$1,000 gives accuracy to 10 nano-strain, which compares well with systems costing more than 10 times as much. These would include Scanning Filter, FBG Analyzer, Optical Spectrum, and Interferometry techniques. The signal

processing methods use a static-trained RLS filter to reduce the signal-to-noise ratio by 13dB. The only recognizable drawback to this system is the time spent on testing filters in order to reduce noise.

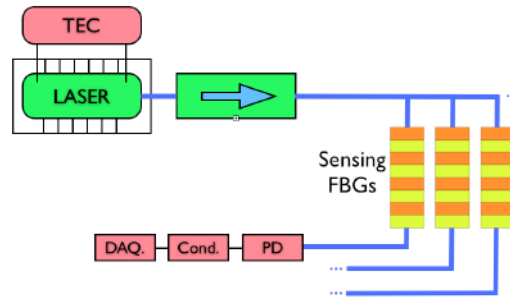


Figure 2.12: Cost-effective strain interrogation system [40].

An all-fiber sensing system created by Davis and Kersey [41] shown in Figure 2.13 uses a broadband source in conjunction with a Wavelength Division Coupler (WDC) to interrogate the gratings. The splitting ratio of the WDC varies based on the signal's wavelength, opposed to a standard fixed ratio coupler, allowing simple intensity-based measurement using photodiodes. This system also uses the back-reflected light from the grating opposed to the transmitted light as in Figure 2.12. This improves the resolution of the system, as the focus is on only one specific wavelength, providing a cleaner signal. Another benefit of using the reflectance spectrum is that a single fiber can then be multiplexed with many sensors, each with a slightly varied wavelength. While these changes add some additional cost to the optical side of the system, a finer spectrum is returned, reducing the needed complexity of signal processing.

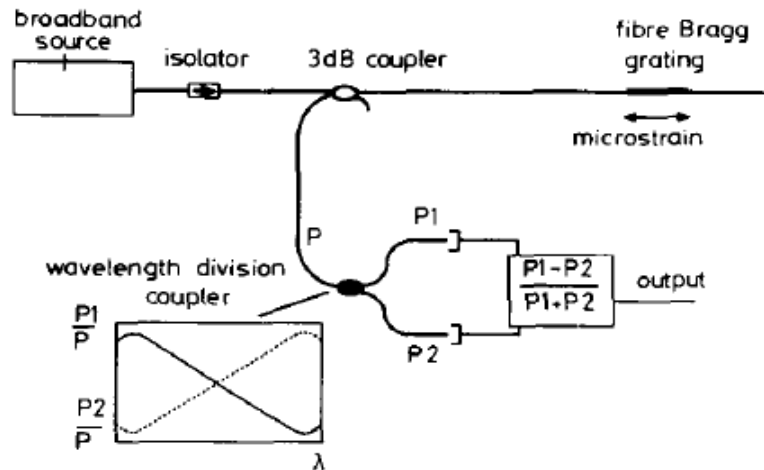


Figure 2.13: Wavelength division coupler interrogation system [41].

© 1993 IEE

One benefit of using discrete 3 cm gratings on a fiber, is that multiple sensors can be inscribed on a single fiber, either to measure pressure, acceleration, temperature, strain or displacement, or a combination of these. Figure 2.14a shows the division of 8 sensors on a single fiber over 6 nm used in the experiments by Sano *et al.* [42]. Each grating then needs to be interrogated by a corresponding set of matched gratings. The arrayed waveguide of matched filters works by first splitting the signal into 8 paths of equal proportions (Figure 2.14b). Using a set of 8 photodiodes as shown in Figure 2.14c will then allow processing of the signals through the concept of varying light intensities. Arrayed waveguides are used in telecommunications to add multiple signals onto a single fiber with negligible crosstalk.

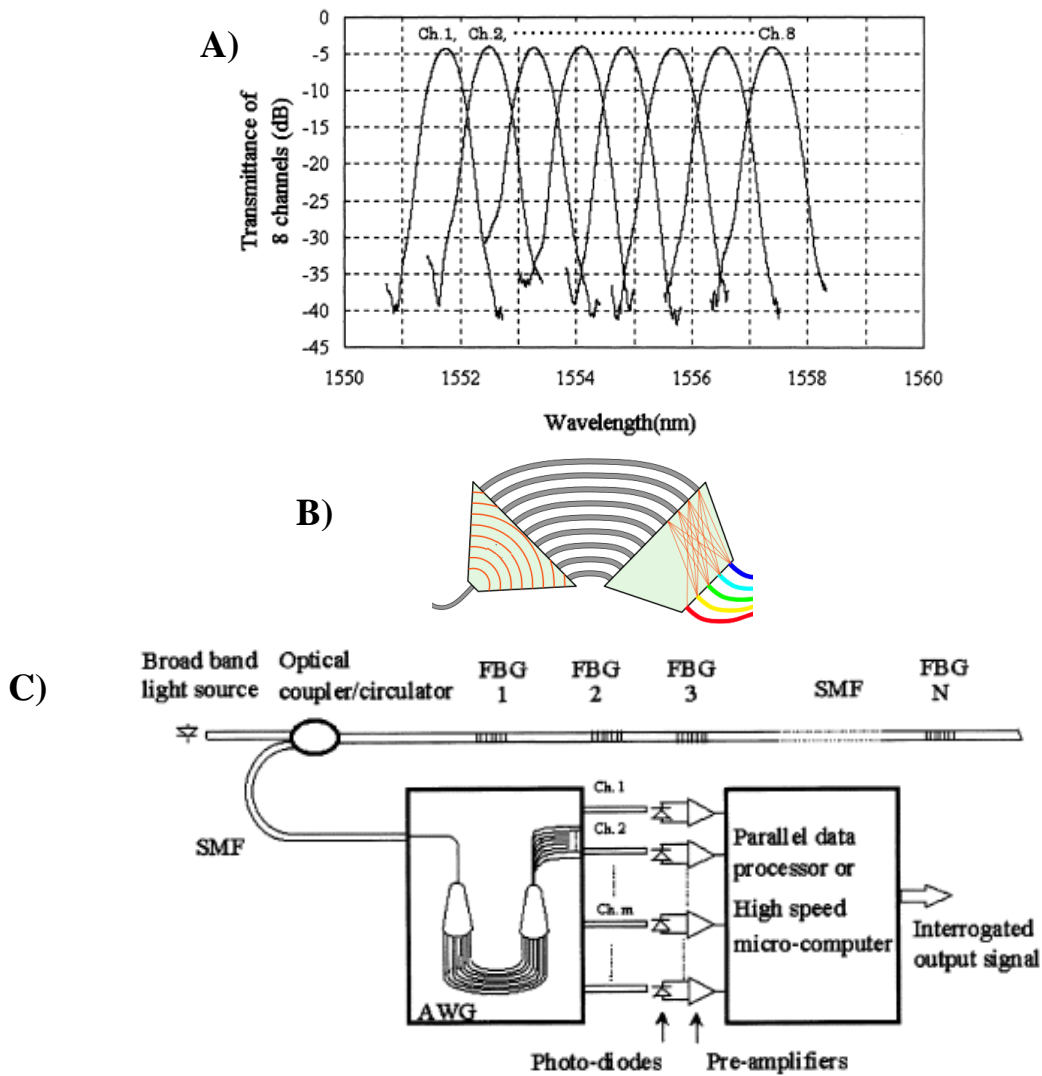


Figure 2.14: Arrayed waveguide interrogation unit
 (a) Channel transmittance levels; (b) arrayed waveguide; (c) sensing system [42].
 © 2003 IEEE

The novelty of the interrogation unit shown in Figure 2.15 is that it uses a dither signal through a feedback loop to sequentially extract wavelengths from each of the 6 sensors over a range of 1530–1557 nm. Davis and Kersey [43] also used a series of matched filter gratings that each in turn will reject light from the reflection of its matched counterpart. A linear response was obtained over ± 100 μ strain, and a dynamic strain resolution of 0.01 μ strain/ $\sqrt{\text{Hz}}$. The total benefit of this idea is that only one photo-detector and path is then needed. The reflection signal of fiber Bragg gratings is already quite weak as only one wavelength of many is reflected, and with the addition of more components, will attenuate even further.

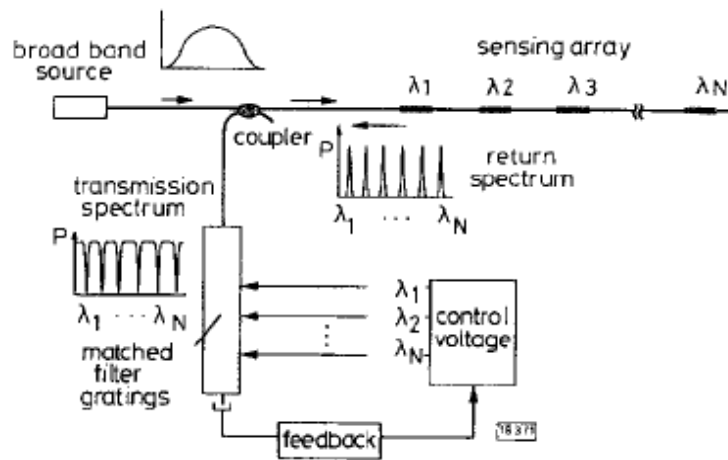


Figure 2.15: Matched filter interrogation unit [43].
© 1995 IEEE

One of the main disadvantages of using fiber Bragg gratings for strain measurement is their dependency on temperature. On the subject of minimally invasive tools where the human body has a different temperature than the atmosphere, the results can be skewed. In Figure 2.16a, Wu *et al.* [43] set up an experimental apparatus to be insensitive to temperature. In this design, fiber Bragg grating 1 (FBG 1) is external to the strained material but in the same temperature environment. FBG2 is inside of the strained device and acts as a strain gauge. As fiber Bragg gratings can be created with very precise dimensions, FBG 1 and FBG 2 were selected as in Figure 2.16b such that they would both shift the same amount under the same temperature stress. The experimental error was recorded as a maximum difference of 6 pm (wavelength) between 15 °C and 50 °C. Under higher temperatures the wavelength will shift up, and vice versa for lower temperatures. In this way, using a ratiometric photo-detection system will give an unchanged ratio under isolated temperature strain. By having FBG 1 attach before the splitter, both the reference arm, and the path with the second

Bragg grating, will be shifted identically. An additional option for this system proposed by the authors is for the splitter to split the signal into three paths with another edge emitter along the third path length. If tuned correctly, this will allow the temperature value to be isolated and equated as well. With the assumption of a 0.01 dB resolution photodiode, Wu *et al.* calculated a temperature resolution of 0.2 °C for the 3-path system.

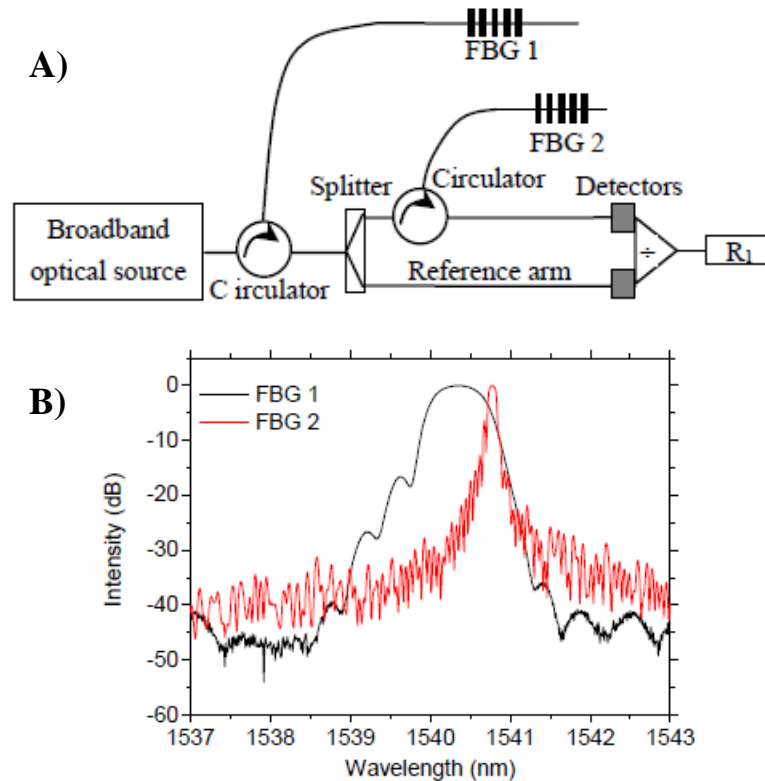


Figure 2.16: Temperature independent interrogation system (a) system schematic; (b) normalized spectral response [44].

In the system proposed in Figure 2.17a by Fallon *et al.* [45], a long period grating is used to modulate the reflected intensity coming from the strain sensing fiber Bragg grating. The splitters, as is common, provide the reference path required for ratiometric photodiode measuring. As can be seen in Figure 2.17b, the broad interrogation response of the LPG dictates the returned light intensity of the FBG. As the FBG spectrum shifts right, its peak will coincide with a lower point on the LPG intensity spectrum. The FBG center wavelength should ideally be kept on either side of the LPG spectrum trough wavelength so that uniqueness of the intensity values is preserved. This system also uses erbium fluorescence as the broadband source spectrum. Erbium fluorescence is produced by the excitement of an erbium-doped fiber through a fiber amplifier. An internal pump laser provides the

initial excitement energy, and on the decent of electrons from higher order states, photons are emitted in a broad spectrum.

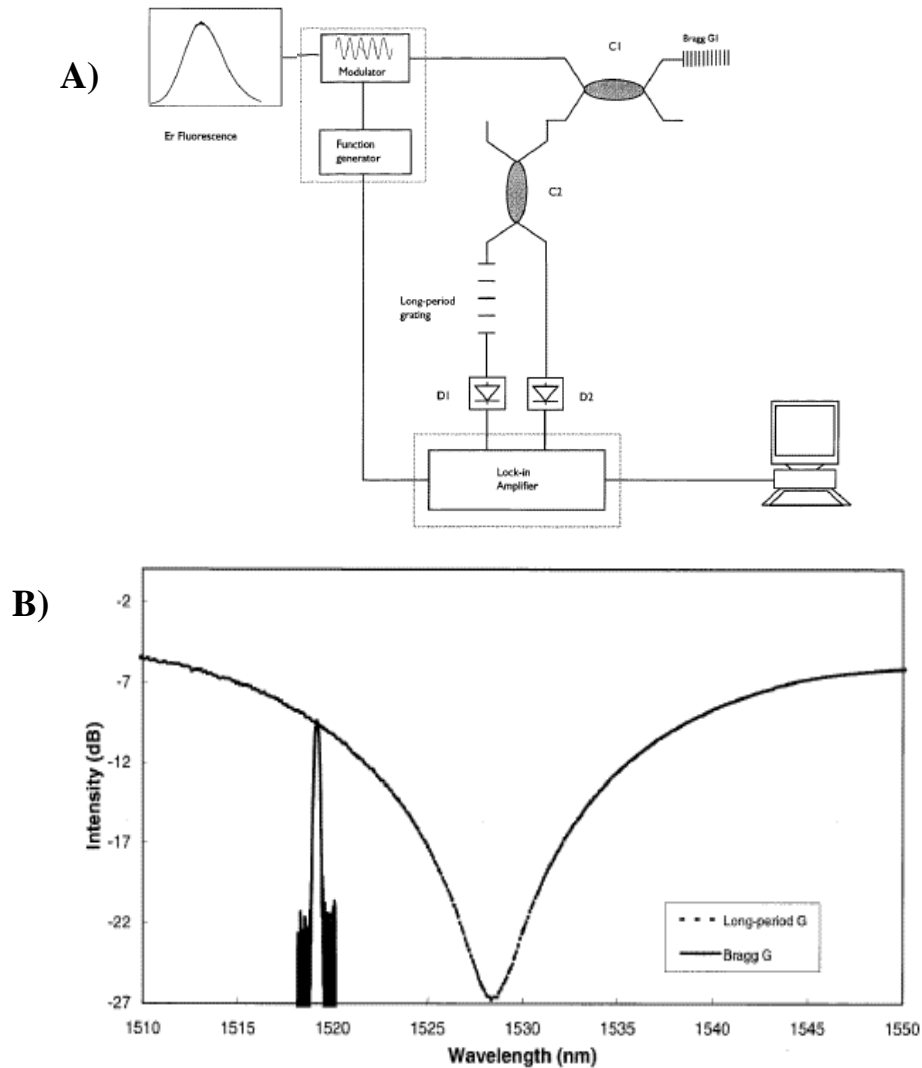


Figure 2.17: Long period grating interrogation system
(a) system schematic; (b) LPG interrogation technique [45].

The next system, proposed by Patrick *et al.* [46], is another long period grating / fiber Bragg grating hybrid interrogation system. The notable difference as can be seen in the Figure 2.18a schematic is that all three gratings (two FBGs and one LPG) are in series along the same fiber, and an OSA is used. Figure 2.18b shows how either side of the LPG spectrum can be used for two different gratings, allowing both strain and temperature to be measured. The LPG is used for temperature sensing as it has a much more sensitive response to temperature, opposite to a FBG which is more sensitive in strain. The center wavelength of the experimental LPG is 1306 nm, while that of the two

FBGs is 1293 nm and 1321 nm. The two Bragg-types are used to medially locate the shifting wavelength of the LPG. An increase in strain causes R1 to decrease slightly, and R2 to increase slightly, as wavelength increases for each. This effect is caused by the mirrored response curve associated with the LPG, and also because the wavelengths of the FBGs increase more than that of the LPG. When temperature changes however, R1 increases a lot and R2 decreases a lot. This is caused both by the mirrored LPG response curve, the fact that the LPG curve is increasing at a greater rate than the Bragg curves, and because the LPG is more sensitive to temperature than the FBGs are to strain.

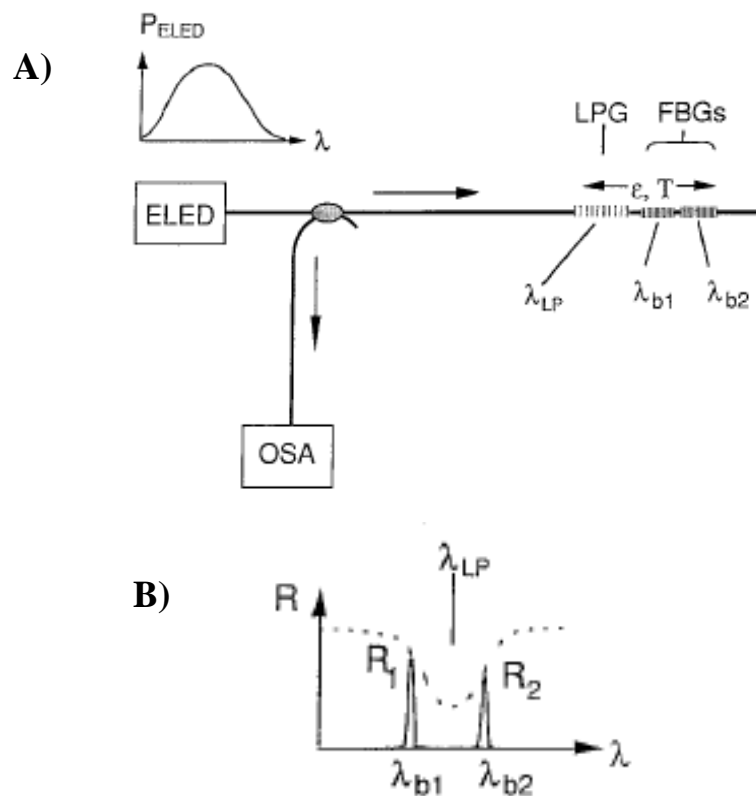


Figure 2.18: Hybrid long period/fiber Bragg grating system
 (a) interrogation system; (b) reflectance vs. wavelength technique [46].
 © 1996 IEEE

Ribeiro *et al.* [47] put forth an all-fiber system that utilizes a bi-conical fibre filter (BFF) as an interrogation unit. This instrumentation design is equivalent to that in Figure 2.19a, with the sole exception of the BFF replacement for the LPG. A BFF is simply a depressed-cladding fiber that operates by propagating a restricted waveset, while heavily attenuating the rest of the signal. The

BFF has a similar response to the LPG seen in Figure 2.19b, with the exceptions that it is more oscillatory and is less deep. These give it a smaller working range, and a less-sensitive interrogation property. While it is generally easier to fabricate, these dissimilarities make it slightly less ideal than an LPG interrogation unit.

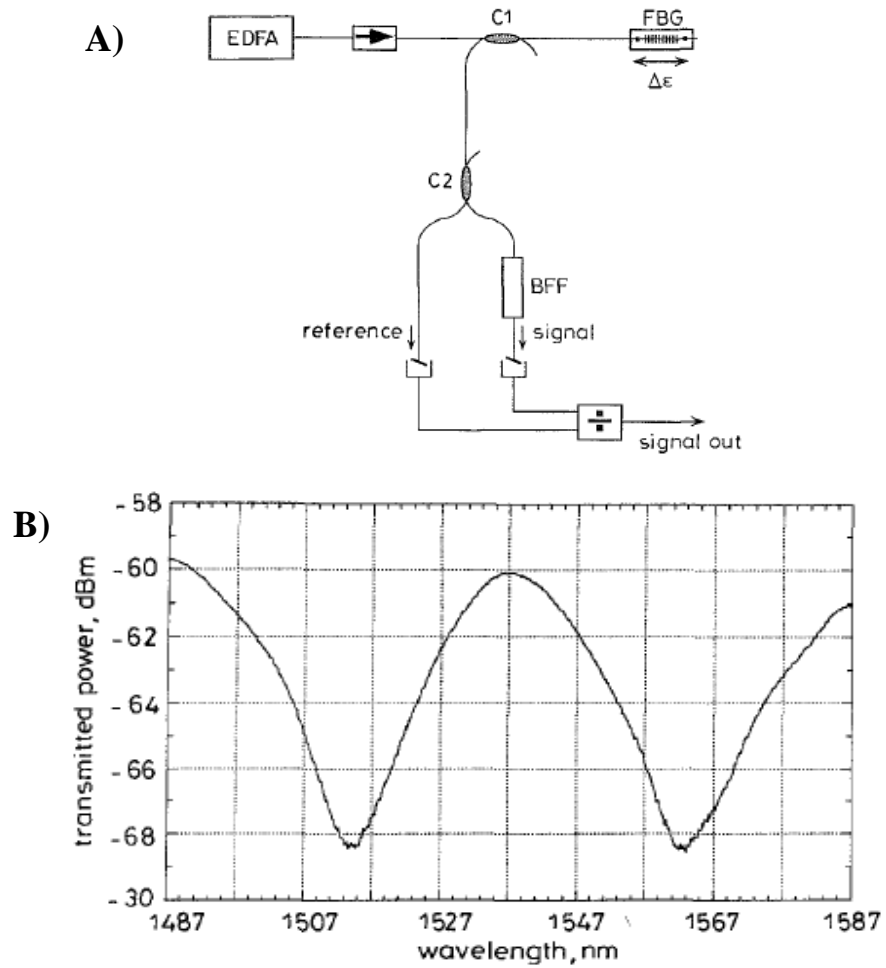


Figure 2.19: Bi-conical filter interrogation system
 (a) system schematic; (b) broad response of a bi-conical filter [47].
 © 1996 IEEE

2.5 Summary

This literature review outlines the existing work that has been done on a variety of components including force feedback, sensor development, optical fundamentals, and fiber optic instrumentation. Force feedback is the central purpose behind developing these instruments. The study of various medical force sensors then provides the experience about how both medical and engineering fields can be joined to create new surgical technologies. Miniaturization, medical compatibility, and sensor flexibility were also emphasized in the review as the driving points behind the mechanical design. By analyzing an assortment of important fiber optic instrumentation designs, an understanding was formulated on how low-cost optical interrogation systems function. The new low-cost system designed from these principles is outlined in the following section of this thesis.

Chapter 3

Fiber Optic, Electrical, Mechanical and Software Design

3.1 Introduction

The presented arthroscopic force sensing design uses fiber optic Bragg grating (FBG) sensors fabricated with UV light imprinting. These sensors have already emerged in a multitude of medical applications [34] due to their relatively simple adhesion and alignment, their high sensitivity [48, 49], and their internal sensing property. This chapter presents each area of development for this system, and analyzes the selection, design, and manufacturing process of each component. These areas include research and design into the low-cost fiber optic interrogation system, electrical circuit board design, mechanical manufacturing of the arthroscopic instruments, and finally the development of the software to visualize the signals and read back the forces. Low-level approaches were implemented in each area to meet the objective of a low-cost complete system: all-fiber interrogation unit, in-lab constructed data acquisition circuit board, self-made tool components, and custom software.

3.2 Design Specifications

The MIS tool was developed with the following list of constraints guiding the design:

1. The overall diameter of the shaft and closed graspers must be less than 5 mm for versatility and to fit through the port.
2. The sensitivity of the tool must be 0.1 N to measure the small forces exerted by the tool on soft tissue.
3. The grasping forces exerted by the jaws on the soft tissue or bone fragments must be measurable between 0 and 20 N.
4. Lateral forces on the tool tip must be measurable between -10 N and 10 N applied 360 degrees around the tool.

5. Tool yielding must occur before fracture as an initial warning to tool breakage. Moreover, any tool fracture must occur outside of the body so that no small pieces are lost inside of the body.
6. To avoid reaction within the human body, or during the autoclaving cycle, the tool must be biocompatible, sterilizable, high temperature resistant, and chemically-inert.
7. An aesthetic and dimensionally equivalent design to current arthroscopic tools will give more similar force data.
8. Unrestricted, low-friction motion of the grasper handle and jaws will give better force measurement, and give better tool motion. There should be no sharp corners on the tool, to avoid accidental tissue cutting or scraping.
9. In order to reduce overall cost, the tool must be fully detachable for reuse with different tips or handles based on the surgical procedure being performed.
10. The software must give live visual force feedback from the sensors, and have a calibration method.

3.3 Low-Cost Interrogation Design

The low-cost characteristic of this system was evaluated solely on material costs, and not on manufacturing or labour costs. It was designed as a low-cost option, constructed in the lab, to aid research into FBG sensor technology, rather than for commercialization. To maintain this low cost, the system was designed as an all-fiber unit (Figure 3.1), decreasing the total interrogation system cost while still maintaining the signal constraints. The figure shows the interrogation of one sensor (of four) through a photodiode (PD), signal processing circuit board (SP) and then to a user interface with force readout on a PC. The PC used for the system is a HP2025 running Windows XP SP3 with an Intel Pentium CPU, 2.80 GHz HDD, and 2 GB RAM. A plastic case was rapid-prototyped with ABS material to hold all of the fiber optic components (excluding the laser) and the circuit board in an organized manner to reduce the risk of fiber breakage or over-bending (optical power loss). This also makes the unit easily transportable.

Final Design Overview – A single-mode benchtop super luminescent diode (SLD) source (S5FC1005S, ThorLabs) was used to provide the system with 1550 nm (45 nm BW) light at 22 mW. The SLD was directly connected to one of nine 1550 nm circulators (3 port fiber circulator, New Focus Inc.) that interrogated the reference fiber. The reference fiber (os1100, Micron Optics), along with the other 8 available sensor fibers, was inscribed with a 1544 nm fiber Bragg grating (FBG).

The refracted light from this grating was input to a 1×8 fiber optic coupler (F-CPL-1X8-OPT, Newport) to ideally power an 8 fiber sensing system (8 DOF). By attaching the reference fiber before the splitter, only one reference fiber was needed. This also gives a consistent reference point between all of the fibers. From the 1×8 coupler, the light from each output is sent through an individual circulator directly to the sensor fiber (Port 2). By using the reflected light instead of the transmitted light as the measurand, the fiber Bragg grating could be placed very close to the tip of the tool. This also allowed the complex interrogation system equipment to be kept far away from the operation site with only the single-mode fiber traversing the space. The refracted light (through Port 3) was directly connected by SC-SC connectors to the photodiodes of the electrical system.

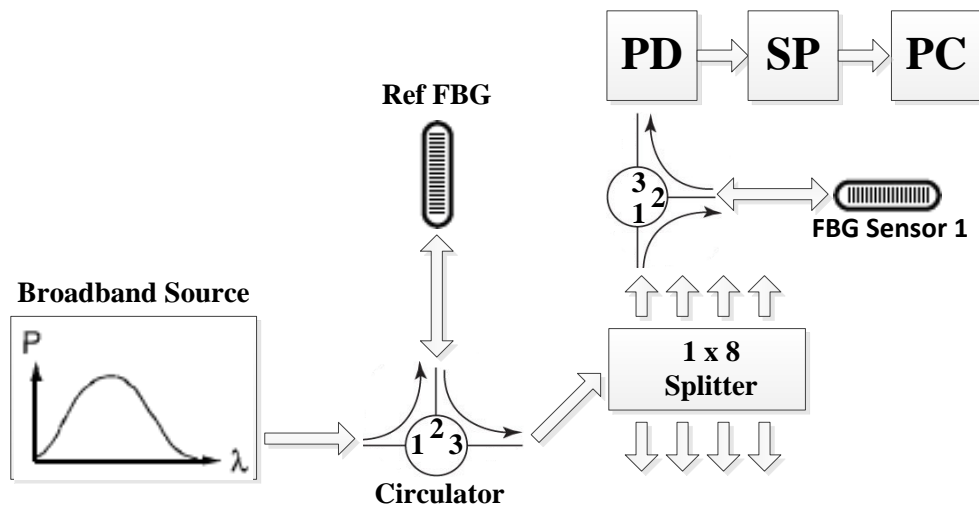


Figure 3.1: Fiber optic instrumentation schematic.

Light Processing – There are four main methods to analyze the light sensor readings returning from the FBGs: directly analyze the spectrum of the light using an Optical Spectrum Analyzer (OSA), use a swept laser source to compare each wavelength output to the wavelength input to determine a match, or use photodiodes to compare the light intensity returning from the sensors. While the first two systems are much more robust, simpler to configure, and more precise, the cost of the photodiode setup was significantly low enough to prompt the question as to whether these benefits were worth the added cost. This thesis work henceforth evolved from a simple high cost solution, to a very complex, much lower cost solution.

A current complete FBG sensing solution on the market at present is an Optical Sensing Interrogator from Micron Optics utilizes swept-source laser technology. By simply plugging in one of the

sensors, the strain on the fiber can be easily analyzed with the provided software. This interrogator measures the wavelength of the light reflected in the fiber, as opposed to the system developed in this thesis, which measures optical intensity. By directly measuring wavelength, the Micron Optics system ignores optical losses in the fiber connections and provides the complete spectrum of returned light.

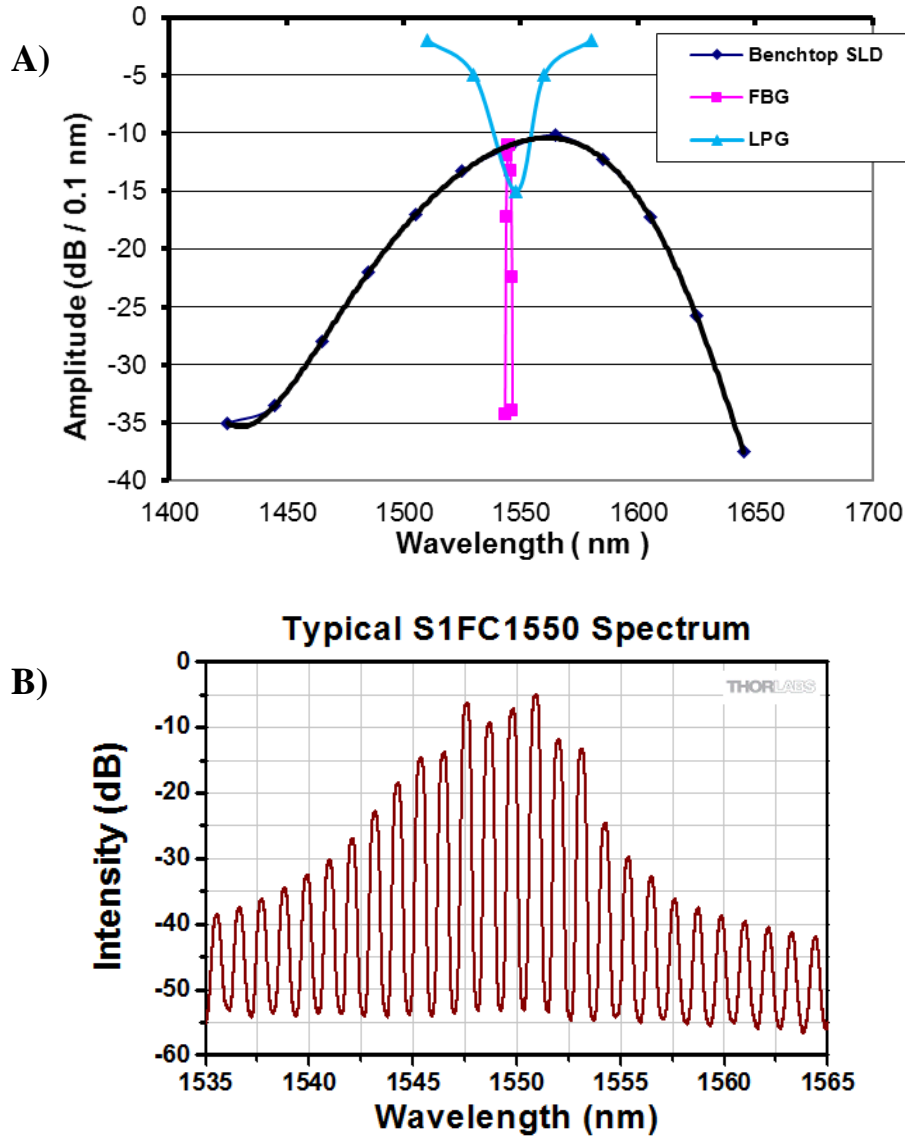


Figure 3.2: SLD and laser spectrums (a) ThorLabs benchtop SLD spectrum; (b) ThorLabs laser spectrum [50].

Power Source – The SLD broadband source selected is composed of an independent, high-precision, low-noise, constant-current source and a temperature control unit. One major benefit of the benchtop source includes the LCD display which shows the current of the internal diode, and a corresponding knob allowed fine adjustment of 0.1 mA to 700 mA at maximum power. The decision to create a system based off of a continuous broadband source rather than a narrow discontinuous laser source was primarily based on system flexibility. For all of the low-level low-cost components that would need to work together, a continuous buffer range of ± 22 nm (45 nm bandwidth) was necessary. The continuity of the power spectrum is important as the interrogation of FBGs requires the measurement of infinitesimally small wavelength intervals. Another benefit of using a broad wavelength range, is that approximately 10 sensors can be effectively interrogated from the single source. Figure 3.2 shows the scale of FBG spectrum to SLD spectrum.

Connectors – The fiber termination connectors that were chosen were standard connectors (SC) due to their connection simplicity. Through research and practice, a suitable connection could consistently be made manually between two bare fiber ends. Additional connections will also be needed as there is fiber wear and breakage. The instrumental cost to setup manual connectorization included a fiber stripper, a fiber splice, cleaning solution, and SC-Quick-Connectors. The manual connection procedure used to obtain highly effective connections is as follows: i) Strip off 6 cm of coating from the fiber optic cable (including jacket) using the fiber optic stripper (Product Name and Number) so as not to notch the fiber; ii) Cleave the un-coated bare fiber section to 4 cm using the fiber splicer (Product Name and Number); iii) Use the fiber optic splice cleaner (Product Name and Number) to remove any dust from the fiber tip; iv) Insert the fiber into a suitable length of furcation tubing (900 μ m outer diameter); v) Slide the black twist lock from the SC-Quick-Connect over the tubing; vi) Slide a rubber boot over the tubing for stress-relief; vii) slide the bare fiber all the way through the SC-Quick Connect until the fiber barely pokes out the end (requires some force); viii) Push the fiber back into the connector using a flat glass plate so that the fiber end is flush with the connector end; ix) Slide the connector clamp to secure the fiber in place and twist on the black twist lock cap; x) Slide a connector into either side of an SC-SC connector for connection. Since there is not a permanent connection between fiber ends, there will be alignment losses. A more suitable method is to use a fusion splicer, which was not available initially, but was used for the second generation system discussed in Chapter 5.

Patch Cable – A patch cable was used to attach the FC/APC (female) connector from the SLD light source to the first circulator (SC connection) of the system. Two types of FC connectors include a UPC end (flat cut) and an APC end (angled cut). Both end connections were tested, and the APC end gave 28% more power than UPC. APC-APC connections are recommended in literature as the lowest loss connection.

Splitter and Circulators – The 1×8 splitter purchased was selected to facilitate a maximum of 8 sensors running simultaneously. It had a wavelength-flattened spectrum to allow consistent splitting ratios among a larger variance of input wavelengths (80 nm bandwidth). The circulators were easy to use and connect, and they allowed the back-reflected light from the FBG sensors to be measured. One interesting phenomenon about the circulator fibers, was that when the fibers were bent more than a 3 cm diameter, there was significant light loss. When the plastic rapid-prototyped cases were made for organization of all system components, this issue was kept in mind.

Fibers – The entire system uses single-mode 1544 nm wavelength fiber. Initially, test fibers were purchased online at a discounted rate with wavelengths of 1528.8 nm, 1544.9 nm, and 1546.1 nm. During initial testing, the two upper wavelength fibers were tested against each other to prove the reference-fiber theory. The 1546.1 nm fiber was used as a reference while the 1544.9 nm sensor was strained. In accordance with the theory described above, the light output slowly increased, and then decreased (Figure 3.3). The difference between the wavelengths of these two fibers was large enough that there was no light interrogation overlap for the first initial small strains on the lower fiber, resulting in no signal change. By using 12 fibers at the same wavelength, the spectrum of these fibers were all initially overlapped, and there was a change in light output at very small strains (high sensitivity).

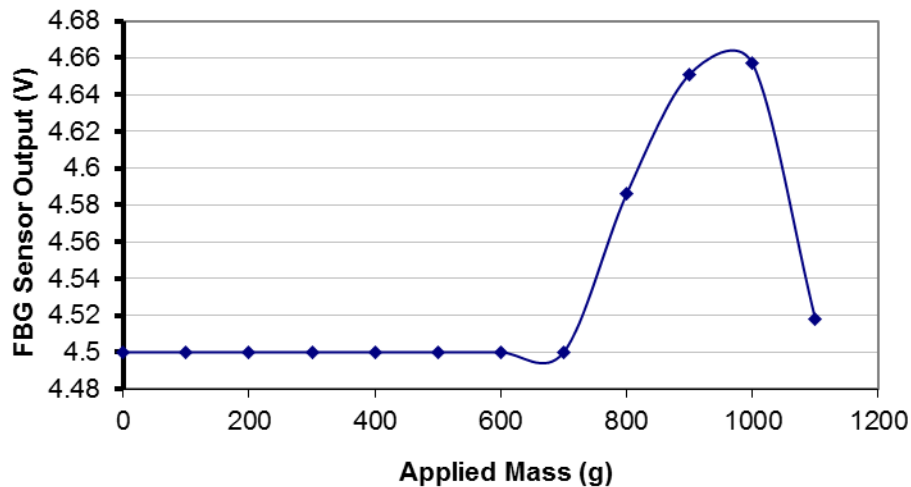


Figure 3.3: FBG response curve with applied weight (1544.9nm sensor and 1546.1nm ref).

3.4 Electrical Circuit Board Design

At the optic-electronic interface of the board (Figure 3.4), 8 high-sensitivity optical fiber InGaAs photodiodes (ETX100, JDSU) are used at a 1550 nm frequency to transform the light into current. These photodiodes incorporated an additional ground pin to further stabilize the signal, and had SC connectors to easily attach to the fiber optic cables. A transimpedance amplifier (OPA381AIDGKT, Texas Instruments) in combination with an 82 M Ω resistor was used to amplify the current output from each photodiode. Prior to the inclusion of the transimpedance amplifier, a simple resistor was used to amplify the signal; however, the resistor also proportionally amplified the noise. An added benefit of this specialized amplifier, is that it amplifies the linearly increasing current, rather than the non-linear impedance. This allowed a direct linear correlation between the received light and the generated electrical signal which eased the signal processing considerably. A “Very Low Noise 24-bit Analog-to-Digital Converter” (ADC) (ADS1256, Texas Instruments) was used to transform the analog signal from the amplifier into a 24-bit digital signal. To clock the conversion rate, a high frequency 7.68 MHz crystal oscillator (CIA/53383, Citizen) was used. This converter was chosen for its 8-pin ADC capability. The fiber optic interrogation system was designed to be compatible with a maximum of 8 sensors, such that future tools could have at least 7 DOF (6 DOF + actuation DOF)

without needing to redesign the circuit board. As specified in the datasheet, there was a tradeoff between frequency and bit resolution for this converter. The final ADC specifications used included a 10 N force-sensing range with a resolution of 0.1 mN, equating to 18.91 noise-free bits. This would provide a theoretical sample rate of 1000 samples per second, equivalent to 75 Hz for 4 fibers. A microcontroller (PIC16F690, Microchip) was used to initialize the ADC, poll for and merge the 24-bit data, and synchronize data transmission, thereby ensuring reliable data transfer.

The code for the microcontroller was developed in MPLAB in Assembly language to maximize the memory available to the microcontroller. A PICKIT3 was used to program the chip. Serial Peripheral Interface (SPI) communication was used between the PIC and the ADC converter due to its typically lower power consumption and its higher throughput compared with I²C. Losses in communication speed were due to the necessity of writing to the ADC, and the associated time delays, when the ADC gate was to be changed. If an internal protocol had been developed by Texas Instruments to automatically cycle through the 8 gates sequentially, the communication rate would be increased by a minimum factor of 2. One issue that has not been solved at present is the tendency of the ADC converter to output a middle value when switching between ADC gates. A temporary solution has been to always poll each gate twice, and discard the first received value, however this again decreases the communication rate by a factor of 2. Further communications with Texas Instrument customer service are recommended to fix this bug.

To communicate with the PC, an FTDI chip was used to receive and transmit data by a UART protocol. A mini-USB connector was added for simple connection to the USB port of the PC. Additional components added to the circuit board include a programming reset button, circuit-protection diodes, and LEDs to signal power, UART communication, and ADC communication on the 4 Input/Output (I/O) pins. The circuit board was designed using EAGLE 6.5.0 Lite PCB software and printed by OSHPARK. The specifications for the board size were to fit all the photodiodes in an easily-accessible, organized manner, and for the total board to fit inside a compact benchtop unit. The designed board and necessary post-processing fixes give a working prototype for system circuitry. Next iterations should decrease the total area of the board, and should fix the EAGLE board drawing errors prior to re-printing. Experimenting with multi-layered boards can also further reduce the total board space requirements.



Figure 3.4: Circuit board design.

3.5 Grasper Design

The manufactured grasper shown in Figure 3.5 is based on the 011024 ACUFEX “Alligator Max” arthroscopic grasper. This robust model was chosen primarily for its simple but highly efficient design. Each joint was designed with such geometry that each part sat flush to the next, erasing the need for any permanent connections apart from those required to seal the instrument and make the tool tamper-proof. Materials including carbon fiber, titanium, stainless steel, aluminum, and Delron (high temperature plastic with low friction) were considered for the tool; however, according to the stress calculations in Appendix IV, the availability and cost of the materials, the effective sterilizability, and machinability, the full tool was manufactured in stainless steel. An additional benefit of this tool is the fixed bottom grasper jaw, which gives the surgeon a better reference when attempting to grasp small tissue samples. While designing the new arthroscopic grasper for force-sensing capabilities, major changes were made to the ACUFEX design to create a fully modular tool with removable components. This allowed a more thorough cleaning and sterilization process, and allowed the tool to be easily tested and redesigned through the development stage. The primary challenge in designing the tool was to design for accurate sensor placement, adhesion, and containment, while considering tool deformation, friction, and biocompatibility. With small overall

tool size being an important objective, further challenges were faced while designing the small tool components for assembly and machinability. An underlying consideration was to eventually use an equivalent tool shaft design to outfit a shaver or probe with force-sensing capabilities.

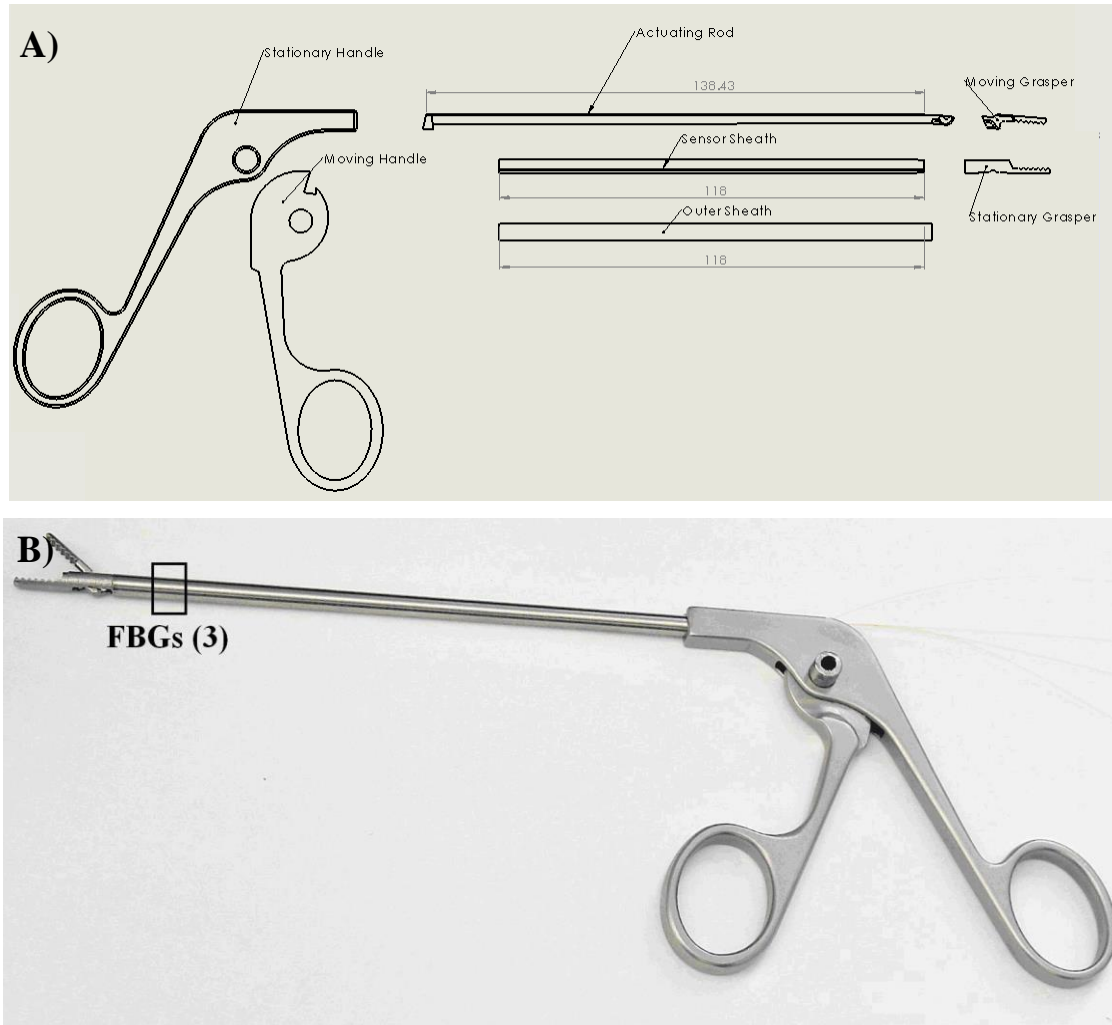


Figure 3.5: Grasper design (a) exploded view; (b) final manufactured design.

Slotted Fiber Shaft—The novel aspect of this arthroscopic grasper is its ability to sense forces applied to the tip and grasping forces. One requirement of this design was to add the sensors as close as possible to the grasper tip to reduce errors through trocar or tissue forces on the shaft of the tool. The use of fiber optics in this design required slots to be made along the tool shaft from the proximal to distal end of the tool shaft. The fibers were to be contained and protected from outside biomaterial to reduce fiber breakage, and to create a smooth interface between the tool and tissue. To further decrease the risk of fiber breakage, a 600 μm (diametric) deep \times 1" long section was cut into the end

of the sensor shaft to allow the fibers to curve back and connect before exiting the shaft (Figure 3.7). By only having one exit point, the three fibers could be contained within a single stress-relief connector and safely connected back to the interrogation unit. The initial sensor curved slot concept was to micro-machine curved slots along the length of the shaft so that the fibers would curve back to one point along a preset path.

The first attempted method to manufacture these slots was to use the in-lab 5 DOF micro-machine. A variety of methods and configurations were attempted with a AlTiN coated 250 μm mill bit (Carbide Miniature Ball End Mill, Harvey Tools). Since this method involved contact with the tube, unlike wire-EDM technology, the deflection and precision errors were too high to make an adequate slot on the thin stainless steel component. The plastic rapid-prototyped triangle jig as seen in Figure 3.6 was used to hold the tube at 120 degree angles. A wire-EDM machine was finally used for machining the slots.

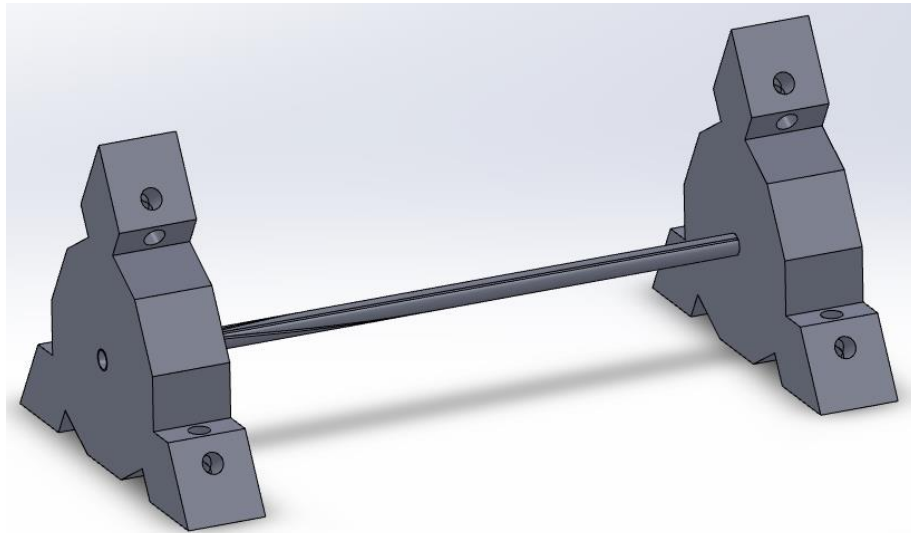


Figure 3.6: Triangle jig assembly for sensor slot micro-machining.

To design for machinability, the slots were manufactured using two concentric tubes, with the slots being machined on the exterior of the inner tube. Three slots, to accommodate three 250 μm diameter fibers, were etched into a 380 μm thick 4.19 mm outer diameter (OD) hypodermic tube (304H08RW, MicroGroup), spaced 120° apart using the wire-EDM machine. Three fibers spaced equally around the circumference is theoretically the most efficient configuration to measure 2 DOF lateral and 1 DOF axial forces on the tip of an extended shaft. The tube was clamped very precisely vertically in the EDM, such that the vertical wire could be positioned adjacent to the tube and cut to

a depth of 300 μm along the x -axis. To ensure an accurate depth of cut, as an error of 80 μm would cut through the wall of the tube, the center of the tube was first indicated for initial x and y -axis center measurements. The x -axis was then further indicated using a software edge-finding protocol. The wire used was 250 μm in diameter, allowing the 300 μm deep slot to be made without directly contacting the metal. The larger hypodermic tube (304H07X, MicroGroup) used to cover the inner sensor shaft and protect the fibers has an OD of 4.57 mm and an ID of 4.22 mm. This gives a clearance of 0.015 mm between the tubes for a smooth sliding connection. The selection process for tube sizes was based on Table 3.1 from MicroGroup. Initially, a 7TW and 8.5 concentric tube pairing was selected for a clearance of 102 μm . The theoretical minimum thickness of the 8.5 gauge inner tube once 250 μm slots were cut into it would be 4 μm . This accuracy had not yet been tested on the micro-machine, and proved to be impossible during fabrication. The current 7XX and 8RW tubes were then selected, which compromised to a thinner outer tube and thicker inner tube. The dimensions of these tubes provided a tighter overall sliding concentric clearance of 15 μm , and a larger minimum thickness of 131 μm for 250 μm deep slots.

The final diameter of the new tool shaft is 4.57 mm, and the length from handle to grasper tip is 17 cm. This concentric slotted tube shaft design, on top of protecting the fibers, allows the fibers to easily be detached from the instrument to reduce costs as different fiber orientations are tested. Current fiber attachment is achieved with light layers of brush-on Krazy Glue and removed with Acetone UN1090, however this slowly degrades the outer protective coating of the FBGs.

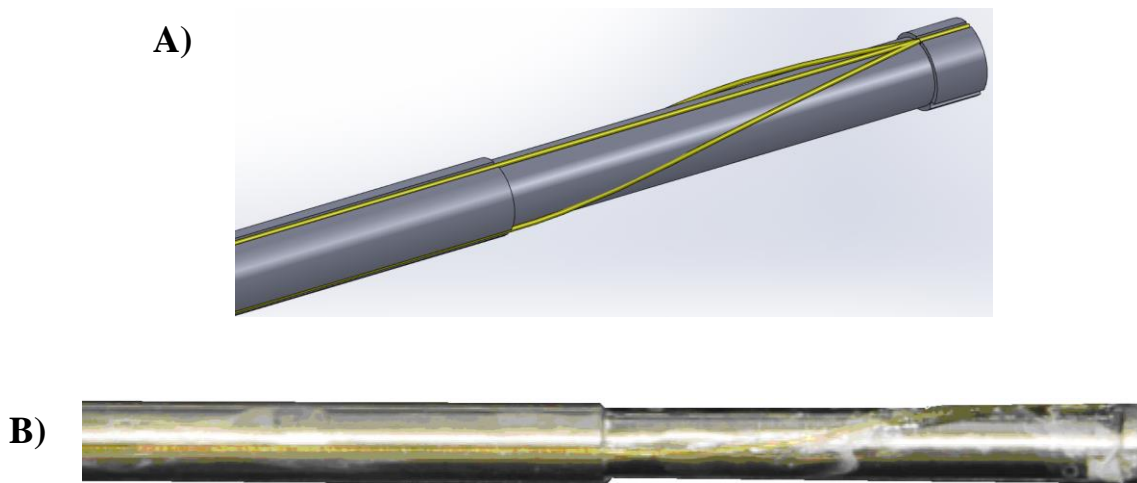


Figure 3.7: Sensor Shaft (a) SolidWorks model of fiber guides; (b) actual instrument.

Table 3.1: MicroGroup hypodermic tubing listing and specifications.

Gauge Size	Nominal Inches			OD		ID		304 SS Item #	316 SS Item #
	OD	Wall	ID	Min	Max	Min	Max		
6 RW	.2030	.015	.173	.2020	.2040	.1700	.1760	304H06RW	316H06RW
6 TW	.2030	.010	.183	.2020	.2040	.1810	.1850	304H06TW	316H06TW
6 X	.2030	.007	.189	.2020	.2040	.1870	.1910	304H06X	
6.5	.1880	.010	.168	.1870	.1890	.1650	.1710	304H06.5	
7 RW	.1800	.015	.150	.1790	.1810	.1470	.1530	304H07RW	316H07RW
7 TW	.1800	.010	.160	.1790	.1810	.1580	.1620	304H07TW	
7 X	.1800	.007	.166	.1790	.1810	.1640	.1680	304H07X	
7 XX	.1800	.004	.173	.1790	.1810	.1720	.1740	304H07XX	
7.5	.1720	.011	.150	.1710	.1730	.1470	.1530	304H07.5	
8 RW	.1650	.015	.135	.1640	.1660	.1320	.1380	304H08RW	316H08RW
8 TW	.1650	.010	.145	.1640	.1660	.1430	.1470	304H08TW	
8 XX	.1650	.007	.150	.1640	.1660	.1475	.1530	304H08XX	
8.5	.1560	.010	.136	.1550	.1570	.1330	.1390	304H08.5	
9 RW	.1480	.015	.118	.1470	.1490	.1150	.1210	304H09RW	316H09RW

Axial Element—The SolidWorks and EDM designs for an axial stress element are shown below in Figure 3.8a-c. The three axial fibers incorporated in the sensor shaft are capable of sensing both lateral and axial forces, however the axial deformation is often significantly less than the bending deformation. Without this element, the fibers could not detect axial deformation in the stainless steel shaft. Initial testing therefore did not include axial force detection, but instead used the additional DOF to average out errors in lateral force detection. The axial element was then designed and constructed in the next generation of the design, with the fibers spanning the element. By adding slots with a wire-EDM at 30 degree intervals in 90 degree pairs over a 3 cm length, the sensor shaft would deform 1.419 μm , and the axial sensitivity vs. bending sensitivity will be increased theoretically by 5.42 times (SolidWorks Simulation). Additional slots can be removed from the shaft if more sensitivity is required. The evenly-spaced slots around the circumference of the shaft, cut in 90 degree pairs, uniformly increase the bending sensitivity and limit twist.

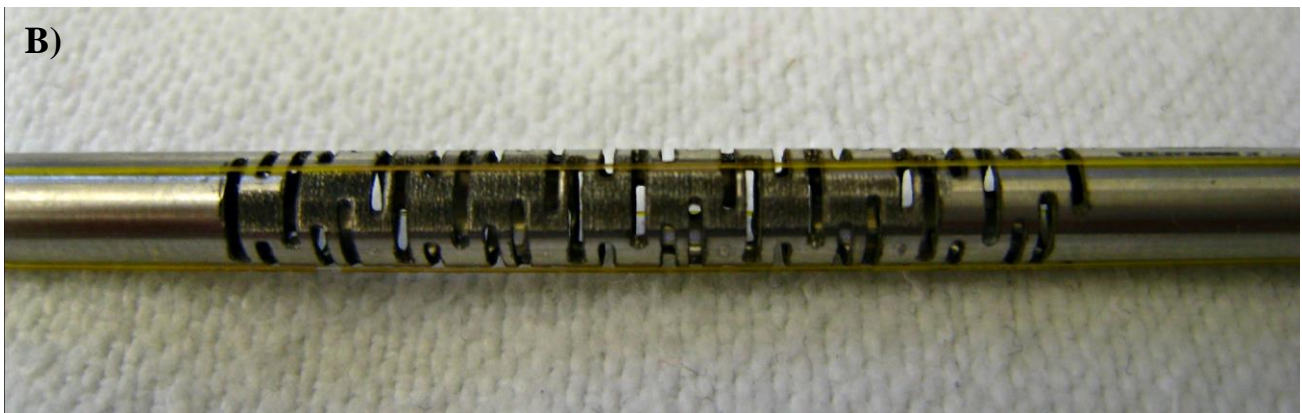
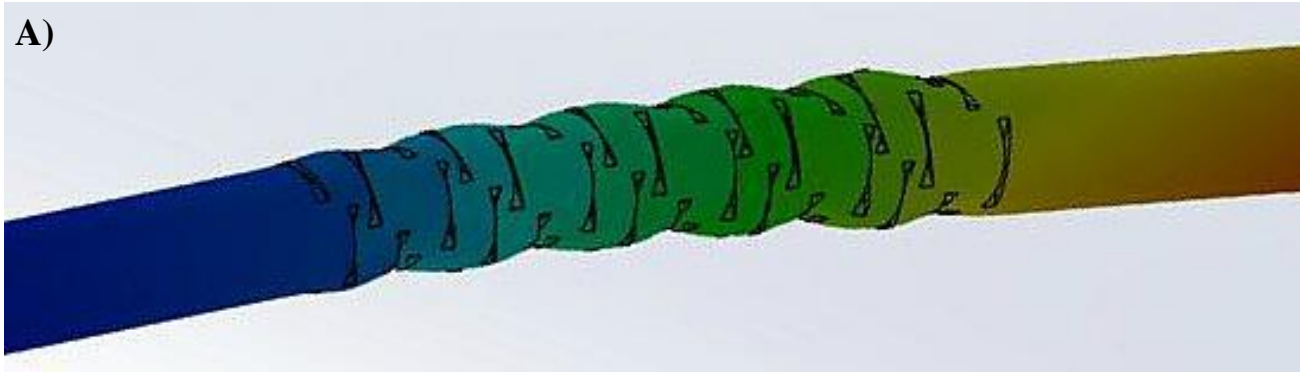


Figure 3.8: Axial amplification element (a) SolidWorks model; (b) EDM manufactured model; (c) EDM setup.

Grasper Jaws — The most complex geometry in the grasper is the grasping jaws, pictured in Figure 3.9 and 3.10. The adopted modular design allowed the jaws to be removed and separated from the sensor shaft during redesigning steps. The proximal end of the grasper jaws was given a double-stepped design to allow attachment of both the small sensor shaft, and the larger overlapping shaft, while giving a smooth continuation between the jaws and shaft. The grasper jaws have 6 lateral teeth for efficient grasping; rounded external edges to prevent tissue snags; and a 1 cm long mouth for large tissue samples. The geometry that linked the actuating rod and the moving grasper jaw in a rotating joint involved an inset cutout that was impossible to machine with conventional methods. Due to this complexity, the parts were produced on a 3-D metal sintering system (DM 125, 3D Systems), resulting in parts that have the same material properties as 316L stainless steel. As the metal sintering system gave a rough finish to the jaws, future designs will experiment with casting for a smoother finish. To give the parts a sliding mate assembly, small diamond files were used to smooth down the fine features. One of the top concerns with jaw design is that the jaw does not come apart while inside the patient’s body. A combination of the design of the curved rotating guide rail and the attachment method to the actuating rod only allows the jaws to attach or detach at 90 degrees to each other, an angle only accomplished when the actuating rod is at least 30 degrees to the sensor shaft. When assembled, and the actuating rod is collinear to the sensor shaft, this angle is impossible.

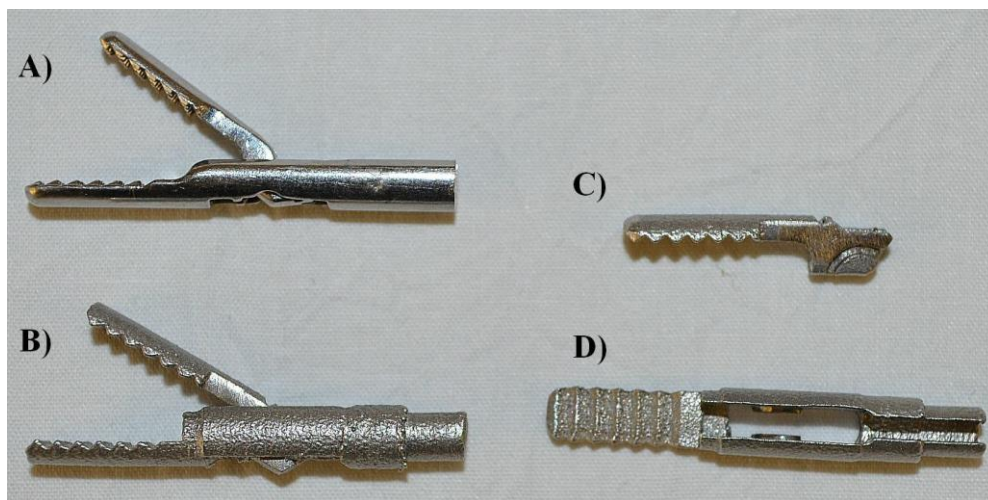


Figure 3.9: Grasper jaws (a) ACUFEX jaws; (b) sintered jaws; (c) top jaw; (d) bottom jaw.

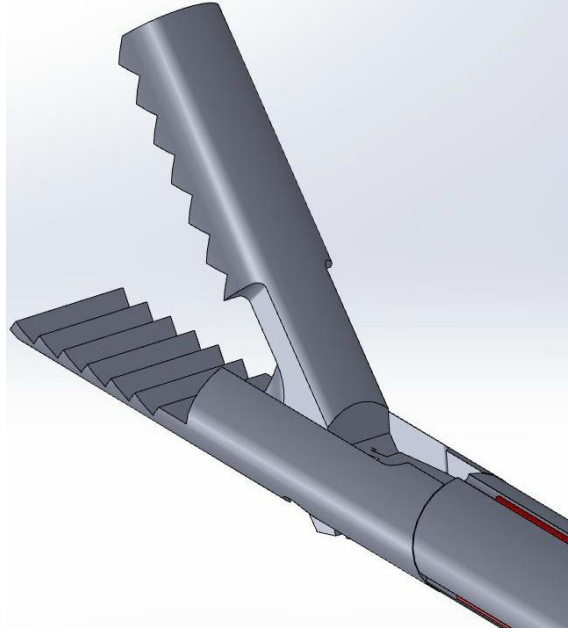


Figure 3.10: SolidWorks jaw model (outer shaft removed).

Grasper Handles—CNC and WireEDM systems were used to fabricate the grasper handles. Alongside some small geometric alterations to the ACUFEX design, Figure 3.11 shows two larger variations: a slot to easily access the fibers, and a removable plug to easily disassemble the handles. A ¼" thick piece of 304 (2B mill finish) stainless steel was used for manufacturing. The profile of the handles was created on SolidWorks, and transferred to the CNC mill. A carbide end mill was used to cut out the oval thumb slot and the profile of the tool. Following this first attempt, a wire-EDM machine was used for the second, current model with the same SolidWorks profile. This gave a much smoother finish, requiring less post-processing. A drill and reamer were used to make the ¼" hole for the handle joint that would hold the removable plug. The slot that holds the smaller moving grasper handle, and the fiber viewing slot, were both drilled and wire-cut. The hole for the outer shaft was drilled with a drill bit equal in size to the shaft for a tight fit. A medical grade finish was applied through a combination of grinding (inline die-grinder), sanding (100, 180, 220, 300, 360 grit), and glass-bead blasting to increase the aesthetics, ergonomics, and biocompatibility of the tool.

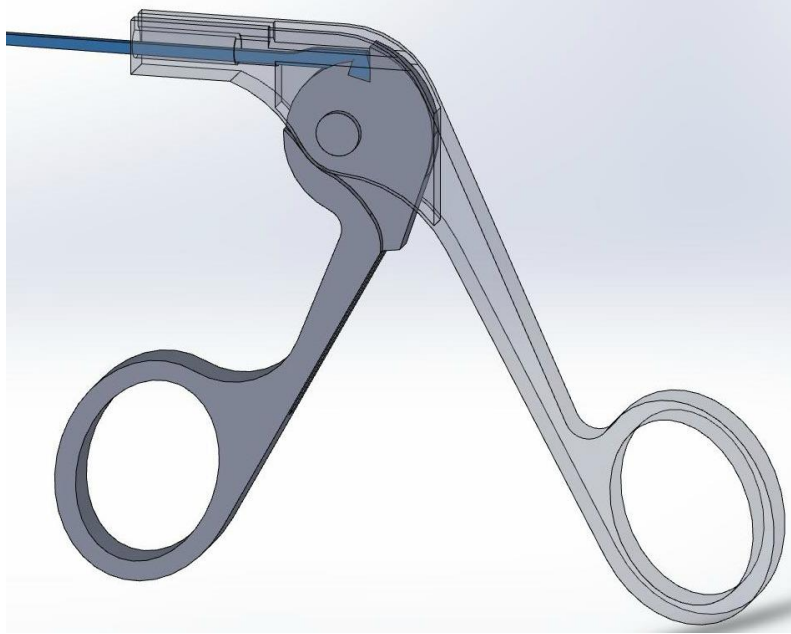


Figure 3.11: SolidWorks handle model.

Actuating Rod – The CNC machine was used to manufacture the actuating rod from the same 304 stainless steel metal as the handles. The SolidWorks profile was again created and used to program in each feature of the rod. The small cuts at the distal end were made with a 1/32" high performance end mill (Figure 3.12). The curvature mates exactly to that of the moving upper grasper jaw, to allow for rotational motion. The proximal end of the actuating rod has a small extrusion that fits into the moving grasper handle for actuation. Due to excess forces applied to the rod during post-processing, the rod bends significantly with applied compression. Future variations of this element should incorporate a more rigid structure than the current 1 mm thickness.

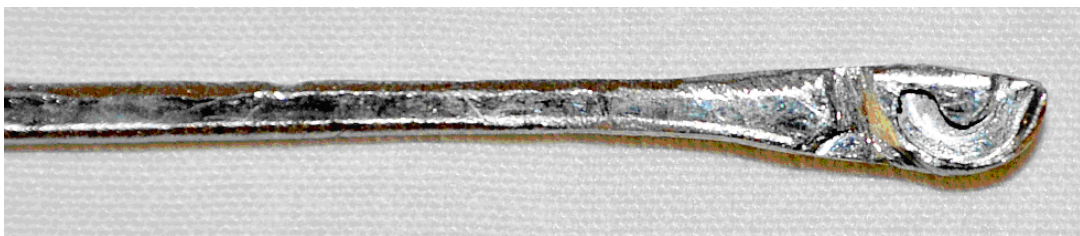


Figure 3.12: Actuating rod.

Miniature Reference Fiber Vice—Since all of the four main sensor fibers are referenced by the same single reference fiber, it is essential to secure this fiber for reliable readings. By adjusting this fiber in very small increments, all of the sensors can be pushed equally into a more favorable linear

region of their respective wavelength spectrums: this will increase the effective sensing range of each fiber. This vice was made from a block of aluminum (Figure 3.13). The block was sized appropriately and squared off, before being cut into two halves. The cut faces were then faced down until smooth. To linearly guide the vice, four holes were drilled into the corners of one face of each vice half, and four dowel pins inserted. Once the pins were inserted, the vice was compressed together, and a hole drilled through the length for the actuating shoulder bolt. The distal block was threaded for the bolt. A washer and corresponding M3 bolts were used to prevent the bolt from leaving its counter-sunk hole, thereby opening the vice instead of removing the bolt. There is approximately 3mm of effective actuation, which is more than suitable to pre-stress the fiber. The vice is $1 \times 2 \times 5$ cm, and so can fit easily into the instrumentation enclosure.

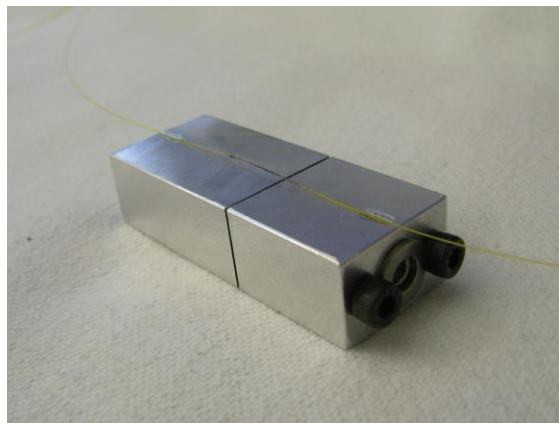


Figure 3.13: Reference fiber vice.

Assembly—To assemble the grasper as in Figure 3.14, the top jaw is first connected to the bottom jaw, and then the tip of the actuating rod is slid into the top jaw at approximately a 60 degree angle. The jaw will not fall off of the actuating rod during surgery since they can only be attached or unattached at this angle: this angle is only possible while the actuating rod is free. Next, the sensor shaft is inserted into the small axial limiting cutout with the lathed section proximal to the tool. The outer shaft is then fit over the sensor shaft, and slid into the nose of the stationary grasper handle. The actuator rod is then fit through the sensor shaft, and the stepped jaw ends are slid into the outer and inner shaft. Next, the spring loaded handle connector is fit into the hole of the moving handle, and the moving handle is inserted into the stationary handle until the spring loaded joint fits into the stationary handle hole. The protrusion on the actuating rod should fit into the opening of the moving handle while it is being inserted.



Figure 3.14: Grasper assembly view
 (a) handles; (b) sensor shaft; (c) outer shaft; (d) actuating rod.

3.6 Shaver and Probe Design

3.6.1 Shaver Design

Fiber optic force sensing ability was added to the current surgical shavers by the addition of a sterilizable slotted metal tube with inset fibers. The shaver being outfitted for force sensing is a Stryker 4.0 mm Cougar Shaver. As seen Figure 3.15, once this model is mounted into the handheld shaver motor, a threaded plastic extrusion is still visible and available for external attachments. By designing the sensor shaft with a female threaded plastic adapter, the shaft can easily be screwed onto the tool. The choice to outfit a pre-made tool opposed to designing an entirely new tool, was based on considerations of time and cost, machinability, blade dulling, and sterilizability:

- By using an existing tool base, the time and cost of design and manufacturing fit into the project limitations.
- To design equivalent effective shaver blades, casting would be necessary; however, this technology was not available.
- Since the shaver blades dull after repeated use, they will need to be disposed of regularly. Using pre-existing single-use instruments as opposed to new designs is therefore a reasonable short-term solution until additional funding can be acquired for the project.
- Existing tools have already proven to be sterilizable, halving the work to be done on sterilizing the full tool.

In order to decrease the risk of fiber breakage around moving parts, the fibers will be sealed in rubber furcation tubing, and will exit the shaft outside the side of the shaft before connection to the shaver motor. Similar to the grasper shaft design, two concentric tubes of 5.56 mm (8987K4, McMaster-Carr) and 5 mm (304M05X.50SL, Microgroup) outer diameters were used, with the inner tube slotted with EDM technology for the fibers. These two tubes, fastened together with adhesive and a plastic connector will then be threaded onto the tool as mentioned previously. This quick-attaching design will add precise fiber optic force sensing to the surgical tool in an easy, detachable manner. Tri-axial fibers will be threaded along the tool, again similar to the grasper design. To increase axial sensitivity, an axial cut element, similar to the grasper design will be made on each of the inner 3 shafts.

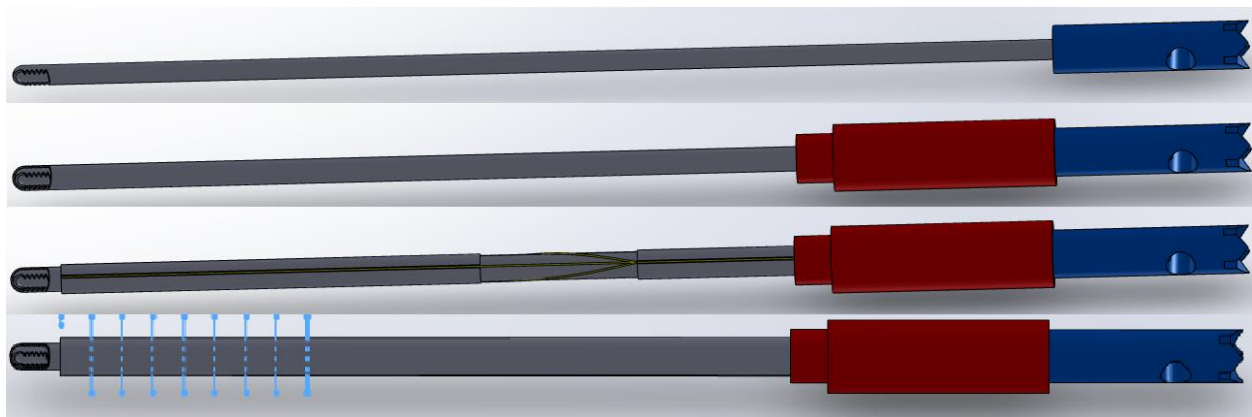


Figure 3.15: CAD shaver assembly view (top to bottom) inner shaver blade; outer shaver blade; sensor shaft; outer shaft.

3.6.2 Probe Design

The probe was designed based on geometry similar to the ACUFEX USA probe model (010246, ACUFEX). The triangular handle seen in Figure 3.16 allows the surgeon easier control of the rotation of the probe and corresponding tip. The inner slotted sensor shaft screws into the tapered probe tip with an M2 thread. The outer protective shaft will then be slid onto the sensor shaft, and then inserted into the probe handle. By threading the back end of the probe handle, a threaded nut can be screwed onto the colleted end in order to compress the two shafts and secure them in place. By adding an axial cut onto the sensor shaft, and since the outer shaft does not restrict the compression of the sensor shaft, axial sensitivity can be increased and thus measured: this will give the probe force sensing capability in x , y , and z . By designing this tool based on a pre-existing model, the identical geometry will already give the tool a familiar feel to the surgeon when used.



Figure 3.16: CAD probe assembly view (top to bottom) slotted sensor shaft (blue) with tapered tip attachment; outer shaft (red); triangular handle with colleted end; securing bolt (blue)

The long hole in the probe handle in which the outer shaft will be inserted will be machined out using the wire EDM. A thin 0.3 mm entry cut will be made lengthwise on the top of the tool so that the wire can access the inner destination. With typical holding of the tool, this entry slot will not interfere with the surgeon's gloves; however, any sharp edges will be smoothed out to prevent accidental tearing. The profile of the tool will also be made with the wire EDM based on the SolidWorks design. The tapered end of the tool will be lathed, and the tip will be bent to approximately 90 degrees using a vice. The straightforward assembly/disassembly will allow the tool to come apart easily for sterilization.

3.6.3 Preliminary Manufacturing

Figures 3.17 shows the initial stages of manufacturing for the shaver. Figures 3.18 shows the initial stages of manufacturing for the probe. Figure 3.19 shows the shaver mounted into the motor)

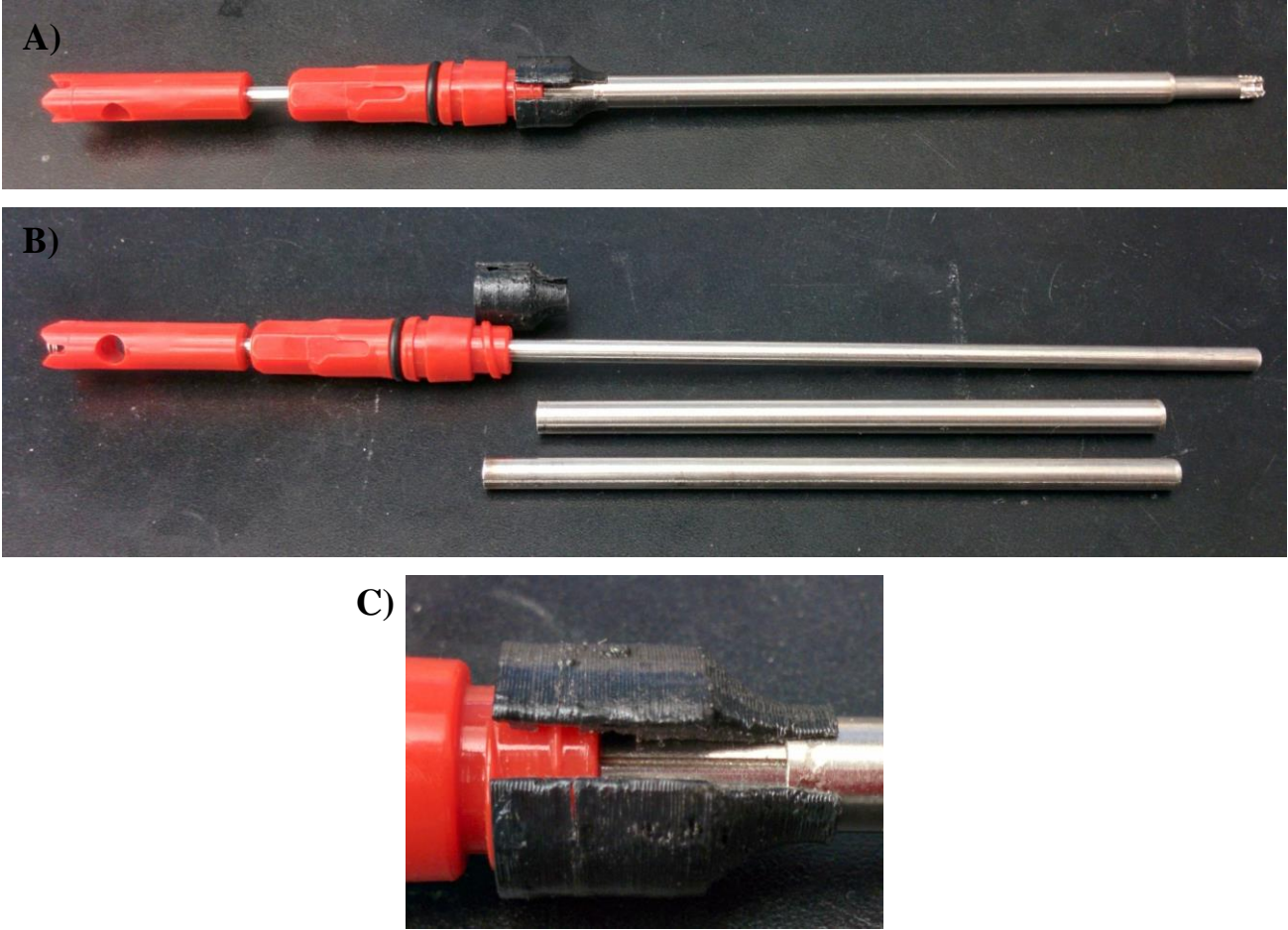


Figure 3.17: Shaver assembly (a) assembled; (b) disassembled; (c) plastic adapter.

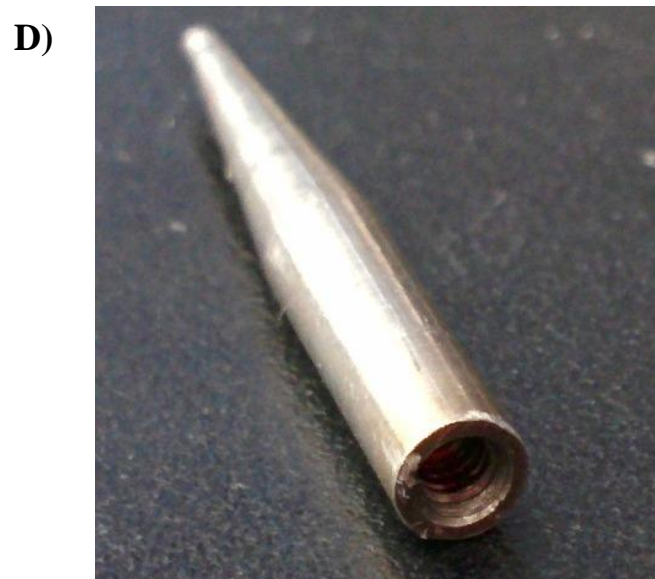
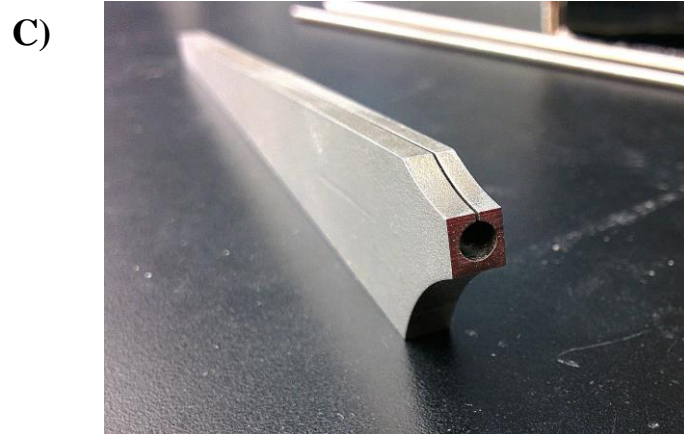
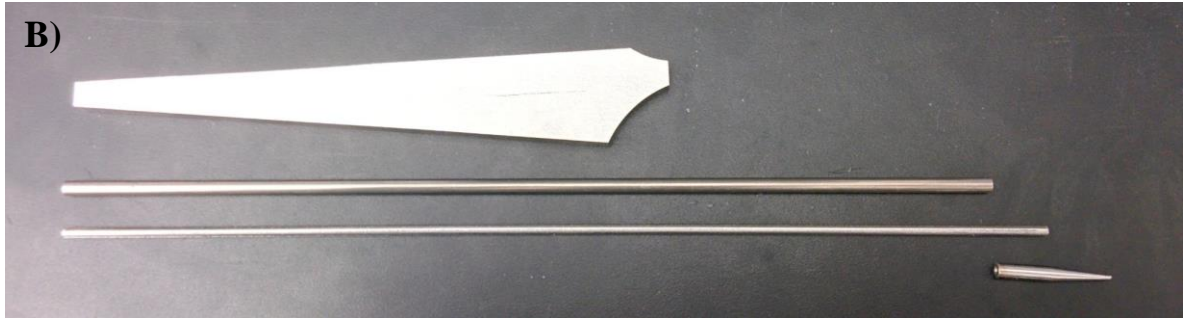
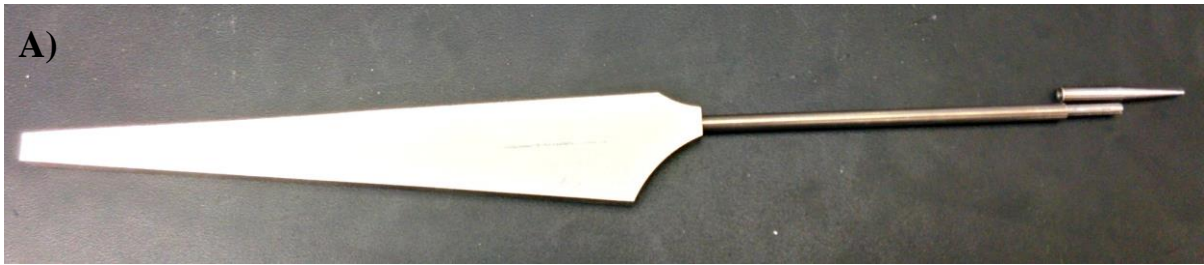


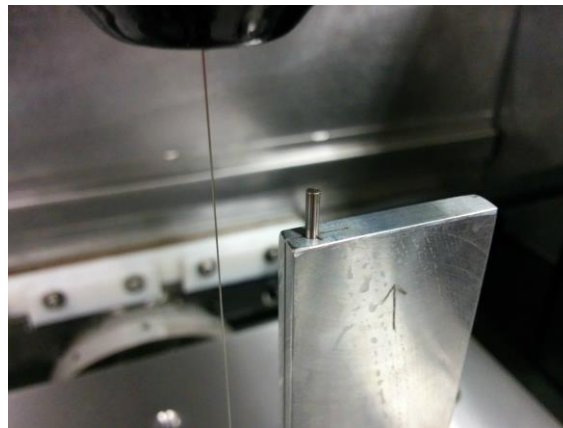
Figure 3.18: Probe assembly (a) assembly without tip; (b) disassembled; (c) handle; (d) tip.



Figure 3.19: Shaver mounted in motor

In order to accurately cut the fiber slots into the thin 2 mm probe shaft, a specialized clamp was designed to clamp the full length of the rod (Figure 3.20). Notches were made at 120 degrees to more accurately locate the slot positions. The clamp was machined on the CNC machine very accurately to micrometer precision so as to minimize the error in the resultant slots. Similar clamps were made both for the Shaver and for the probe, differing by length and by tube diameter.

A)



B)



Figure 3.20: Probe clamp (a) EDM setup; (b) final grooves.

3.7 Software Design

3.7.1 Final Design

The software developed to present the forces interpolated from the FBG signals via a user-friendly interface was written in C++ using the Qt GUI library. The core of the program was based on software previously developed for the SIMIS project [13, 14]. It was adapted for the FBG sensing system by adding low-level serial port communication with the microprocessor, and by removing components such as video feedback that are still being developed for this system. An open-source External Serial Port library was used to manually setup the serial port and read in communications from the microchip onboard the PCB. The FBG signals for all 4 sensors are constantly input as voltages between 0 and 5 volts and recorded at a sample rate of 90 ms. The various screens available on the program are as follows (Figure 3.21, Appendix I): Voltage Plots, Calibration Setup, [Calibration] X Y Z Curves, Grasper [Force] Curve, Force Readout, [Setup] Options. Each of the 4 signals has a different noise level and amplification value along its fiber optic path. Therefore, each is read at a different zero-force value. The values are initially synched to remove system light offsets, for easy visualization and to simplify the mathematics. Another option is auto drift analysis, which allows the drift to be calibrated out automatically when the instrument is not in contact with tissue. This concept is explained more fully in Section 4.4.4. The Voltage Plot screen allows each of these concepts to be visualized using the raw input signals to ensure the proper functioning of the FBGs. The Calibration Setup screen allows the user to create bending and axial calibration curves using convenient push buttons for each interval. As consistent, reliable loading is difficult for the grasper handle, its calibration relies on continuous polling of the ATI-43 force torque sensor. Using the code and libraries provided by ATI, and custom code developed at CSTAR, a method was inserted into the existing FBG sensor program to run the ATI force sensor in parallel with the FBG signals. When the ATI force torque sensor reads an integer force value between -20 and 20 N within 0.01 N error, it records the current FBG signal value. In this way, as the user applies force to the grasper handle, a calibration curve can be made relating the FBG voltage signal to the ATI Force/Torque sensor value. An additional element provided for the ATI force sensor reading is the ability to bias the signal manually. While the code does include the loading of an appropriate calibration file, the user may still opt to create a zero-force reference at a different loading configuration depending on the calibration setup. The next two screens X Y Z Curves and Grasper

Curve, first plot the created calibration points, and then interpolate the intermediary values using an open-source cubic spline library. By reversing the axes of these splines, and limiting the new plot to a linear discrete voltage domain, a single force value can correspond to each FBG signal. Since the spectrum of the FBGs is (positive) parabolic in shape, it is essential to operate either solely on the left side of the spectrum, or on the right side, to maintain distinct force values for each signal value. By equating the contribution of each of the three shaft fibers to the total applied force and angle of applied force, an estimated applied force and angle of application is output on the Force Readout screen. The grasping force is calculated only by the contribution of the FBG on the grasper handle, and thus is presented directly from the grasper calibration curve. The Force Readout screen presents the estimated values numerically and in a real-time increasing and decreasing bar graph similar to the presentation of forces on the ATI F/T sensor software. The Options page allows the user to change the serial port characteristics manually (port number, baud rate, data bits, parity, stop bits, polling time, polling/event driven mode. In addition to all of these options and displays on the full user interface, also included are loading, saving, and refreshing options wherever necessary so that the program can be shut down and still save its calibration files, and so that old tests can be refreshed with new tests.

An issue with the current electrical circuit/software is that the ADC chip outputs a mid-value when transferring from one sensor to the next. As a temporary fix, this extra byte has been read and ignored in the code. This currently doubles the sample rate, from a possible 45 ms to the stated 90 ms. A second problem with the program is that the speed of the communication across the serial port is limited by the computer processing speed; 90 ms is the lowest stable speed that operates the system without risk of noise instability.

While developing the code for the serial communications between the microcontroller and the QT GUI, certain considerations had to be made to optimize the processing power and decrease the code complexity while creating a reliable (noise-free) response signal. A balance also had to be struck between the event-driven timer in the software, the baud rate of the serial communication, and the adjustable conversion rate of the analog-to-digital converter. A polling/event driven combination was chosen to address these issues. Originally, by sending the data continuously at a 38400 baud rate, it was difficult to create a reference stop/start bit that the interface would not confuse with data, and to do this without slowing down the communication significantly. Since 4 sensors were used, it was essential to correctly identify which signal corresponded to which data value. Since each of the

4 signals was composed of 24 bits (3 bytes) each, it was again essential that each of the 3 bytes were aligned correctly. The most reliable and time saving process that was chosen, was to send one byte to the microcontroller to signal the software's readiness to receive all four 24 bit signals. By receiving a constant number of bytes at reliable time intervals, it was easier to check for misalignment of the bytes, or bit read errors.

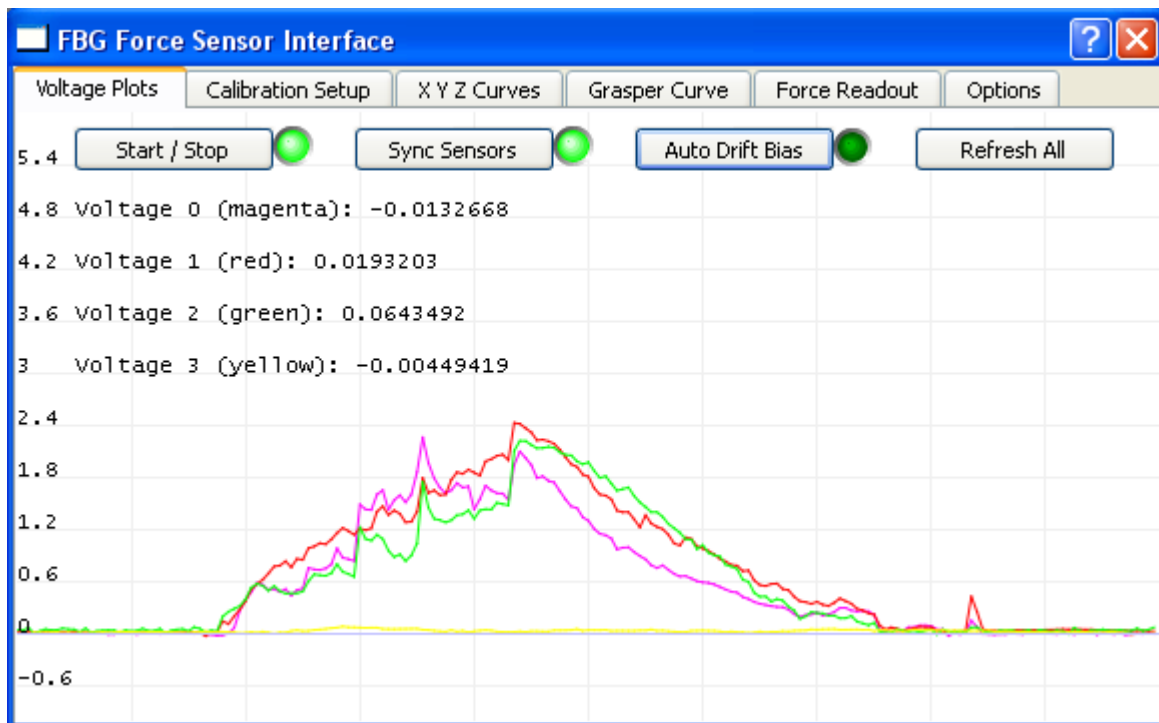


Figure 3.21: Software interface showing 3 signals (bending).

3.7.2 Software Version Development

Version 0 was composed of the code written for the SIMIS system [13,14]. This included video feedback, graph painter functions, methods to handle the data from the DAQ card, calibration procedures, instrument selection, constant mapping of the forces, strains, and voltages of the system, and much more higher-level coding

Version 1 implements direct bit by bit communication with the in-lab designed circuit board using an open-source External Serial Port library in order to bypass the DAQ hardware. Boost and CV

libraries were installed for the graphing functionality. Similar mapping of the forces, strains, and voltages was used in combination with the graph printing functions, however the rest was removed to opt for a different calibration procedure and program more suited to the FBG sensors.

Version 2 includes methods to simply test the communication and reliability of bit transfer with the circuit board.

Version 3 replaced the user interface for the SIMIS system with a simpler GUI more suitable to the FBG sensors so as to minimize code and processing power needed. Various speeds of bit transfer were tested for effectiveness, and methods to distinguish the 8 bit test signal consistently were constructed.

Version 4 includes an attempt to re-paint the constantly-changing overlapping broadband spectrums of both the FBGs and laser source in real time for visualization of the optic properties being manipulated. This visual was abandoned after it slowed down the software considerably with minimal relative advantage. Future software could be developed with higher processing power to include this feature.

Version 5 removed all excess code, and improved the communication protocol in order to have faster transmission. Significant improvement was seen, and the data sample rate was tuned to the fastest speed with minimal bit transfer errors. Event Driven Mode was tested, as opposed to the previously used Polling Mode, to further study the effect on sample rate.

Version 6 implemented multiple byte handling, combining most and least significant bytes, and printing to the graph. This increased the resolution by 4 times (10 bit signal). A simple averaging filter was added to decrease noise, and various error handling methods were added. External Serial Port library was updated to include a method to read a specific number of bytes, opposed to previous readAll method. A fitGraph method was added to visually amplify the signal on the GUI and a user-adjustable calibration function was added. In order to test for long-term drift, an output function sends the voltage value to an excel file every 10 seconds.

Version 7 tested the concept of deciphering which side of the parabolic FBG wavelength spectrum was being read. The noise was too high for the peak of the curve to be determined; however, after

further signal processing, this may be possible. For this reason, the current software relies on staying within the linear region of one side of the FBG spectrum.

Version 8 was the first version to handle the 24 bit signals from the new ADC Texas Instruments chip. Further bit filtering was used to reduce errors. The noise was significantly decreased using the Texas Instruments impedance amplifier instead of a resistor; therefore, the averaging filter was removed. A receive error handling method was added to the microchip code.

Version 9 added a sync function to bias all 4 sensor signals to zero. A zero estimation method was included to test automatic drift compensation under a low fluctuating signal. Further tuning and code optimization was done to increase the sample rate. The method for polling the microchip for each set of four 24 bit signals was created.

Version 10 is the current version, described in Section 3.7.1.

3.8 Summary

The detailed analysis presented in this chapter of each individual component of the design serves to highlight the multi-disciplinary approach used to address the stated design specifications. This entailed gaining a complete understanding of the fiber optic components and how the optical signal is transmitted and affected, including how to interface the optical components with other modules and the losses this may cause. A custom circuit board was designed that, while not fully optimized, serves to convert the light signal to a high-resolution electrical signal. From the mechanical perspective, the detailed and effective designs of a grasper, a shaver, and a probe are presented. The manufacturing of the small precision features of these instruments required a range of specialized manufacturing techniques. This included the machining of the fiber grooves on the sensor shaft, the designing of the complex metal sintered grasper jaws, and the finishing techniques applied to achieve the required tolerances for each part. The addition of a software program allowed the system performance to be easily visualized through each step of the design and was an important tool for instrument calibration.

Chapter 4

First-Generation Prototype Evaluation

4.1 Introduction

The first functional arthroscopic grasper prototype lacked the axial sensitivity required to sense tissue pushing and pulling forces; however, it successfully and accurately measured the applied bending and grasping forces. The tool was then altered slightly (as presented in Chapter 5) to increase the axial sensitivity of the system: the proximal end of the sensor shaft was mechanically fixed and an axial spring-like element was designed for the sensor shaft. The two main techniques in the literature to read the strain values from the tools are either to use an optical spectrum analyzer and theoretical Bragg wavelength equations [16], or to use a low-cost system to produce a reference calibration curve between applied strain and refracted light. For the results presented in this chapter, the low-cost approach was used and the tools were loaded using a calibration procedure to obtain meaningful results.

4.2 Calibration

4.2.1 Sensor Shaft Calibration (Axial)

The four sensors on the tool are capable of measuring x , y lateral, and z axial forces at the tip (3 sensors), as well as measuring tip grasping force (1 sensor). Under axial loading between ± 20 N within the axial test jig (Figure 4.1), the tool began to deflect in bending (as concluded from the sensor readings), before showing a change in force that signaled axial extension or compression. A pure axial load is indicated by the signal dropping (compression) or rising (extension) amongst all three shaft sensor signals; however, this was not seen, and so a resultant axial force could not be obtained. This result indicates that the grasper sensor shaft does not have a large enough axial-to-bending sensitivity ratio to read all of the loading combinations distinctly. The testing jig consisted of an ATI Nano 43 force/torque sensor attached to a Zaber Tech linear stage. The handle was fixed to a base, while the jaws were set into a jaw-shaped plastic component attached to the force sensor. Incremental steps of the linear stage gave readings on the fiber optic sensors and ATI sensor simultaneously to determine the force–strain relationship.



Figure 4.1: Axial calibration apparatus.

4.2.2 Sensor Shaft Calibration (Bending)

Since the axial sensitivity was too low, the third shaft sensor readings were instead used in bending calibration to average out the errors between the other two shaft sensors. In future tool generations, this fiber will be used to measure the axial force of the instrument. The 1 cm grating in each of the fibers is positioned from 3 cm to 4 cm on the distal tip of the grasper jaws. The importance of adding the sensor gratings at the instrument tip as opposed to the proximal side of the grasper shaft is to eliminate any external forces caused by interaction with the trocar/entry port. The x and y tool forces were measured by hanging weights from 0 to 500 g in 100 g increments in each direction on the second tooth of the lower grasper jaw in a cantilever configuration (Figure 4.2). The support point was located 1 cm from the shaft–handle connection, for a cantilever arm length of 13.25 cm. The tool was rotated manually in 60-degree intervals for a total of six positional measurements within the calibration jig. The signals from each of the three fiber sensors were recorded at each weight and position. This process was repeated 8 times to give a total of 480 readings per fiber.



Figure 4.2: Bending calibration apparatus.

Reference curves were chosen for sensor calibration, instead of theoretical values, due to uncertainties in grating precision, location, spectrum shape, and power loss. The calibration curves for the three fibers from -5 N to 5 N can be seen in Figure 4.3, where the vertical axis represents the equal-amplification voltage output of each signal. Eleven readings were taken while each sensor was in maximal tension (inline with the applied load) or maximal compression (180° from the applied load) over the 10 N range to formulate the three calibration curves. The nonlinearity is caused by overlapping of the parabolic spectrums between the reference and sensor FBGs (see Figure 2.11).

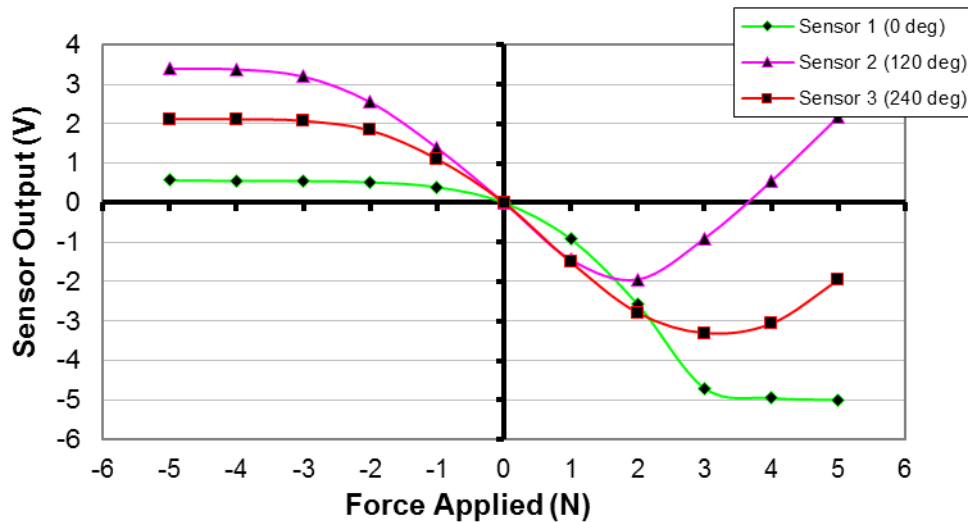


Figure 4.3: FBG calibration curves.

4.2.3 Grasping Calibration

The grasping force FBG sensor was placed on the 2.5 mm thick stainless steel member of the moving grasper handle, approximately 2.5 cm from the load point of the surgeon's index or middle

finger and 4 cm from the handle fulcrum. As the grasper moving handle is part of a 4-bar linkage with the moving grasper jaw, connected by an actuating rod, this sensor position was ideal for a grasping force relationship, and was not coupled to any other forces on the grasper tip. The friction within this linkage was minimized by smoothing the components until the force of gravity on the moving handle could actuate the jaws alone. For calibration, the grasper jaw tips were secured on a two-plate rapid-prototyped plastic jig with each plate fastened to either side of an ATI Nano 43 force/torque sensor (Figure 4.4).

Force was applied normally to the movable grasper handle while two fixed mounts secured the rest of the tool. To formulate the calibration line, 44 FBG sensor and F/T sensor outputs were recorded simultaneously between 0 and 20 N in 6 increasing and decreasing loading cycles (Figure 4.5).

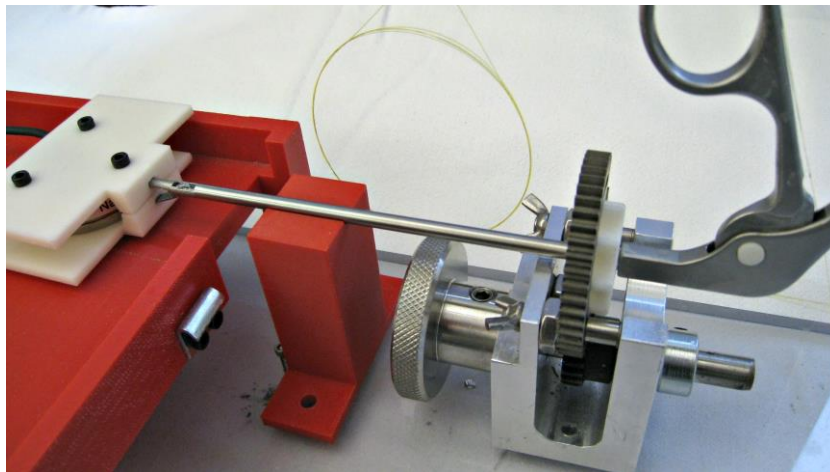


Figure 4.4: Grasper calibration apparatus.

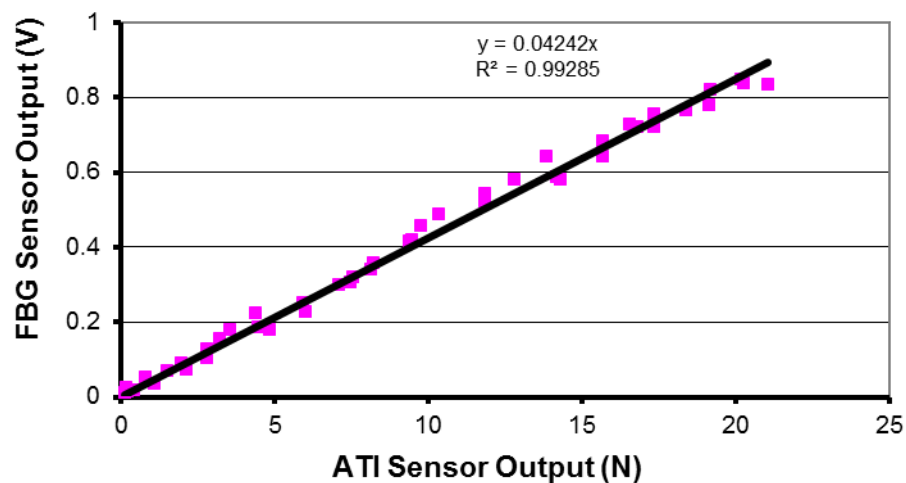


Figure 4.5: Grasper force calibration.

4.3 Performance Assessment

To assess the sensing performance of the final prototype, the total resultant tip force measurement, and an angle approximation of the direction of the applied load referenced to a vertical axis (Force Angle) were measured for the sensor shaft. For the actuation force, the total force applied by the jaws was measured. The performance of the FBG sensors was assessed based on the following measurements, and formulated in Table 4.1:

- i) Accuracy: The RMS error of the shaft sensors was determined from 469 additional readings by again hanging weights from 0 to 500 g in 100 g increments at 60 degree rotations. The weights were fully removed before rotating the instrument. The signals from the 3 fibers were taken and equated to predict the corresponding zero strain neutral axis (NA) as displayed in Figure 4.6. Both the total applied force and the angle of the applied force, referenced from the top of the instrument (0°), were calculated from these values based on the calibration curves. The RMS error of the grasping force was determined by again applying increasing and decreasing forces to the handle over the range of 0 to 20 N. 76 sensor readings from 6 iterations were used for grasper force prediction measurements based on the grasper calibration line and compared to the readings from the ATI sensor.
- ii) Repeatability: The maximum standard deviation (σ) was evaluated for the sensor shaft in 8 repetitions using the same method described above for accuracy. Six loading cycles were performed to assess the repeatability of the grasping force from 0 to 20 N.
- iii) Hysteresis: The RMS error was calculated between the increasing and decreasing load values of both the sensor shaft and the grasping sensor using the same data obtained in the accuracy assessment.
- iv) Signal Drift and Noise: The signal drift was evaluated after 10 minutes under both a 0 N and a 1 N load. The maximum signal noise was evaluated after 30 seconds per fiber. Both tests were conducted in the linear range of the FBG sensor for consistent results. A 10-minute drift time was chosen to simulate the maximum continuous time in contact with tissue. The auto-biasing method described in Section 4.4.4 will compensate for drift when not in contact.
- v) Sensitivity: The minimum sensitivity of the sensors in their linear range was tested by applying force to the grasper tip and grasper handle until the signal was visually discernable from the noise.

vi) Resolution: The maximum effective resolution for this system is limited by the Analog-to-Digital Converter, which gives a 20 bit noise-free signal at the 10 Hz 4-fiber frequency (the minimum frequency estimated for effective visual feedback). The resolution was distributed over a ± 5 N load range.

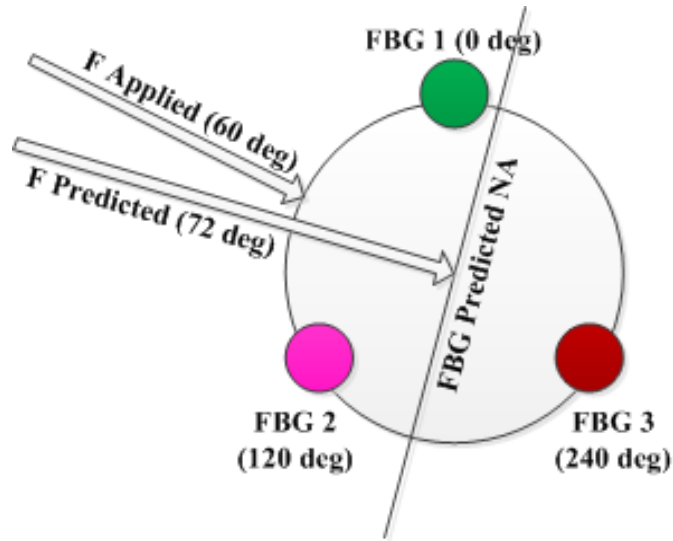


Figure 4.6: Force and angle prediction at 60 degree applied load.

Table 4.1: FBG sensor calibration assessment.

	RMS error	Max σ	Hysteresis	Noise / Drift
Tip Force (N)	0.213	0.169	0.133	0.075 / ⁻¹
Force Angle ($^{\circ}$)	4.37	3.87	5.65	0.075 / ⁻¹
Actuation (N)	0.747	0.804	3.54	0.075 / ⁻¹

¹ No discernable drift

4.4 Validation of Force Calibration

4.4.1 Sensor Shaft

The measurements taken from the three fibers at each of the 60° increments were tabulated and equated based on their corresponding locations to give a maximum resultant force and an angle of force application. Figure 4.7 shows the relation of the lateral forces compared to angle of tool rotation. Three paired combinations of the three sensors (1–2, 1–3, 2–3) were evaluated. The RMS error in the average force prediction was 0.213 N (nonnormalized). The error in the averaged angle

prediction was 4.37° . These values are predicted to be suitable for surgical applications, however future *in vivo* testing will be required to confirm their suitability.

An ideal case was also considered, where the sensor pair with the lowest error in each case was used for calculating the overall error. This resulted in average force and angle prediction RMS errors of 0.023 N and 3.87° . This result points out the high precision that is possible with these sensors. The most accurate fiber pair was Fibers 2–3, which solely predicted a nonnormalized force RMS error of 0.345 N and an angle RMS error of 5.25° . If Sensor 1 is to be used for axial sensing in future designs, this result shows that the remaining 2 fibers will provide high accuracy by themselves. Further improvements in fiber placement, angle measurement, and weight application will help to reduce errors further and reduce dissimilarities between fibers. The calibration curve was also made with a least-energy spline method to join the discontinuous sample points; additional points for this curve could give more accurate results.

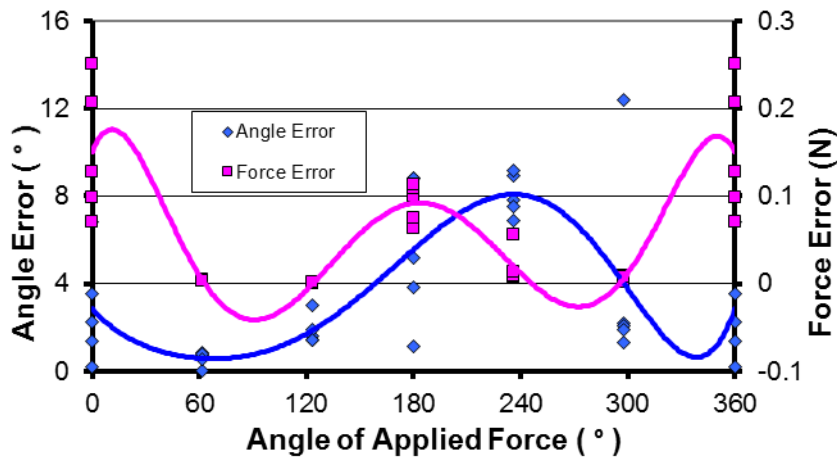


Figure 4.7: Accuracy errors vs. angle of applied force.

It is important to note that the linear range of the fiber sensors in the sensor shaft calibration curves (see Fig. 4.3) only extends for approximately 5 N over the 10 N loading range. Also, as the applied forces get larger in Sensors 2 and 3, the uniqueness of the sensor output data dissolves. To address both of these issues, the tool should be made stiffer in order to extend the linear output of the tool strain in both loading directions. While this change will, alone, slightly decrease sensitivity, improvements in signal processing will help counteract this effect. Additionally, for best results, all of the sensors should be pre-strained in a way that the center of their linear region is approximately at the zero loading condition. Further methods should be developed to accurately pre-strain the fibers

on the sensor shaft. In contrast, resolution is maximized and noise is minimized over the ± 2.5 N load span with the narrow linear region. For tests that only require forces in this range, this setup is ideal. As the loading range increases, resolution will slightly decrease and electrical noise will have a more significant impact.

4.4.2 Grasping

The grasping force sensor was initially placed on the thin actuating rod to achieve a relation between its bending deformation and the grasping force; however, there was too much coupling with the lateral bending of the grasper shaft. By placing the sensor on the grasper handle, the sensor was easily accessible for calibration, and was not coupled to lateral tip forces. It could also be pre-strained very accurately so that its range of strain corresponded precisely to the linear region of the grasping force sensor. In having a high degree of linearity, the measurements from the grasping force sensor could be modeled by a line of best fit. Due to the thick cross section of the handle, there was only a small strain on the sensor, and the linear range of the sensor encompassed the full 20 N load. The RMS accuracy error in this load range was 0.747 N, further decomposed into a 0.663 N error for 0–10 N and 0.830 N error for 10–20 N. Due to loose joints in the system, and to large bending of the thin actuating rod, there was significant hysteresis error between force application and relaxation in the results. Future designs will incorporate a more rigid actuating rod, and tighter tolerance components to minimize these effects.

4.4.3 Overall System Performance

Minimal processing was applied to the signal because the signal-to-noise ratio was already high with a 0.075 N noise error and a negligible drift error. Since fiber optic sensors are not prone to electrical noise, and the light noise was insignificant to the broadband power, all of the noise is assumed to be within the circuit board design. Furthermore, with additional circuit board design considerations, the ADC resolution potential could be increased by 2.63 times from the current resolution of approximately 0.01 mN. One source of noise that was difficult to eliminate with a low-cost design was noise that arises within fiber connections. Since quick-connect connectors were initially used instead of a fusion splicer, alignment issues were encountered between the sensing fibers, the splitter, the circulators, and the broadband power supply. The recorded sensitivity of the fibers is approximately 0.05 N, however this value could improve with reduced noise.

4.4.4 Auto Zero-Drift Compensation Method

Due to the low signal noise, and relatively high sensitivity in FBGs, a tested method to calibrate system drift has been formulated. The procedure is to auto-reset the reference zero value if the tool has been under zero load for approximately 3 seconds. With the maximum noise of the system calculated as 0.075 N, a zero load condition is met if the noise remains under 0.1 N for 3 seconds. Due to high tool sensitivity, it is conjectured that a surgeon will not be able to maintain a sub-0.1 N load fluctuation while in contact with tissue for greater than 3 seconds; however, further experimental testing is necessary to prove this claim. This method requires configuring the sensors to be within a linear range at all times. Further testing on this drift compensation method is recommended to prevent zeroing errors, and to fine tune the zero load period and acceptable load error.

4.5 Summary

This first-generation instrument was first calibrated and then tested in axial, bending, and grasping configurations that measured RMS error, repeatability, hysteresis, noise and drift. The first results for this system were gathered, and while some values are larger than the tool specifications, concrete methods to improve the tool and address these errors are presented. The axial force could not be measured accurately using the current design, and so a new design was undertaken to improve both the axial calibration jig and the axial sensitivity of the tool. Additional sources of error and areas of improvement in the other testing configurations of grasping and bending were identified for the tool. A method to address drift in real-time is described, and would increase the overall accuracy of the fiber sensors.

Chapter 5

Evaluation and Discussion – Second Generation Instrument

5.1 Introduction

Using insights and lessons learned from the first functional prototype discussed in Chapter 4, a second functional arthroscopic grasper prototype was designed and built (Figures 5.1a and 5.1b). This tool incorporates the axial element discussed in Chapter 3. Since the axial element affects bending as well as axial sensitivity, the tool was fully recalibrated for axial, bending and grasping with the new design to ensure that no functionality was lost. With the addition of the axial force measurement, the coupling of the bending and axial signals to the grasping signal was also analyzed and formulated into coupling calibration curves for each sensor. An interrogator from Micron Optics was purchased to compare the low-cost system with a commercially available system. Calibration and validation were assessed with each system.

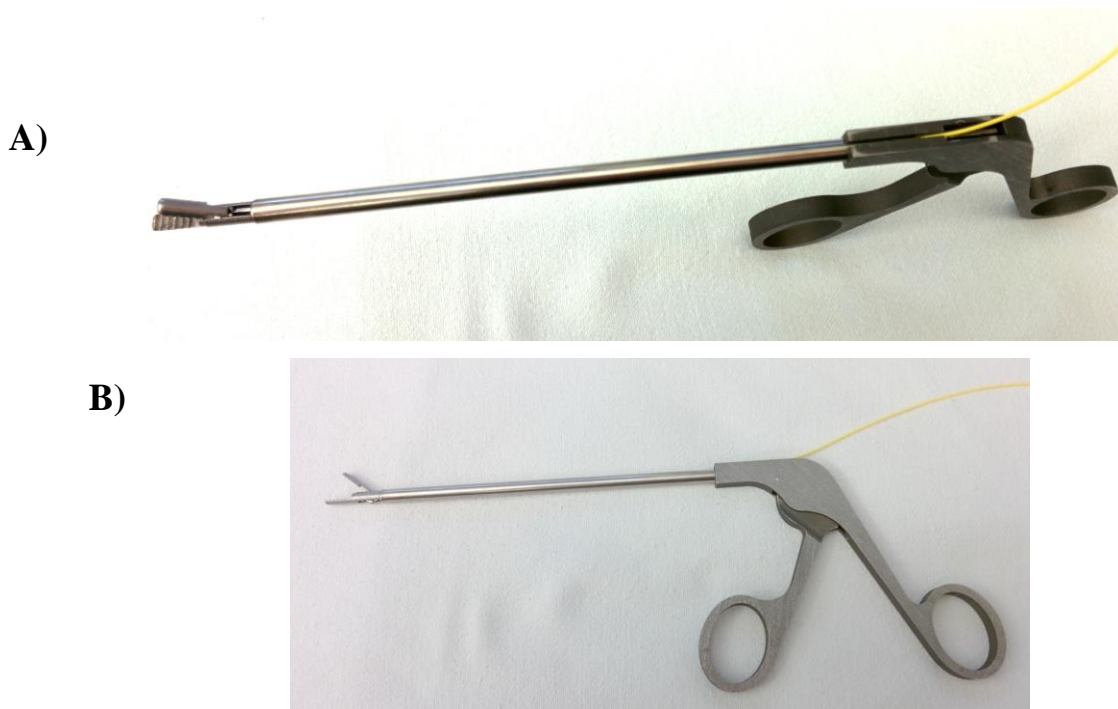


Figure 5.1: Second generation instrument with stress relief cable (a) top view; (b) side view.

5.2 Design Changes

Early in the testing of the axial element, it was realized that the sensor shaft press-fit could not withstand the 20 N axial forces being applied. For this reason, a stepped slot was added at the handle–shaft junction such that both the sensor shaft and outer shaft could independently be glued to the handle. This design was very stable throughout both 20 N compressive and 20 N tensile axial loading. To facilitate this design, the thin 1" section of the sensor shaft, which is used to configure the fibers for a single exit point, was shifted 1" distally (Figure 5.2).

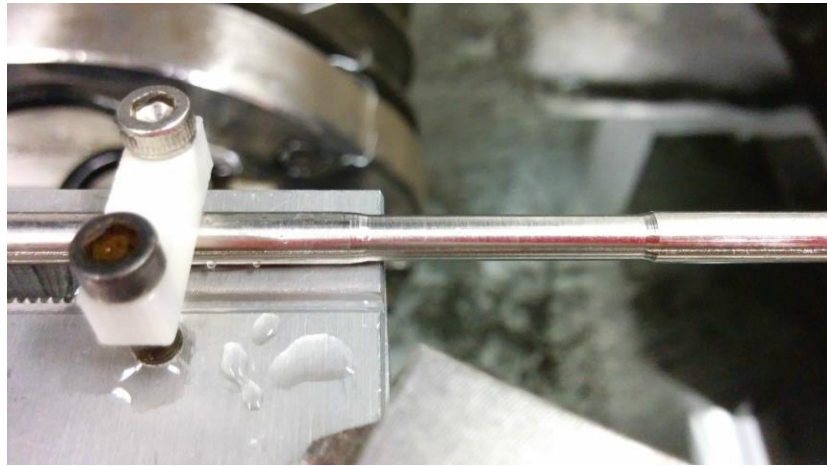


Figure 5.2: 1" thinned sensor guide cut.

Originally the fibers were glued across the axial element according to the hypothesis that compression was more reliable if the fiber was glued down. However, gluing across a discontinuous member caused alternating stresses across the fibers, resulting in increased breakage. To counteract this effect, an improved method of pre-straining the fiber was adopted. This involved hanging 200 grams from a pulley attached to each fiber (Figure 5.3) and gluing the fiber on either end of the axial element. 200 grams gave very consistent pre-strain to each of the FBGs (8 nm wavelength shift), resulting in reliable signals in compression. With the increased bending of the tool resulting from the new axial element, there was increased pressure between the sensor shaft and the outer shaft. This pressure was transferred to the fibers, causing them to strain at different rates and give off multiple wavelength peaks, and causing large light losses. This anomaly was only realized once the full wavelength spectrums were visualized on the Micron Optics interrogator. To compensate for this effect, the slots were cut 10 μm deeper, and less glue was used. As a result, there was still slight attenuation, but a single major peak could be distinguished among the readings.



Figure 5.3: FBG pre-straining apparatus.

After purchasing the Micron Optics interrogator, the exact bandwidth and wavelength shift of the FBGs could be seen. The Full-Width at Half Maximum (FWHM) of each FBG spectrum was 0.25 nm, which means that to stay within a linear measurement region, the full range of all 3 fibers including pre-strain (0.1 nm), drift (0.02 nm), noise (0.02 nm), and maximum strain (1.5 nm), would need to all be contained within 0.25 nm on the reference fiber. This was an unrealistic expectation, especially since 20 N axial deformation alone ended up straining the fibers by a full 1 nm. Therefore, instead of an FBG being used for referencing the 3 signals, a LPG fiber was purchased, which has a linear range of 10 nm. This increases the total cost of the system by \$100, but greatly improves the robustness and range of measurable forces. Figures 2.17b and 3.2a show the spectral relationship between FBG and LPG fibers. The main negative aspect of using the LPG fiber is that it produces a much smaller signal.

Once the Micron Optics Interrogator was available, there was a desire to test and compare the same tool and same sensors on both the Micron Optics and the Low-Cost systems. While the Micron Optics system is based on wavelength and the Low-Cost system is based on optical intensity, each is calibrated to output force as the comparable measurand. In order to significantly decrease the optical

losses in the system (increase the signal), and to allow for an easy transition of the sensors between the Micron Optic interrogator and the Low-Cost interrogator, FC/APC connectors were spliced onto the ends of the sensors to replace the previously used SC connectors. A fusion splicer (Fujikura, 40S) was used to make these connections (Figure 5.4). This allowed the instrument to be swapped between systems simply by unplugging the 4 sensors from one and plugging them into the other. The signal amplitude was increased so significantly that the amplification resistors across the transimpedance amplifier had to be reduced from 82 M Ω to 6 M Ω .

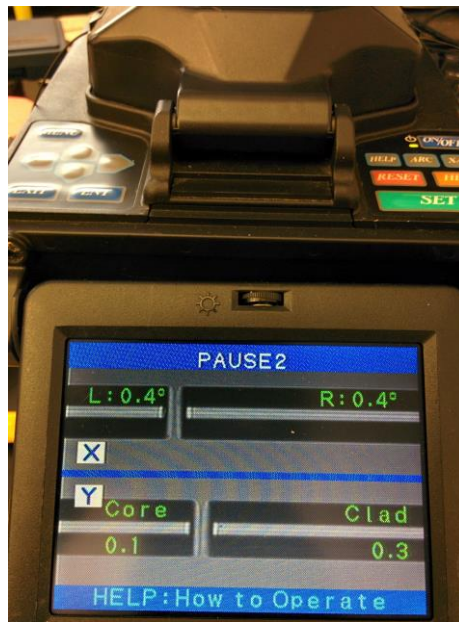


Figure 5.4: Fusion splicing apparatus.

To assist in comparing the two interrogation systems, the developed software was modified to read the FBG sensor wavelengths directly from the Micron Optics sm130. Due to limited control provided by the Micron Optics API, an asynchronous thread was programmed to continuously parse the buffer and return timed signals. While reprogramming the software, automatic calibration functions were implemented for bending, grasping, and axial force. The axial force measurement software was also fully redeveloped to simplify data recording.

5.3 Calibration Changes

5.3.1 Bending Calibration

In the calibration method for the previous tool, theoretical calculations were used to predict the resultant bending forces based on the output of the three fibers. During the calibration of the new

tool, these equations did not hold true. On observation of the signal output, it was apparent that the tool had a tendency for increased bending along certain axes. It is believed that this behavior is caused by the cut pattern of the axial element not being entirely uniform. The bending calibration equations were improved with a lookup table that used lowest energy splines and linear interpolation to predict the force and force angle applied to the tool. By using an increased amount of data, the tool is more fully characterized, which theoretically provides more reliable data.

The x and y tool forces were measured by hanging weights from the second tooth of the lower grasper jaw in a cantilever configuration. The applied weight ranged from 0 to 500 g in 100 g increments. The support point was located 1 cm from the shaft–handle connection, for a cantilever arm length of 13.25 cm. The tool was rotated manually in 60-degree intervals for a total of six positional measurements within a calibration jig. The signals from each of the three fiber sensors were recorded at each weight and position. The first series of complete data points was used to produce the calibration curves seen in Figures 5.5 and 5.6.

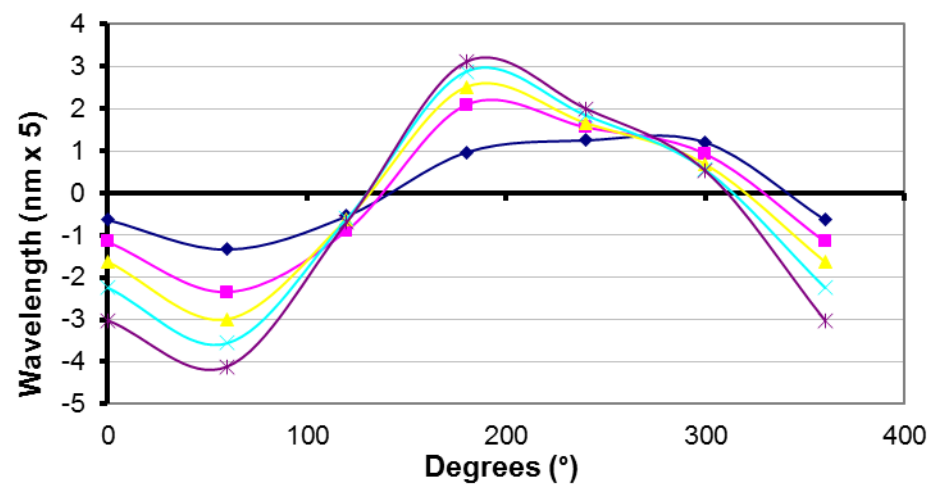
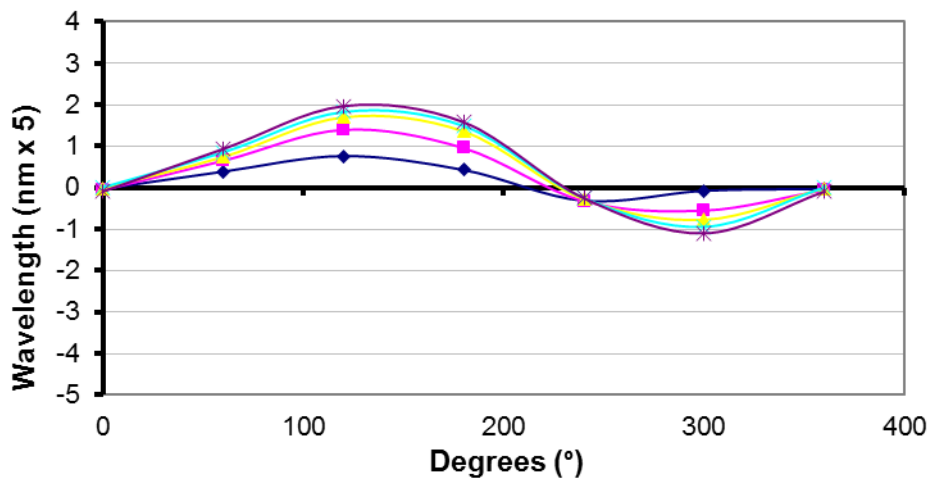
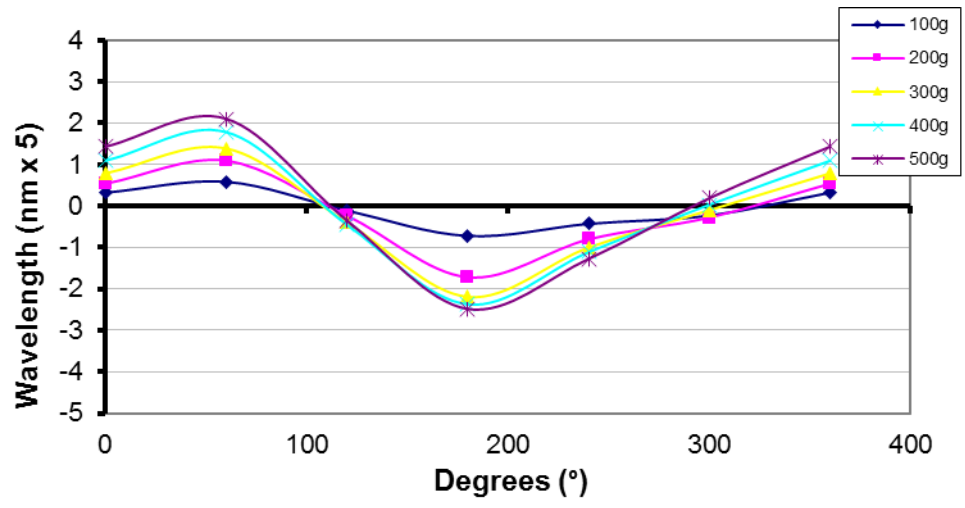


Figure 5.5: Micron Optics bending calibration curves (Sensors 1 – 3).

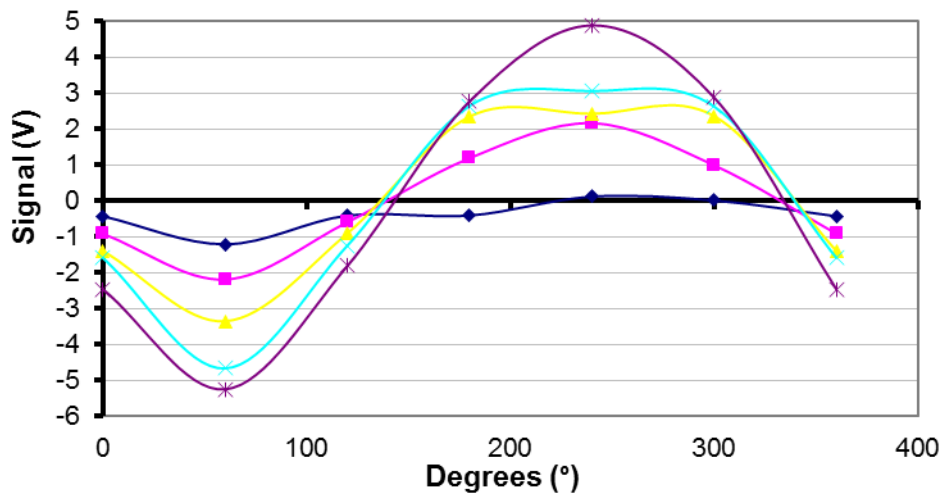
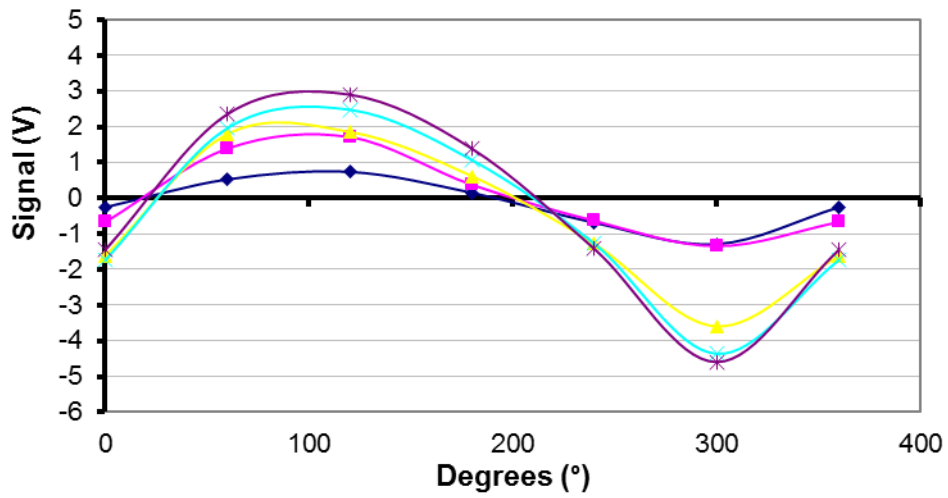
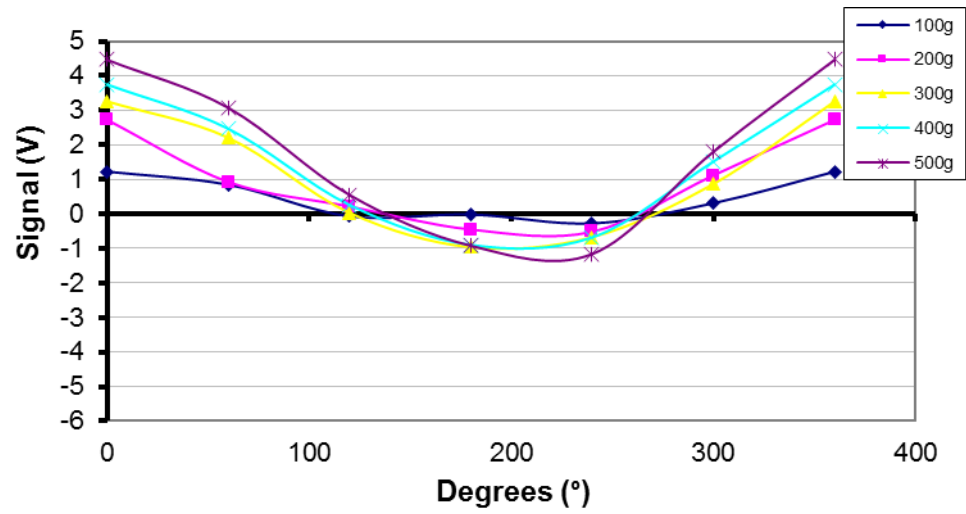


Figure 5.6: Low-Cost System bending calibration curves (Sensors 1 – 3).

5.3.2 Grasper Calibration

The actuation force was measured by applying force normally to the movable grasper handle from 0 to 10 N while two fixed mounts secured the rest of the tool. The grasper jaw tips were secured on a two-plate rapid-prototyped plastic jig with each plate fastened to either side of an ATI Nano 43 force/torque sensor (Figure 4.4). The first test was used to produce the calibration curves seen in Figure 5.7a and 5.7b.

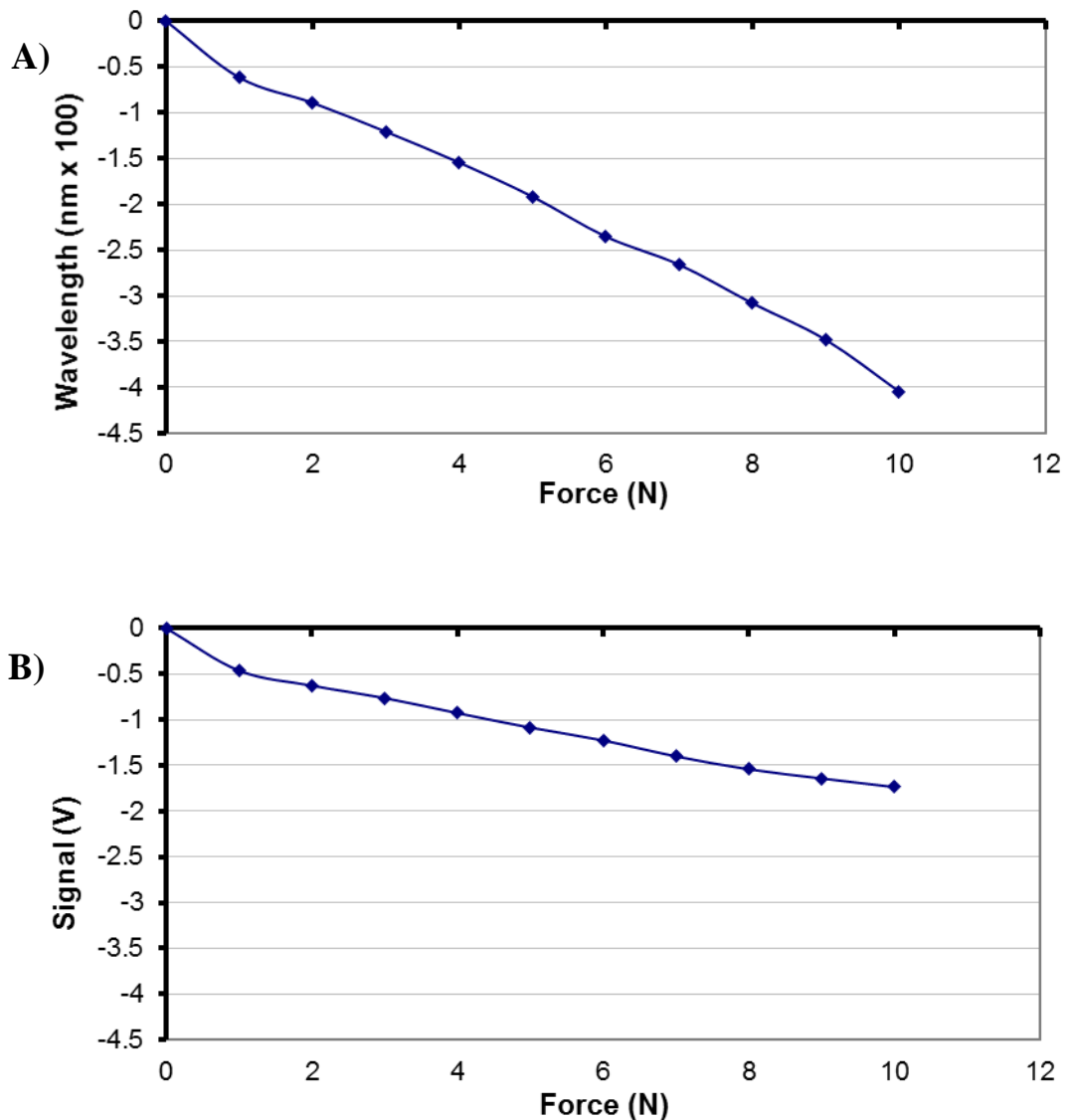


Figure 5.7: Grasper calibration curve (a) Micron Optics; (b) Low-Cost System.

5.3.3 Axial Calibration

The axial calibration was performed with a slightly different apparatus design than was used for the first-generation prototype instrument (Figures 5.8a and 5.8b). Instead of fixing the jaws in a rigid plastic extrusion at a position with presumed zero bending on the tool shaft, three set-screws were instead used at 120 degree angles to fix the jaws and allow fine tuning in all directions. By using the Micron Optics interrogator, the spectrums of all three fibers could be precisely aligned to guarantee minimal bending of the tool shaft. This design was very robust, easy to use, and improved the results significantly.

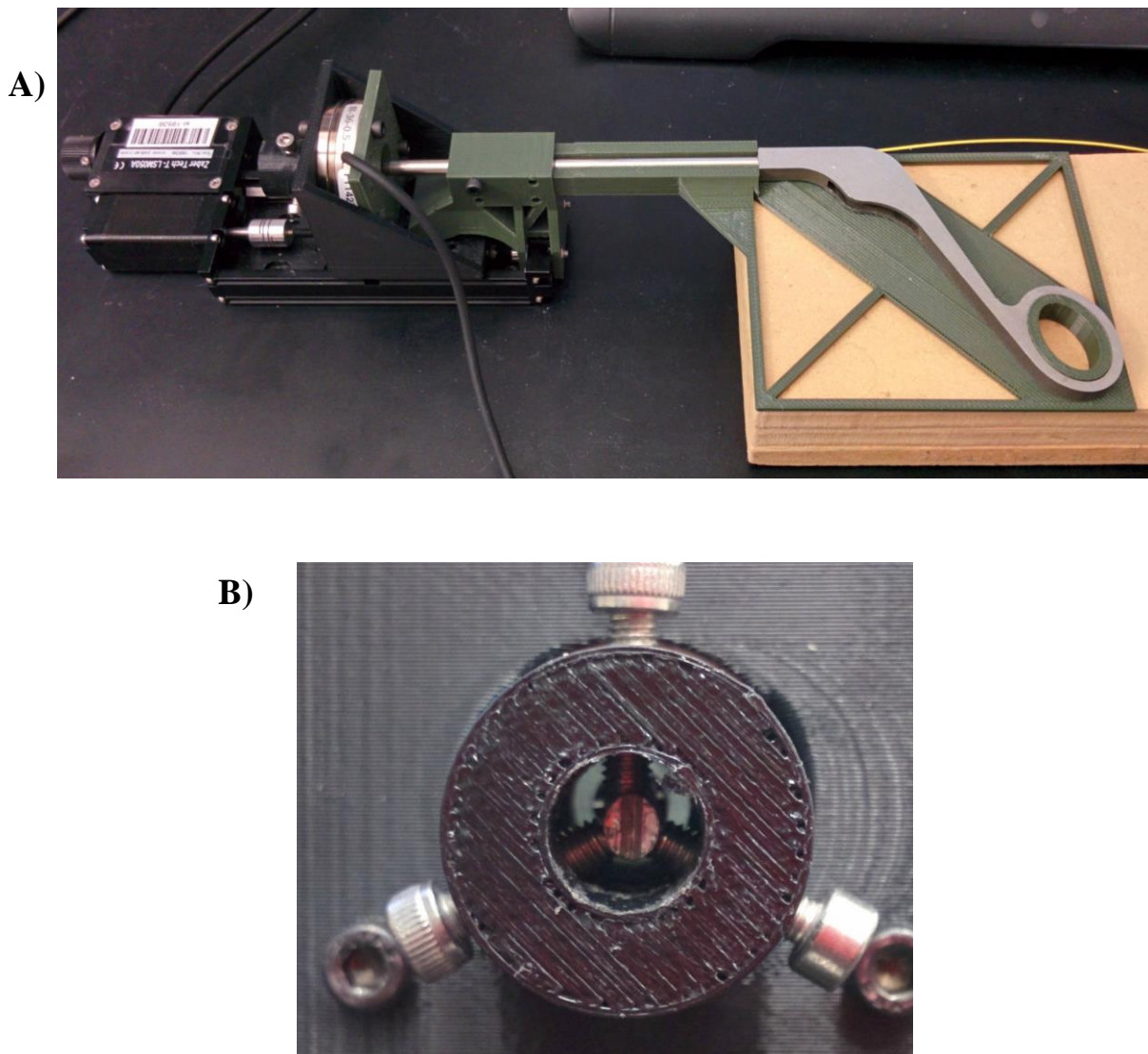


Figure 5.8: Axial strain calibration apparatus (a) full view; (b) three point set screw alignment.

The axial force was measured by stabilizing the tool and tuning the set screws until the shaft was in a near-zero bending configuration. A zero-bending condition was determined by viewing the reaction of the signals to low axial force, and maximizing the sensitivity of all the signals in both tensile and compressive directions. Figure 5.9 shows the maximized tensile peak followed by the minimized compressive valley. One side of the ATI Nano 43 force/torque sensor was connected to a Zaber Tech T-LSM050A linear stage, while the other side was connected to the tool. The linear stage was manually moved to increase or decrease the axial force on the instrument between 0 and 20 N in both compression and tension. The first test was used to produce the calibration curves seen in Figure 5.10.

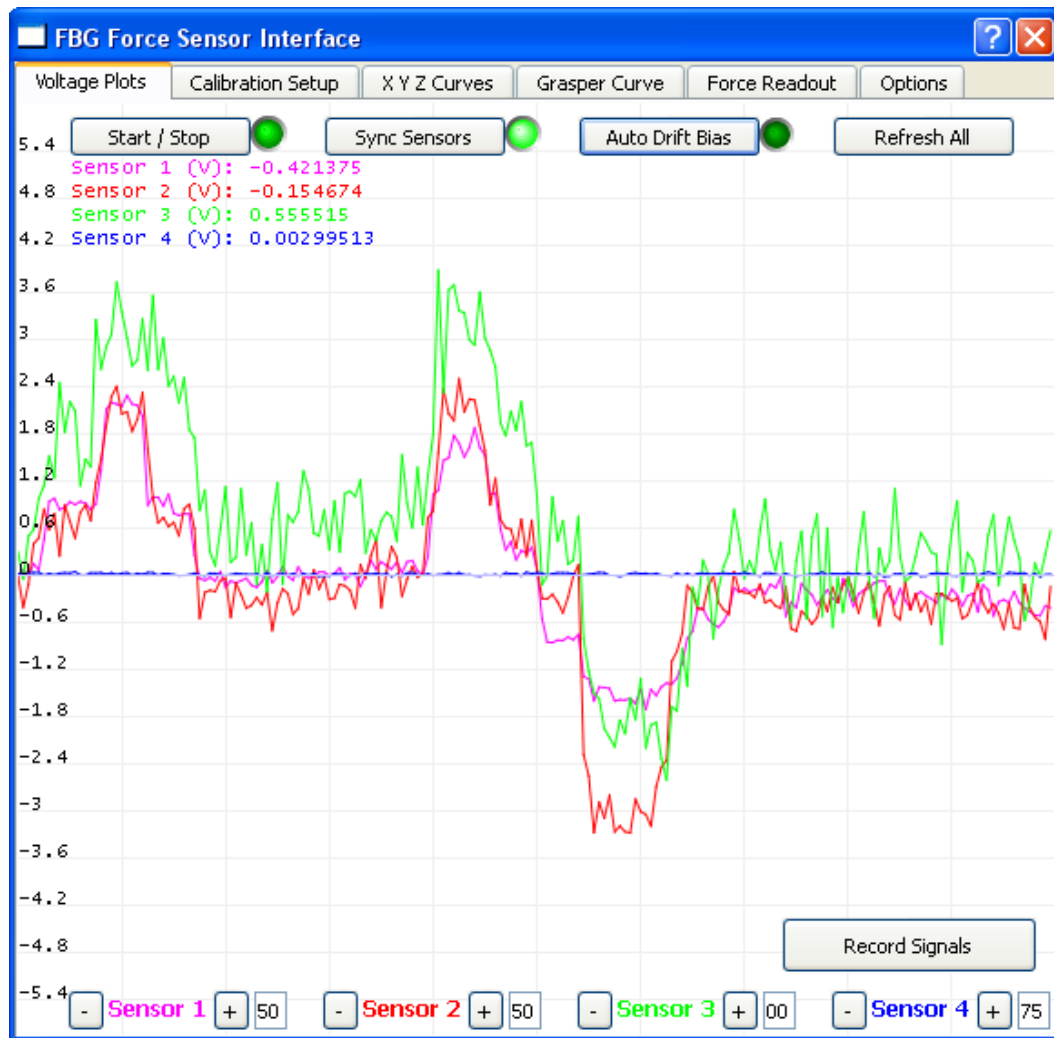


Figure 5.9: Low-Cost System axial tuning (positive = tension).

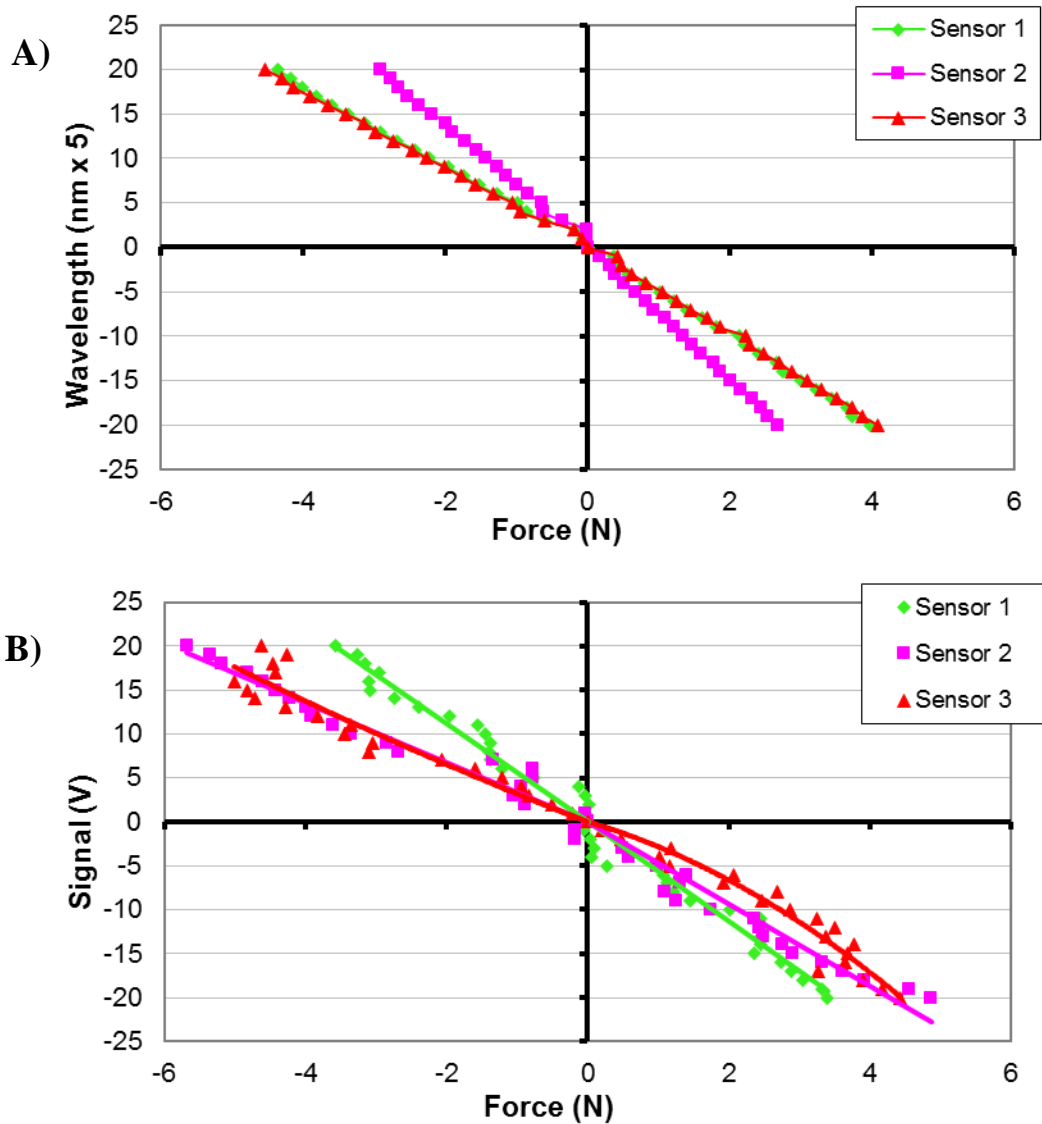


Figure 5.10: Axial calibration curve (a) Micron Optics; (b) Low-Cost System.

5.3.4 Signal Coupling

When grasping force is applied through the actuating rod, the shaft of the instrument is put into axial tension due to the construction of the tool. Theoretically, if the axial-grasping calibration curve is known, when the grasping force is known, the axial corresponding axial force can be calculated and biased accordingly. If there is no force on the moving handle by the surgeon, the applied axial force will not increase the grasping force reading since the rotation of the moving grasper handle is unrestricted. During the tests for grasping using the 4th sensor, the signal from the 3 shaft sensors

was measured to determine corresponding axial and bending coupling responses. The first test was used to produce the calibration curves seen in Figures 5.11 and 5.12.

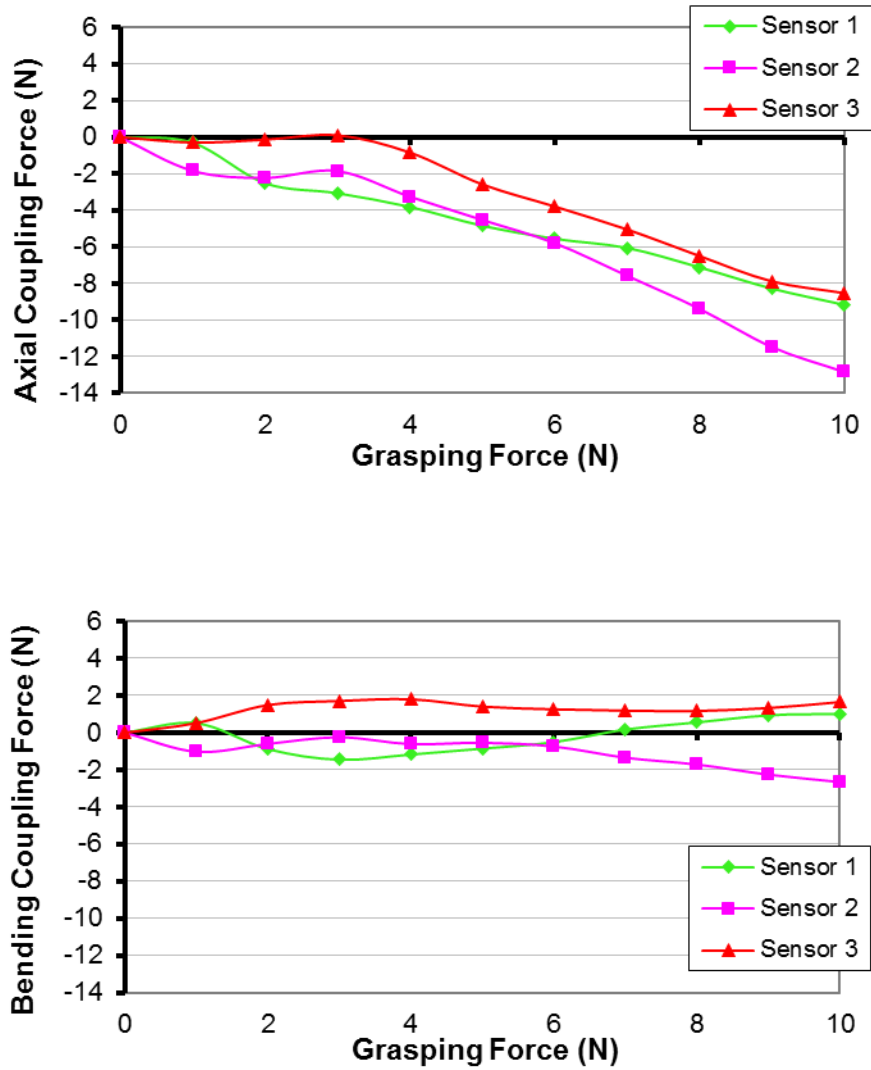


Figure 5.11: Micron Optics coupling curves.

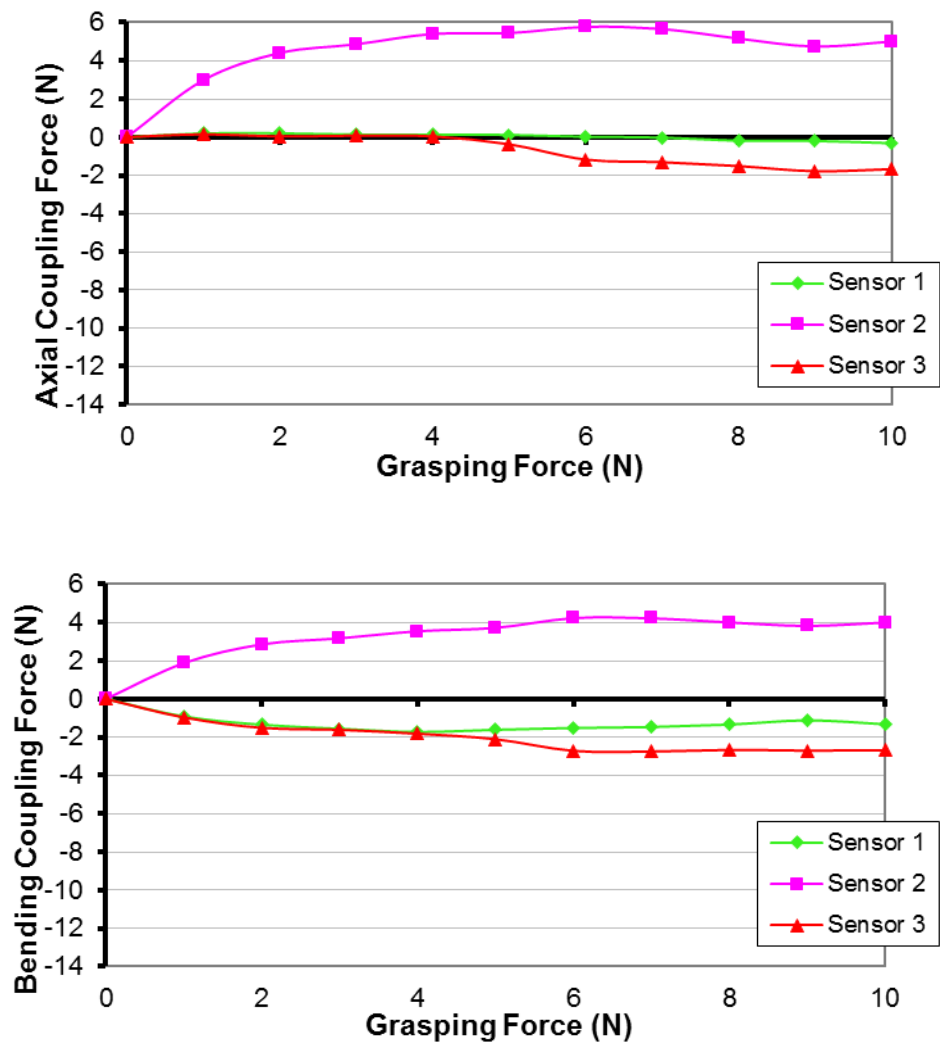


Figure 5.12: Low-Cost System coupling curves.

5.3.5 Noise and Drift

The system noise was recorded over a time of 30 seconds for each system (Micron Optics and the Low-Cost System). 800 readings were analyzed and the maximum and minimum signal values were recorded to give a noise range (Figures 5.13 and 5.14). There was a minimal amount of outliers that were filtered out of these results. These signals were then converted into force using the corresponding axial calibration curves. The system drift was determined by recording the average signal value before and after a 10 minute interval and taking the difference.

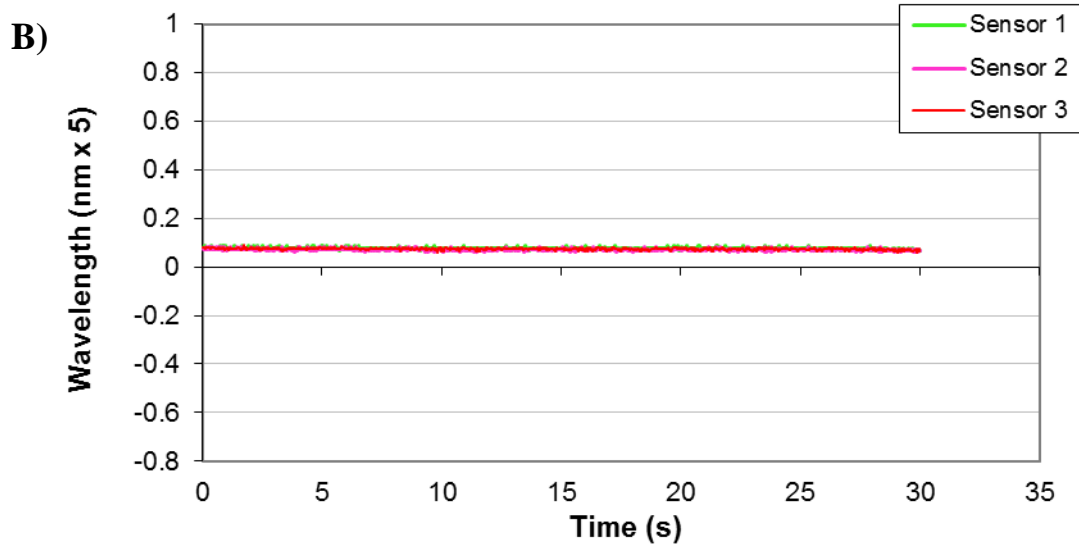
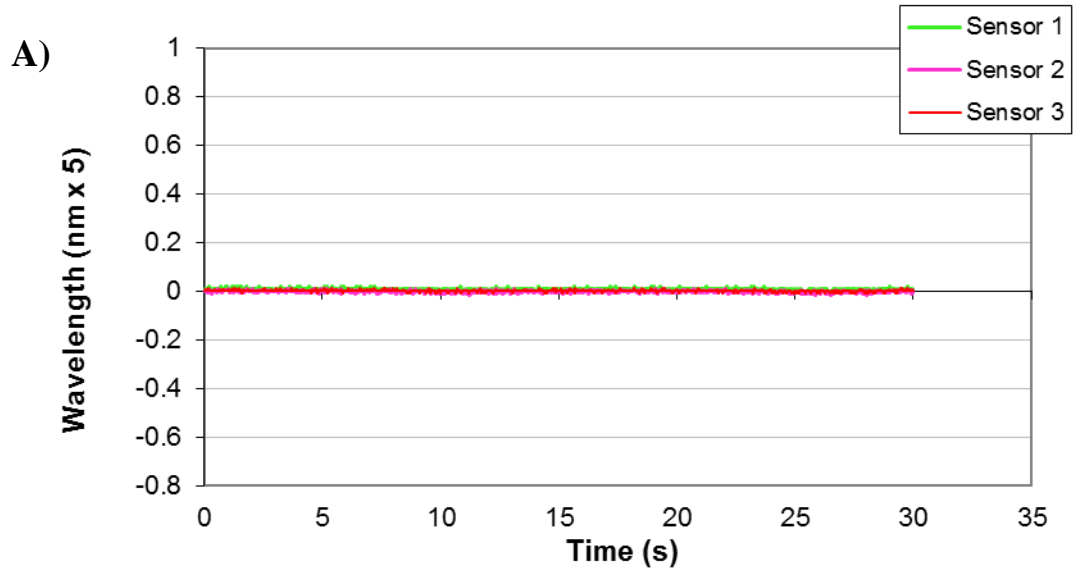


Figure 5.13: Micron Optics noise and drift data (after 10 minute interval)
 (a) initial noise; (b) 10 min drift.

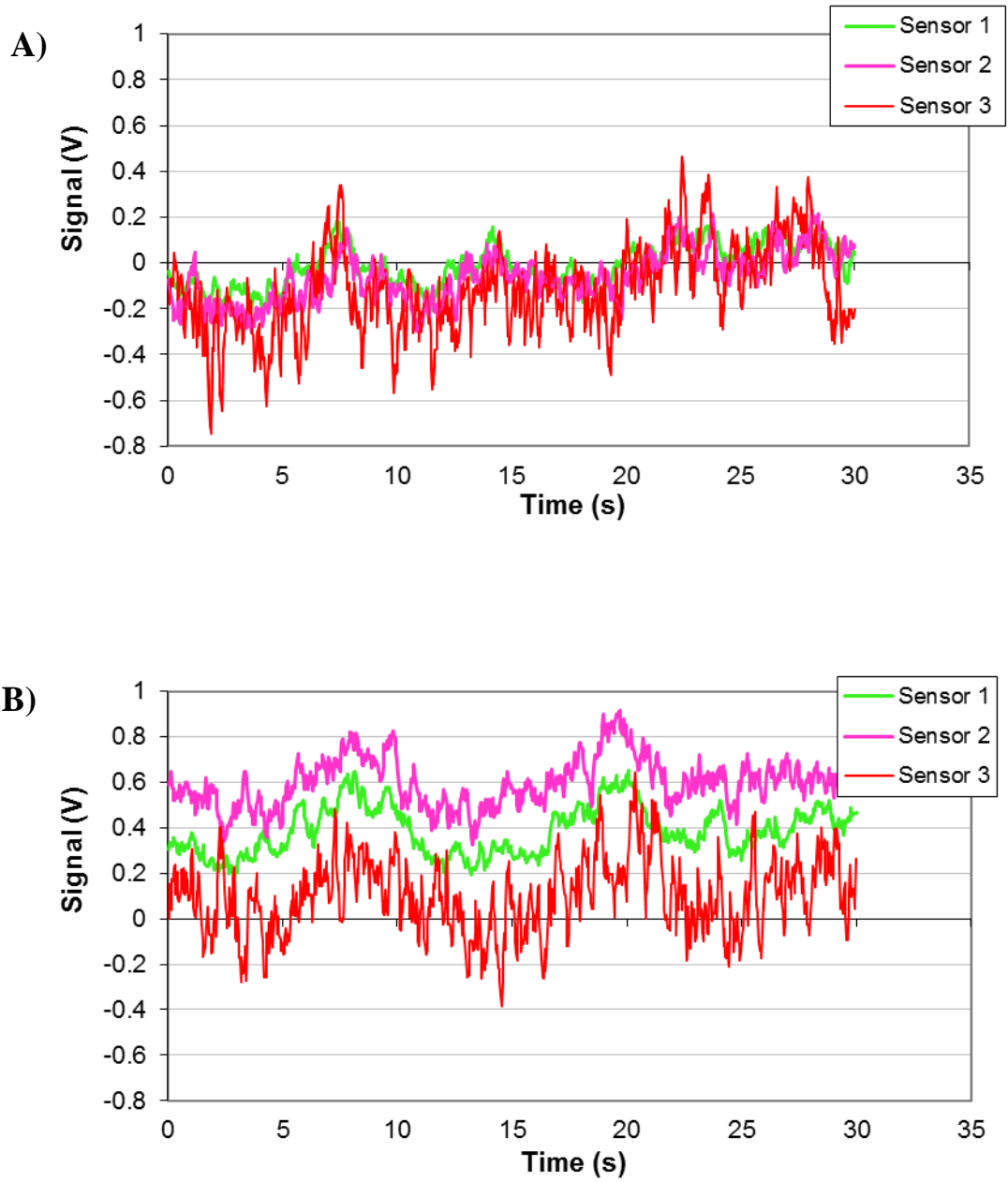


Figure 5.14 Low-Cost System noise and drift data (after 10 minute interval)
 (a) initial noise; (b) 10 min drift

5.4 Performance Assessment

The performance of the second-generation prototype was assessed by running multiple trials with both the Micron Optics and the Low-Cost interrogators. The same apparatuses used for bending, axial, and grasping calibration were used. The performance of the FBG sensors was assessed based on the following measurements, summarized in Tables 5.1 and 5.2. The results are a combination of errors within both the instrument and the corresponding interrogation system.

i) Accuracy: The RMS bending error of the shaft sensors was determined by hanging weights from 0 to 500 g in 100 g increments in each of the 6 angles for 5 additional trials. The weights were fully removed before rotating the instrument. The RMS error of the axial force was evaluated by applying increasing and decreasing forces to the grasper tip over the range of -20 to 20 N in 1 N increments for 11 additional trials. The RMS error of the grasping force was determined by applying increasing and decreasing forces to the handle over the range of 0 to 10 N in 1 N increments for 9 additional trials. From measuring the shaft sensors during the grasping trials, the coupling equation was formulated. The RMS error of the coupling force was thus evaluated over the same 9 trials.

ii) Repeatability: The maximum standard deviation (σ) was evaluated for bending, axial, grasping, and coupling forces using the same tests described above for accuracy.

iii) Hysteresis: The RMS error was calculated between the increasing and decreasing load values of both the sensor shaft and the grasping sensor using the same data obtained from the accuracy assessment.

iv) Signal Drift and Noise: The drift of the sensor signals was evaluated after 10 minutes under a zero loading condition. The maximum signal noise was evaluated for 30 seconds for each fiber under 0 N, 3 N, and 5 N steady loading conditions. A 10 minute drift time was chosen to simulate the maximum continuous time in contact with the tissue during arthroscopic surgery.

v) Sensitivity: The minimum sensitivity of the sensors in their linear range was tested by applying force to the grasper tip and grasper handle until the signal was visually discernable from the noise on the user interface.

vi) Resolution: For the Micron Optics system, the maximum resolution is approximately 1 pm (500 Hz), which correlates to a force of 4.3 mN using the average strain responsivity of all 4 fibers given by the axial and grasping calibration curves. For the Low-Cost System, the maximum effective

resolution is limited by the circuitry, software, and serial communication with the ADC. Electrical noise, inefficient coding, and slow serial communication limited the ADC capabilities. The ADC resolution would ideally be distributed over a ± 5 N load range and would be approximately 10 mN (10 Hz).

Table 5.1: Micron Optics calibration assessment.

	RMS error	Max σ	Hysteresis	Noise / Drift
Bending (N)	0.6393	0.2722	0.3812	0.0585 / 0.4066
Force Angle ($^\circ$)	9.363	5.472	9.954	—
Actuation (N)	0.3716	0.3530	3.8229	0.0585 / 0.4066
Axial Force (N)	0.9643	0.8302	8.5813	0.0585 / 0.4066
Coupling (N)	—	0.5895	—	—

Table 5.2: Low-cost system calibration assessment.

	RMS error	Max σ	Hysteresis	Noise / Drift
Bending (N)	0.6861	0.5924	0.9065	0.9477 / 1.9838
Force Angle ($^\circ$)	15.993	14.822	14.994	—
Actuation (N)	1.5034	1.4586	3.5315	0.9477 / 1.9838
Axial Force (N)	1.9472	1.3208	5.9778	0.9477 / 1.9838
Coupling (N)	—	0.6824	—	—

5.5 Validation of Force Calibration

The primary change in the second-generation tool was the addition of the axial element. Due to the increased axial sensitivity caused by this element, bending and axial forces were difficult to isolate during calibration. The added instrument flexibility is hypothesized to be the main contributor of the increased bending and grasping errors, as compared to the first-generation design. In order to compare the Low-Cost system to the commercially-available Micron Optics system, the arthroscopic tool was evaluated using both systems with identical calibration methods. The following validation will discuss the benefits and drawbacks of each system, and will compare the overall performance of each.

5.5.1 Bending Forces

The measurements taken from the three fibers at each of the 60° increments were tabulated and equated based on their corresponding locations to give a maximum resultant force and an angle of

force application. A variety of factors can explain the RMS errors of 0.213 N, 0.6393 N, and 0.6861 N, for the 1st generation tool and Low-Cost System (1G-LC), 2nd generation tool and Micron Optics System (2G-MO), and the 2nd generation tool and Low-Cost System (2G-LC), respectively. The most prominent is the addition of the axial element adding additional degrees of movement to the tool. In the bending calibration curves, there is a tendency for increased bending in the 60 degree direction. This caused divergence from the theoretical calculations used for the 1G tool and required a new calibration technique to be adopted. This specific observation helps explain the larger errors in the predicted angle of force application. The new technique characterized the bending of the tool more fully, 33 vs. 90 points; however, it did not fully reduce the error caused by the increased movement.

As the new calibration process was developed, there was one key challenge. When a fiber that is positioned at the current neutral axis (NA) changes from compression to tension, the signal output remains the same, irrespective of weight; therefore, this signal can not be used in force estimation. Theoretically, these NA points for different fibers should be offset by 60 degrees, allowing the other two fibers to successfully predict a force. At approximately 250 degrees, however, all three fibers are close to convergence, causing larger errors. This error could be improved with further analysis of the axial element cut design, by adding a fourth fiber for redundancy, or by plotting more data points at this angle.

While the RMS error was similar between the LC and MO systems, by looking at the maximum standard deviation (Max σ) and hysteresis errors, it can be seen that the MO system is much more precise: 0.2722 vs. 0.5924 and 0.3812 vs. 0.9065, respectively. This is primarily due to reduced noise for the MO system, by a factor of 16. As the RMS error is much larger than the Max σ for the MO system, a better selection of calibration curve is likely to improve the results significantly. Further improvements in axial cut patterns, fiber placement, angle measurement, and weight application will help to reduce errors further and reduce dissimilarities between fibers. The calibration curve was also made with a least-energy spline method to join the discontinuous sample points: additional points for this curve could give more accurate results.

Addressing the Bending Validation in Section 4.4.1, it is important to note that the increased noise in the 2G-LC system vs. the 1G-LC system and the increased errors in each section are a result of an LPG reference fiber compared to the previously used FBG fiber. This ensures the monotonicity of

the calibration curves over, at minimum, the full loading range (20 N), as opposed to the curves for the first-generation system that had a uniqueness range of only 5 N. The broader spectrum, however, decreases the signal to noise ratio, resulting in increased noise. The noise and drift values are independent of loading condition as the fluctuations are located primarily in the system, not at the instrument level, and are electrical rather than optically based. Originally it was conjectured that a stiffer tool with FBG sensors could broaden the range of the sensors; however, once the signals were viewed on the Micron Optics Interrogator, it could be seen that a stiffer tool would not be effective enough. The broader spectrum also puts less emphasis on perfect pre-straining, significantly reducing the challenges of fiber adhesion.

5.5.2 Grasping Forces

The grasping force was not significantly affected by the new axial element or other changes in the new instrument, and thus maintains similar sources of error for RMS and hysteresis as in Section 4.4.2. The RMS errors of 0.747 N (1G-LC), 0.3716 N (2G-MO), and 1.5034 N (2G-LC) correspond closely to the noise values in each respective system, as explained in Section 5.3.5.

5.5.3 Axial Forces

The axial force element in the second-generation instrument significantly amplified the axial deformation of the sensor shaft, allowing measurement of axial force. The RMS errors of the 2G-MO and the 2G-LC systems are 0.9643 N and 1.9472 N, respectively. The Micron Optics system has a much lower noise level, and thus provides a more accurate representation of the possibilities of axial measurement. The RMS and Max σ errors, both being just under 1 N, can be caused by excess movement in the axial testing apparatus, different speeds of loading and unloading, drift over the 80 seconds of loading during each test, and unequal axial deformation or twisting within the axial element cuts. The largest trend errors visible in the test readings were during 15 and 20 N of compression, measured by the ATI F/T sensor, where the deformation of the axial element began to level off. For the tested instrument, the axial element was set at 1 cm from an initial 2 cm length in order to decrease excess bending while still providing sufficient axial deformation to allow measurement of axial forces. This change may have decreased the possible axial deformation of the element at large compressive loads. Sensor 3 was modeled by a second-order polynomial in order to address this effect while maintaining uniqueness in the plot, although the effect could not be completely controlled. Another possible cause of this error could be contact between the sensor shaft

and the outer shaft. The outer shaft is intended to be floating in the axial direction, as the design includes approximately 1 mm of axial clearance. If the tool was compressed by more than 1 mm during large compressive loading, the forces would level off as well. The large hysteresis errors for axial measurement, 8.5813 N (2G-MO) and 5.9778 N (2G-LC) may be caused by the time delay for the elastic deformation in the axial element to return to normal. This effect gives significance to the fact that the large loading time of 80 seconds may increase the RMS error of the system depending on different loading rates. While this loading time was kept constant throughout testing, additional experimentation can be done using different periods. Further, these different time periods could be related to loading times in real surgeries.

As this is the first time axial force has been measured on this arthroscopic instrument, there are a variety of improvements that can be made in future generations of the tool. The concept of measuring axial deformation while maintaining bending and grasping has been proven possible. The radial cuts in the sensor shaft were a simple and effective method to achieve this goal while keeping the size factor of the tool at a minimum.

5.5.4 Coupling Offsets

The coupling offsets caused by grasping were validated by the Max σ between the results. The RMS accuracy error could not be measured as there was no calibration apparatus available to accurately apply both an axial and grasping force simultaneously. Designing such an apparatus would give better measurements of the coupling accuracy. The coupling deviation values of 0.5895 N and 0.6824 N for the 2G-MO and 2G-LC systems are directly dependent on the errors among the other loading methods, and as such are in the same range. Improving the actuation, bending or axial force errors would further improve the coupling errors.

Initially, grasping was hypothesized to contribute almost completely to axial loading alone. When the bending curves showed increased tendency for bending at specific angles, however, the coupling offsets were broken down into both an axial and bending component. When the coupling offsets were measured as a direct summation between axial and bending forces though, after subtracting the axial force from the coupling offsets, in some cases the resultant bending forces did not fall into a bending state predicted by the bending calibration curves. This occurred more in the Low-Cost system than the Micron Optics System. The main reason for this fault is concluded to be as a result

of the noise in the system skewing the bending signal at low loading conditions. This effect can be seen in the flat bending calibration curves for 100 gram loading in the LC system (Figure 5.6).

5.6 Summary

The primary change in the second-generation instrument was the addition of an axial element to increase the axial sensitivity of the tool. This necessitated a new fiber adhesion method using weights to pre-strain the fibers. With the ability to measure axial force, a coupling measurement was also made between grasping and axial forces for greater accuracy of the system. Changes were also made in the calibration equations, specifically in bending, to give more accurate results. With the availability of a Micron Optics interrogator at this point in the project, the performance of the instrument was assessed both with the low-cost system described herein, and with the Micron Optics system. Sources of error and areas of improvement are also discussed for future instrument development. Appendix V provides a complete calculation example using the calibration graphs and coupling biasing.

Chapter 6

Conclusions and Future Work

6.1 Introduction

The work presented in this thesis describes the process behind developing a fiber optic force sensing system and arthroscopic tool set. A review of the current state-of-the-art shows the absence of a commercially available 4-DOF force-sensing arthroscopic grasper, and a 3-DOF force sensing arthroscopic probe and shaver. The arthroscopic grasper was evaluated both with the Low-Cost (LC) System and the Micron Optics (MO) Interrogation System in order to formulate a comparison between the two units.

The small-scale size and high-resolution response needed in the arthroscopic tools encouraged development of a separate fiber optic sensing system using fiber Bragg gratings. By adding slots in an inner sensor shaft, these fibers could be used as strain sensors to measure the applied forces on the soft tissues and bones inside the patient's body. Common in long-shaft surgical tools is the difficulty of measuring axial forces. For this purpose, additional axial sensing elements were developed to increase axial sensitivity. The most significant amount of work was done in developing the fiber optic system as a low cost option (\$4,500 CAD vs. \$25,000 CAD) for laboratory research. Through thorough research into the development of low-cost all fiber systems, a final solution was created, complete with software and electrical signal processing. Calibration and testing experiments performed with the instruments showed their effectiveness and performance in force measurement. This proves their usefulness in a preliminary training environment for surgeons. The sensorized tool presented herein is a tested solution for measuring forces in a surgical training environment; however further improvements can be made in future development.

6.2 Contributions

The work presented in this thesis will benefit the engineering and medical communities by describing the development of an arthroscopic instrument and force sensing system capable of measuring small-scale MIS tissue interaction forces. Specific contributions of this work include the following:

- The fiber Bragg grating system that was developed at a low-cost provides a reasonable solution to investigate the use of FBGs as sensors in future medical tool devices. Before the development of low-cost sensing systems, the expensive interrogation of the sensors was the largest roadblock. By using a simple ratiometric photodiode setup with corresponding transimpedance amplifiers and a low-noise ADC converter, the low forces that can be sensed by this tool are effective for the scale of arthroscopic surgery.
- The calibration and experimentation using this set of force sensing instruments (grasper, shaver, probe) illustrates the high resolution and high signal-to-noise ratio that is possible from the use of fiber optic sensors. The complete description of the design and manufacture of these tools shows the ease of fiber sensor adhesion compared to the complex alignment of common strain gauges. All of the new instruments were also designed to maintain the same small arthroscopic form factor.
 - The grasper incorporates fiber slots on an inner sheath to guide fiber optic sensors down the shaft. This design allows the instrument to sense forces on the tool tip without increasing the overall size of the tool. An axial element that was designed by cutting a notched pattern in the inner shaft allows forces to be sensed axially. The 3D sintering machine in Robarts was used to manufacture the grasper jaws, showing the possibilities of the technology. The three-fiber setup on the shaft in combination with the axial element allows forces to be sensed in 3 dimensions at the tool tip.
 - The shaver and the probe also incorporate fiber slots along inner sheaths to prove the tools with force-sensing capabilities. The probe, as with the grasper, was designed with a “floating” outer sheath, to allow slight compression axially so as to measure axial compression while maintaining rigidity of the instrument.

6.3 Recommendations and Future Work

Throughout the development of these tools and corresponding sensing system, areas of improvement and points of consideration were identified that can increase the overall performance of the MIS system. These areas of future work are presented below:

- The low-cost FBG interrogation unit, while currently only being used with the developed arthroscopic tools, can in fact be set-up with any FBG sensor system to sense strain. As the high cost of FBG interrogation is the primary limiting factor to the adoption of fiber optic

sensing technology, this low-cost system is an excellent solution for increasing the accessibility of these sensors in research. Other than strain, FBGs can also be used to sense displacement, pressure, acceleration and temperature, making this system increasingly versatile.

- Near the conclusion of this thesis, a fusion splicer was used in lieu of SC-SC mating connectors. This greatly reduced alignment and air-space losses, improving the signal. Similarly, professional polishing of the cleaved fiber ends may also improve the signal. An improved signal makes it easier to filter out any noise that is affecting the accuracy of the measurements. Another major recommendation would be to further research the effects of fiber twisting and bending on optical losses. The optical signal through the fibers making up the circulator largely decreased under a bending ratio of less than 2 cm, while the sensor fibers could bend down to 0.5 cm while retaining full signal. This could be caused by a difference in the fiber manufacturing process. When twisting the tool, the twisting of the fibers sometimes also led to signal losses. There was minimal study done on the effect that ambient light and temperature fluctuations have on the system, however better knowledge of this may also further reduce system noise. As the system runs on a wavelength of approximately 1550 nm, the effect of ambient light is assumed to be minimal. The temperature effects should first be tested by putting the tool in a 37 °C environment to simulate surgery. This could be done using a water bath, as the fiber optics are not affected by water. By attaching the grasping force fiber to the tool handle, the surgeon's hands may also heat the instrument. By exposing the entire tool to different controlled temperatures, the relationship between signal and temperature could be determined. To deal with excessive temperature effects, a reference unstrained fiber could be designed into the tool, the location of the grasping fiber could be altered, or the tool signals could be zeroed after entering the body.
- Since the success of implementing the sensing method and design have been demonstrated in an arthroscopic grasper, manufacturing equivalent sensing medical tools such as shavers, probes, punches, angled tool tips, catheters, arthroscopes and various other tools is a logical next step. As the addition of axial force sensitivity using a slotted axial element is a fairly recent development, further research can investigate alternative methods for increasing and decoupling actuation and bending signals. While torque sensing (tissue twisting) was not implemented on the tool presented herein, testing in real surgeries will decide if the ability to measure this force component would improve surgical procedures.

- While the tools have not been exposed to the chemicals and temperatures used in standard cleaning and sterilization procedures, the fibers themselves are chemically-inert and high-temperature-resistant. Biocompatible and autoclavable medical-grade adhesives are available and could be adopted for future versions of the instruments.
- The medical grade finish of the tool is possible using a combination of sanding, grinding, and glass bead blasting.
- The precision of the micromachine degrades significantly with the simultaneous use of multiple axes. The finish and precision given by the EDM machine is so superior to conventional milling that tool designs should initially design for machinability on the EDM.
- The 3D sinter technology in Robarts is an excellent resource for complex parts. This was used to manufacture the grasper jaws. The current rough finish of the technology can be improved using small diamond files and glass bead blasting. Currently, an electropolisher is being purchased for this machine to further improve the finish of the printed parts, reducing post processing significantly.
- The low-cost design objective was placed more on the FBG interrogation unit than the tool, since the cost of commercial interrogation units is significantly higher than the cost of manufacturing sensorized instruments. If the entire system is to become commercially available, different machining processes may be necessary to replace EDM machining of the tool with another process such as casting. Another point to consider in commercialization is which components on the tool should be single-use. For instance, if the blades on the newly developed shaver dull, then they should be made disposable. Currently the grasper can be disassembled such that the fiber sensor shaft can be separately removed. The fibers can then be removed from the shaft using acetone. In this way, the sensors can be kept while the remaining tool is disposed of. There will eventually be a choice between the cost to disassemble, sterilize, and reassemble the tool, and the cost to completely dispose of the tool.
- The most complex part of manually assembling the tool is in accurately pre-straining the fiber sensors during adhesion. The fibers should be pre-strained equally so that the sensing range falls in the linear region of the reference grating's spectrum. An improved method to simplify this adhesion process would significantly reduce manufacturing time and improve performance.

- To improve the robustness of the fiber connections, a mechanical connection can be used such as a “Quick Connect SC Connector”.
- Optimal tolerancing between the sensor shaft and the outer shaft on the grasper should be investigated in future tool generations to balance the axial restriction of the sensor shaft, while still having both tubes bend as one for easier calibration.
- Different angles of fiber adhesion around the shaft and different numbers of fibers to provide sensor redundancy for error reduction (varying from 3 fibers equally spaced at 120°) can be experimented with to show whether different combinations can improve instrument performance.
- The way in which the information will be displayed to the surgeon, whether as a constant data stream, or by a colored force indicator, should be examined in the future for effective visual communication.
- The calibration procedure for the bending force of the tools currently consists of manually hanging incremental weights from the tip of the grasper and recording the signal. It has been suggested that an automatic calibration system with motors and linear stages may be preferable to gain more accurate results through finer increments, and to also decrease the time needed for the process. Another improvement for the bending force apparatus would be to make the rotating gear more secure, and to add graduations along the gear for more accurate angle measurement. Also, the gear cannot rotate fully 360 degrees, necessitating removal of the tool for certain angles. The procedure to measure the grasping force relies on the transfer of force on an offset plastic attachment to the ATI force/torque sensor. Development of an improved method for accurately measuring grasping force would improve accuracy of the calibration. Axial calibration is the most difficult, as bending is difficult to eliminate in any setup. The current plastic jig can be further improved to limit this coupling as much as possible.
- A main recommendation for the calibration of this system, particularly in the area of grasping but also possible for all loading methods, is to develop an adaptive control system to measure the effects of loading time on the signal outputs. With the large hysteresis errors in the accuracy results due to the time dependent nature of stress-relaxation, it is certain that adaptive control would significantly improve the results. Figures 6.1a and 6.1b show individual cases of 5 N applied grasping force over 1 second for each system where the system was zeroed between each test. These graphs are examples of the type of tests necessary to develop a

complete characterization of adaptive force control. These tests can be done for incremental weights over incremental time periods. The software would require additional functionality to steadily record and analyze data at a fast data rate.

- Recommended improvements to circuit board design were discussed in Section 3.4. The main point is to increase the data transfer rate by either changing the micro-controller or GUI code, by purchasing a different type of ADC, or by increasing the processing power of the PC. An additional point of consideration is that connection to a 120 VAC internal power supply as opposed to a separate 5V power supply will decrease the total space requirement of the system and make the system more versatile. This would require the most additional development for the circuit board.
- An EM tracker can be attached to the tool to measure x , y , and z positions and corresponding rotations to increase the data feedback during surgical procedures (Appendix II).

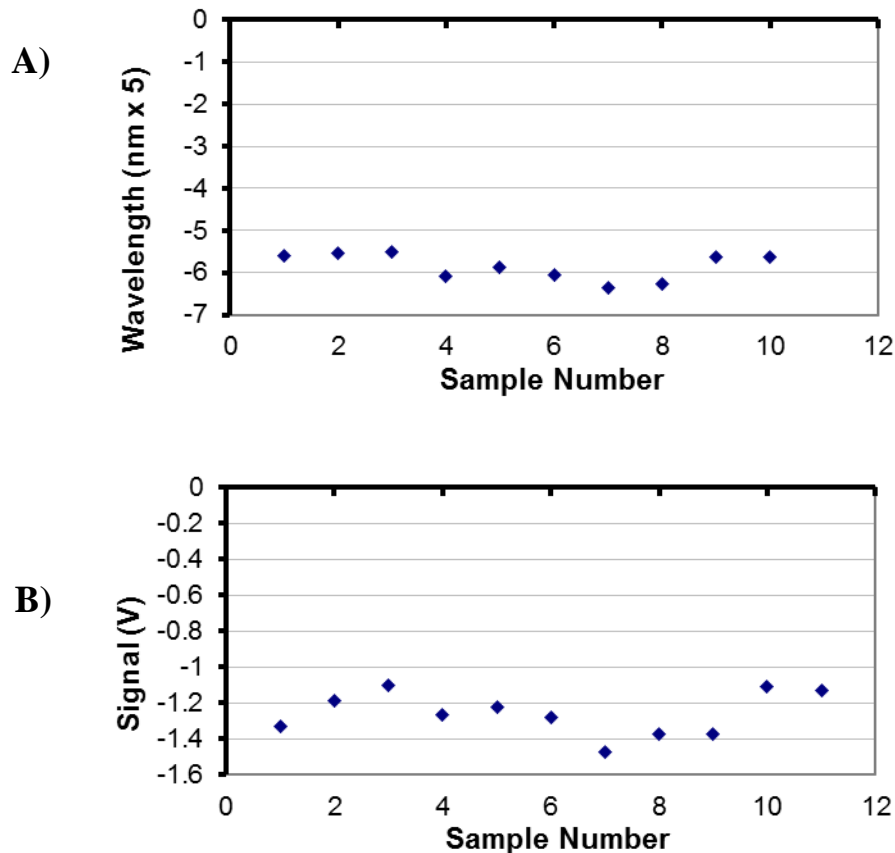


Figure 6.1: 5 N grasping force over 1 second intervals (a) Micron Optics; (b) Low-Cost System.

References

- [1] J. Lozano, C. B. Ma, and W. D. Cannon, “All-inside meniscus repair: a systematic review,” *Clinical Orthopaedics and Related Research*, no. 455, pp. 134–141, 2007.
- [2] S. E. Cameron, W. Wilson, and P. St. Pierre, “A prospective, randomized comparison of open vs. arthroscopically assisted ACL reconstruction,” *Orthopedics*, vol. 18, no. 3, pp. 249–252, 1995.
- [3] M. Ohgami, S. Ishii, Y. Arisawa, T. Ohmori, K. Noga, T. Furukawa, and M. Kitajima, “Scarless endoscopic thyroidectomy: breast approach for better cosmesis,” *Surgical Laparoscopy, Endoscopy & Percutaneous Techniques*,” vol. 10, no. 1, pp. 1–4, February 2000.
- [4] K. H. Fuchs, “Minimally invasive surgery,” *Endoscopy*, vol. 34, no. 2, pp. 154–159, 2002.
- [5] P. Modi, A. Hassan, W. R. Chitwood Jr., “Minimally invasive mitral valve surgery: a systematic review and meta-analysis,” *European Journal of Cardio-thoracic Surgery*, vol. 34, pp. 943–952, 2008.
- [6] Y. Kitagawa, S. Kitano, T. Kubota, K. Kumai, Y. Otani, Y. Saikawa, M. Yoshida, and M. Kitajima, “Minimally invasive surgery for gastric cancer — toward a confluence of two major streams: a review,” *Gastric Cancer*, vol. 8, pp. 103–110, 2005.
- [7] P. J. Kregor, J. A. Stannard, M. Zlowodzki, and P. A. Cole, “Treatment of distal femur fractures using the less invasive - stabilization system surgical experience and early clinical results in 103 fractures,” *J. Orthopedic Trauma*, vol. 18, no. 8, pp. 509–520, 2004.
- [8] J. E. O’Toole, K. M. Eichholz, and R. G. Fessler, “Surgical site infection rates after minimally invasive spinal surgery clinical article”, *Journal of Neurosurgery: Spine*, vol. 11, no. 4, pp. 471–476, 2009.
- [9] D. A. Simpson, N. P. Thomas, P. M. Aichroth, “Open and closed meniscectomy: a comparative analysis,” *The Journal of Bone and Joint Surgery*, vol. 68-B, no. 2, March 1986.
- [10] M. V. Ottermo, M. Øvstedal, T. Langø, Ø. Stavadahl, Y. Yavuz, T. A. Johansen, R. Mårvik, “The role of tactile feedback in laparoscopic surgery,” *Surgical Laparoscopy, Endoscopy & Percutaneous Techniques*, vol. 16, no. 6, pp. 390–400, 2006.
- [11] M. E. H. Eltaib, J. R. Hewit, “Tactile sensing technology for minimal access surgery—a review,” *Mechatronics*, vol. 13, pp. 1163–1177, 2003.
- [12] V. R. Patel, A. S. Tully, R. Holmes and J. Lindsay, “Robotic radical prostatectomy in the community setting—the learning curve and beyond: initial 200 cases,” *The Journal of Urology*, vol. 174, pp. 269–272, 2005.
- [13] A. L. Trejos, A. C. Lyle, A. Escoto, M. D. Naish, and R. V. Patel, “Force/position-based modular system for minimally invasive surgery,” *IEEE Int. Conf. on Robotics and Automation*, Anchorage, AK, pp. 3660–3665, May 2010.
- [14] A. L. Trejos, R. V. Patel, and M. D. Naish, “Force sensing and its application in minimally invasive surgery and therapy: a survey,” *J. Mechanical Engineering Science*, vol. 224, no. 7, pp. 1435–1454, 2010.

- [15] V. Gupta, N. P. Reddy, and P. Batur, "Force in surgical tools: Comparison between laparoscopic and surgical forceps," *Proceedings of the International Conference of the IEEE Engineering in Medicine and Biology Society*, Amsterdam, The Netherlands, pp. 223–224, 1996.
- [16] J. J. Van den Dobbelaer, A. Schooleman, and J. Dankelman, "Friction dynamics of trocars," *Surg. Endosc.*, vol. 21, no. 8, pp. 1338–1343, 2006.
- [17] G. Picod, A. C. Jambon, D. Vinatier, and P. Dubois, "What can the operator actually feel when performing a laparoscopy?" *Surg. Endosc.*, vol. 19, pp. 95–100, 2005.
- [18] W. Sjoerdsma, J. L. Herder, M. J. Horward, A. Jansen, J. J. G. Bannenberg, and C. A. Grimbergen, "Force transmission of laparoscopic grasping instruments," *Minim. Invasive Ther. Allied Technol.*, vol. 6, no. 4, pp. 274–278, 1997.
- [19] P. Puangmali, K. Althoefer, L. D. Seneviratne, D. Murphy, and P. Dasgupta, "State-of-the-art in force and tactile sensing for minimally invasive surgery," *IEEE Sensors Journal*, vol. 8, no. 4, pp. 371–381, 2008.
- [20] J. Rosen, B. Hannaford, M. P. MacFarlane, and M. N. Sinanan, "Force controlled and teleoperated endoscopic grasper for minimally invasive surgery-experimental performance evaluation," *IEEE Trans. Biomedical Engineering*, vol. 46, pp. 1212–1221, 1999.
- [21] G. Tholey, A. Pillarisetti, W. Green, and J. P. Desai, "Design, development, and testing of an automated laparoscopic grasper with 3-D force measurement capability," *Proc. Int. Symp. Medical Simulation*, pp. 38–48, 2004.
- [22] S. Sokhanvar, M. Packirisamy, and J. Dargahi, "A multifunctional pvd-based tactile sensor for minimally invasive surgery," *Smart Materials and Structures*, vol. 16, pp. 989–998, 2007.
- [23] T. Ohtsuka, A. Furuse, T. Kohno, J. Nakajima, K. Yagyu, and S. Omata, "Application of a new tactile sensor to thoracoscopic surgery: Experimental and clinical study," *Ann. Thorac. Surg.*, vol. 60, pp. 610–614, 1995.
- [24] J. Piers, J. Clijnen, D. Reynaerts, H. Van Brussel, P. Herijgers, B. Corteville, and S. Boone, "A micro optical force sensor for force feedback during minimally invasive robotic surgery," *Sensors and Actuators A*, vol. 115, pp. 447–455, 2004.
- [25] X. Liu, I. I. Iordachita, X. He, R. H. Taylor, and J. U. Kang, "Miniature fiber-optic force sensor for vitreoretinal microsurgery based on low-coherence Fabry-Pérot interferometry," *Biomedical Optics Express*, vol. 3, no. 5, pp. 1062–1076, 2012.
- [26] X. He, J. T. Handa, P. L. Gehlbach, R. H. Taylor, and I. I. Iordachita, "A Sub-millimetric 3-DOF Force Sensing Instrument With Integrated Fiber Bragg Grating for Retinal Microsurgery," *IEEE Transactions on Biomedical Engineering*, vol. 61, no. 2, pp. 522–534, 2014.
- [27] X. He, M. A. Balicki, J. U. Kang, P. L. Gehlbach, J. T. Handa, R. H. Taylor, I. I. Iordachita, "Force sensing micro-forceps with integrated fiber Bragg grating for vitreoretinal surgery," *Proc. SPIE Optical Fibers and Sensors for Medical Diagnostics and Treatment Applications XII*, vol. 8218, no. 0W, pp. 1–7, 2012.
- [28] I. Iordachita, Z. Sun, M. Balicki, J. U. Kang, S. J. Phee, J. Handa, P. Gehlbach, R. Taylor, "A sub-millimetric, 0.25 mN resolution fully integrated fiber-optic force-sensing tool for retinal microsurgery," *Int. J. CARS*, vol. 4, pp. 383–390, 2009.

- [29] Z. Sun, M. Balicki, J. Kang, J. Handa, R. Taylor, I. Iordachita, "Development and preliminary data of novel integrated optical micro-force sensing tools for retinal microsurgery," *IEEE Int. Conf. on Robotics and Automation*, Kobe, Japan, pp. 1897–1902, May 2009.
- [30] S. J. Blumenkranz, and D. Q. Larkin, "Force and torque sensing for surgical instruments," US Patent 20070151390 A1, June 2011.
- [31] S. J. Blumenkranz, "Force sensor temperature compensation," US Patent 8561473 B2, October 2013.
- [32] D. Q. Larkin, D. C. Shafer, "Robotic surgery system including position sensors using fiber Bragg gratings," US Patent 20110224689 A1, April 2011.
- [33] E. Hudd, "Optical fiber grating sensors and methods of manufacture," US Patent 20090123111 A1, May 2009.
- [34] V. Mishra, N. Singh, U. Tiwari, and P. Kapur, "Fiber grating sensors in medicine: Current and emerging applications," *Sensors and Actuators A: Physical*, vol. 167, no. 2, pp. 279–290, 2011.
- [35] C. Lu, and Y. Cui, "Fiber Bragg grating spectra in multimode optical fibers," *Journal of Lightwave Technology*, vol. 24, no. 1, pp. 598–604, 2006.
- [36] Sakurambo, "Fiber Bragg grating," *Wikimedia Commons (image)*, July 2008.
- [37] W. W. Morey, G. Meltz, and W. H. Glenn, "Fiber optic Bragg grating sensors," *Proc. SPIE Fiber Optic & Laser Sensors VII*, vol. 1169, pp. 98, 1989.
- [38] A. D. Kersey, M. A. Davis, H. J. Patrick, M. LeBlanc, K. P. Koo, C.G. Askins, M. A. Putnam, and E. J. Friebele, "Fiber grating sensors," *Journal of Lightwave Technology*, vol. 15, no. 8, pp. 1442–63, 1997.
- [39] "Optical properties of fused silica," *suss-microoptics.com*, SUSS MicroOptics, Jan. 2008, Web. April 2015. <http://www.suss-microoptics.com/media/downloads/SMO_TechInfo_Sheet_09.pdf>.
- [40] D. Tosi, M. Olivero, G. Perrone, and A. Vallan, "Improved fibre Bragg grating interrogation for dynamic strain measurement," *Deutsche gesellschaft für angewandte optik*, Torino, Corso Duca degli Abruzzi, 2009.
- [41] M. A. Davis, and A. D. Kersey, "All-fibre Bragg grating strain-sensor demodulation technique using a wavelength division coupler," *Electronics Letters*, vol. 30, no. 1, pp. 75–77, 1994.
- [42] Y. Sano, and T. Yoshino, "Fast optical wavelength interrogator employing arrayed waveguide grating for distributed fiber Bragg grating sensors," *Journal of Lightwave Technology*, vol. 21, no. 1, pp. 132–139, 2003.
- [43] M. A. Davis, and A. D. Kersey, "Matched-filter interrogation technique for fibre Bragg grating arrays," *Electronics Letters*, vol. 31, no. 10, pp. 822–823, 1995.
- [44] Q. Wu, Y. Semenova, A. Sun, P. Wang, and G. Farrell, "High resolution temperature insensitive interrogation technique for FBG sensors," *Optics and Laser Technology*, vol. 42, no. 4, pp. 653–656, 2009.
- [45] R. W. Fallon, L. Zhang, L. A. Everall, J. A. R. Williams, and I. Bennion, "All-fibre optical sensing system: Bragg grating sensor interrogated by a long-period grating," *Measurement Science and Technology*, vol. 9, pp. 1969–1973, 1998.
- [46] H. J. Patrick, G. M. Williams, A. D. Kersey, J. R. Pedrazzani, and A. M. Vengsarkar, "Hybrid fiber Bragg grating/ long period fiber grating sensor for strain/ temperature discrimination," *Photonics Technology Letters*, vol. 8, no. 9, pp. 1223–1225, 1996.

- [47] A. B. L. Ribeiro, L. A. Ferreira, M. Tsvetkov, and J. L. Santos, "All-fibre interrogation technique for fibre Bragg sensors using a biconical fibre filter," *Electronics Letters*, vol. 32, no. 4, pp. 382–383, 1996.
- [48] C. W. Lai, Y. L. Lo, J. P. Yur, W. F. Liu, and C. H. Chuang, "Application of Fabry-Pérot and fiber Bragg grating pressure sensors to simultaneous measurement of liquid level and specific gravity," *Measurement*, vol. 45, pp. 469–473, 2012.
- [49] A. R. Bahrapour, S. Tofighi, M. Bathaee, and F. Farman, "Optical fiber interferometers and their applications," *Interferometry—Research and Applications in Science and Technology*, vol. 1, pp. 3–30, 2012.
- [50] ThorLabs, "Typical S1FC1550 Spectrum", Single Channel, Fiber-Coupled Laser Sources, June 2014, <<http://www.thorlabs.com/search/thorsearch.cfm?search=S1FC1550>>.
- [51] A. Escoto, F. Le Ber, A. L. Trejos, M. D. Naish, R. V. Patel, M. E. LeBel "A knee arthroscopy simulator: design and validation," *IEEE Int. Conf. Engineering Medicine and Biology Society*, Osaka, July 3–7, pp. 5715–8, 2013.

Appendix I: Software Interface

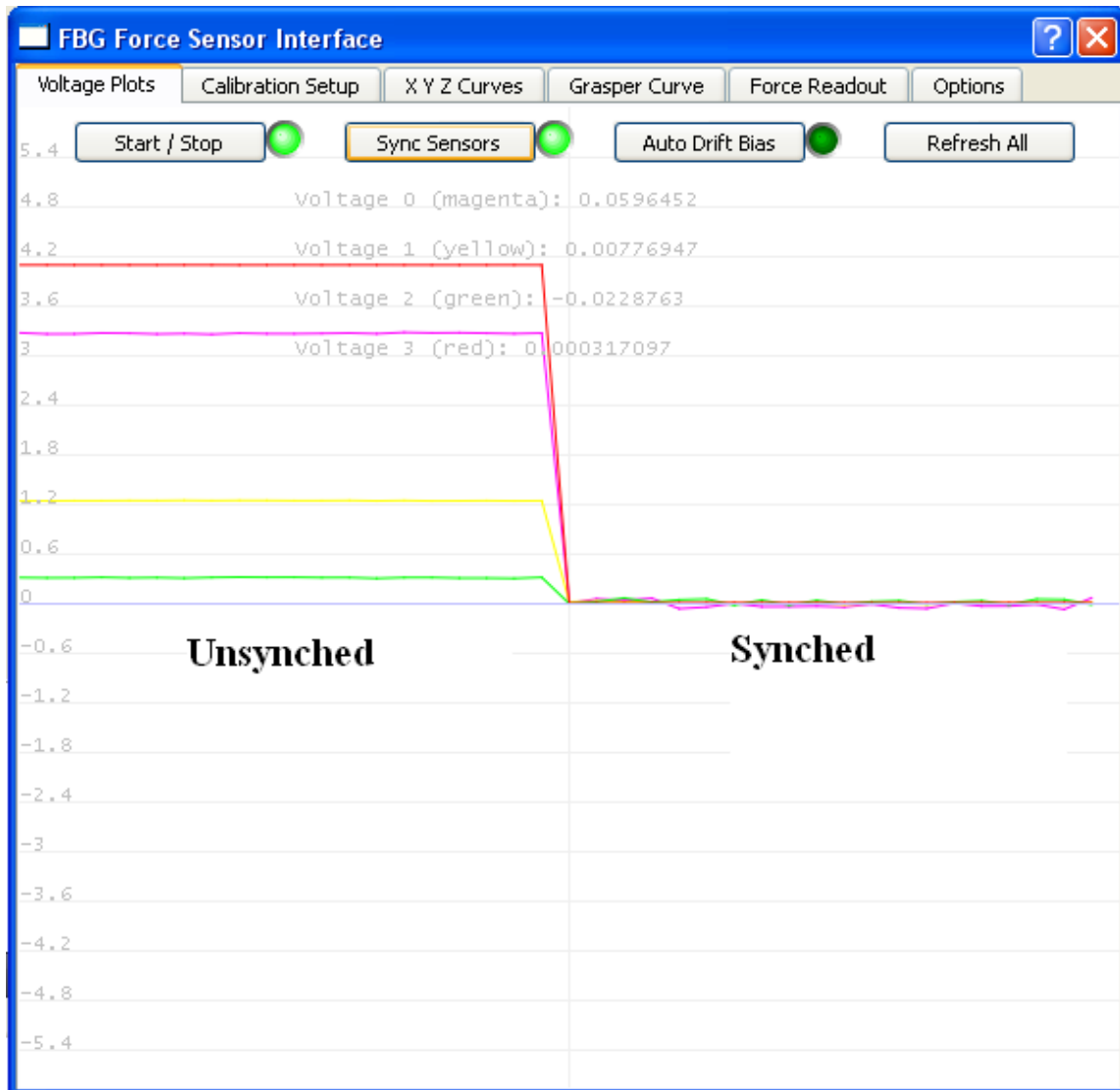


Figure A.1: Raw data voltage plot showing synced vs. unsynced signals.

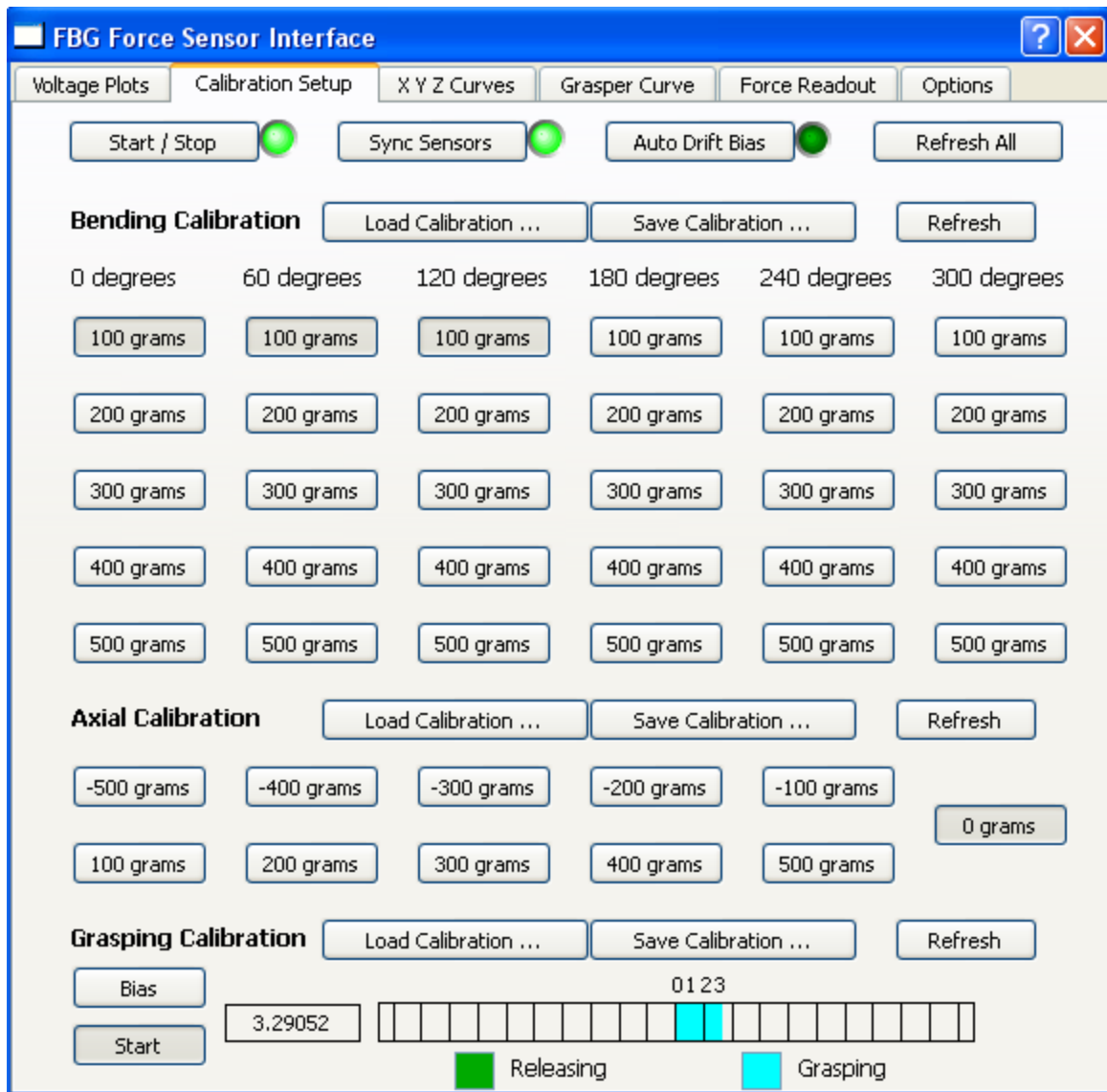


Figure A.2: Bending, axial, and grasping force calibration.

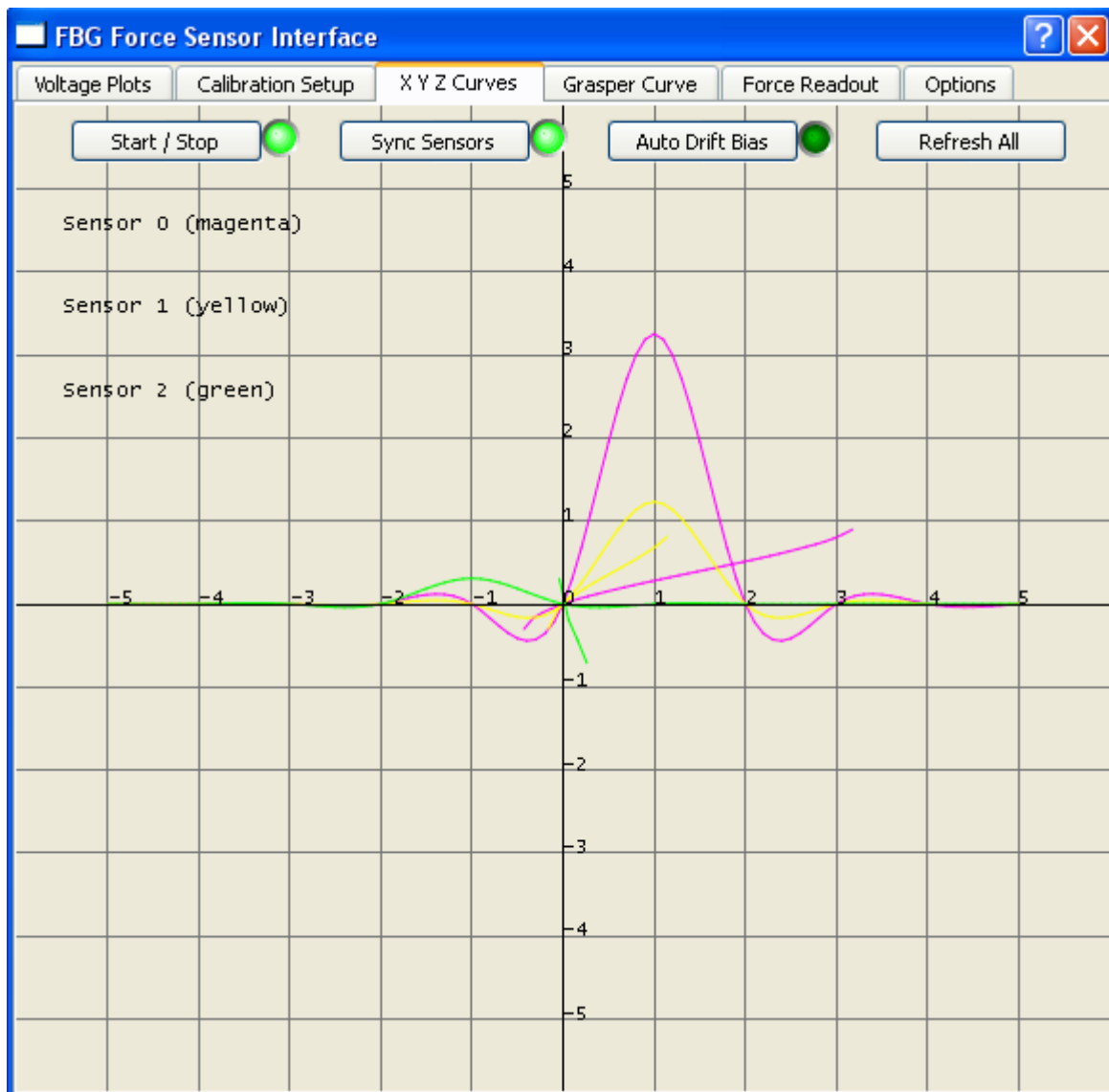


Figure A.3: Bending and axial force calibration curves.
 x: force(N) y: signal (V)

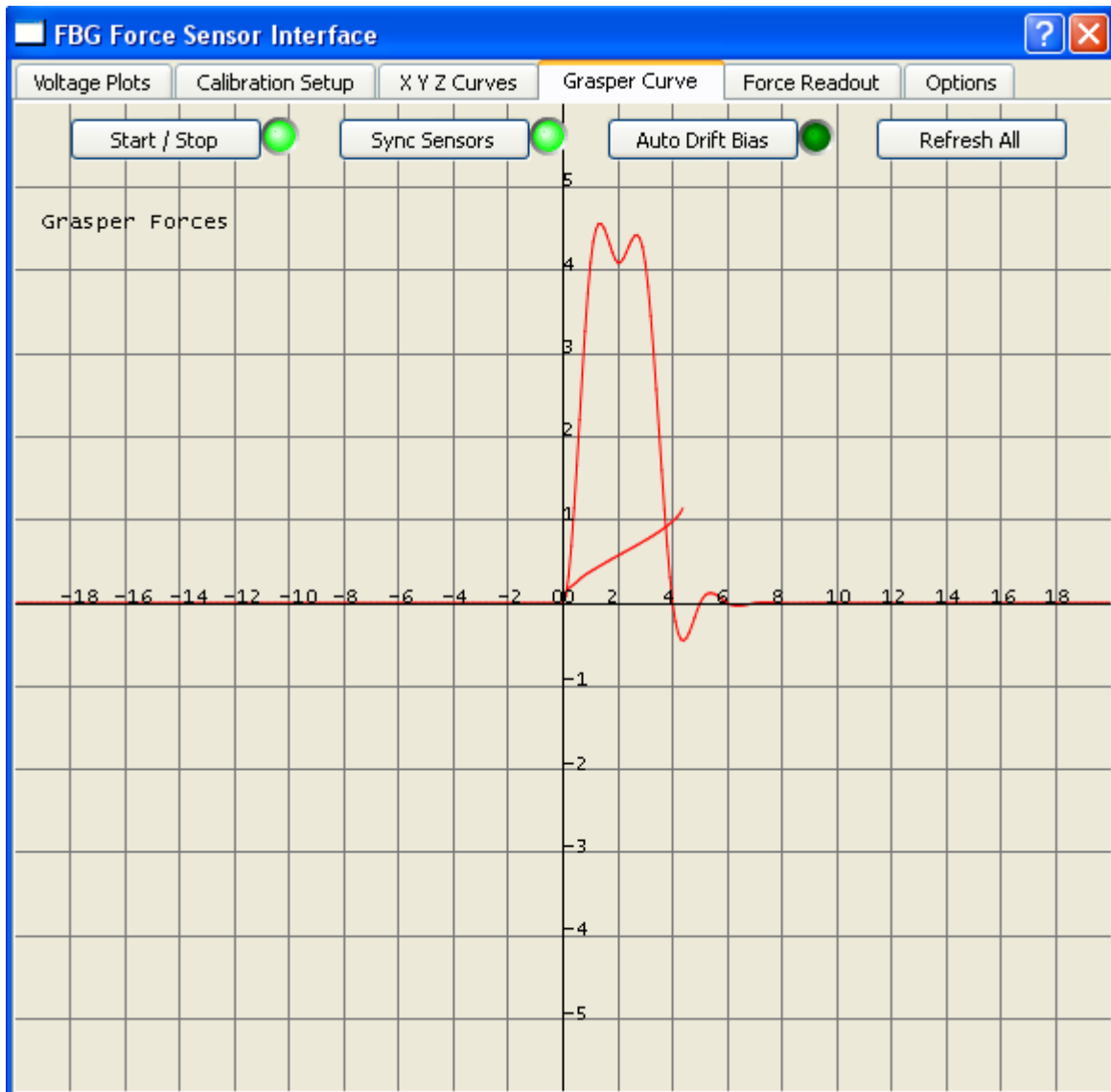


Figure A.4: Grasping force calibration curve.
x: force(N) y: signal (V)

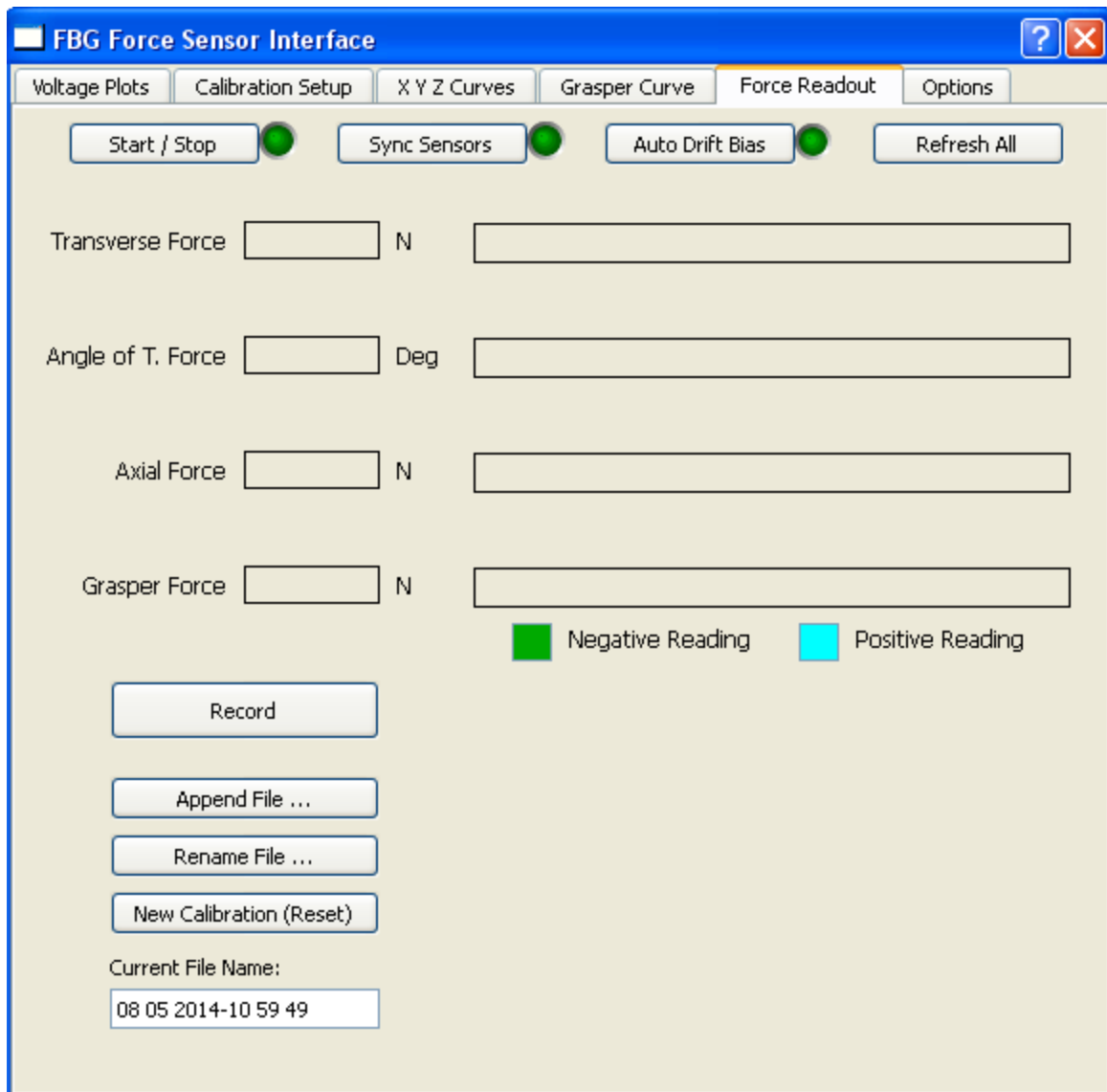


Figure A.5: Visual bar graph force output with recording option.

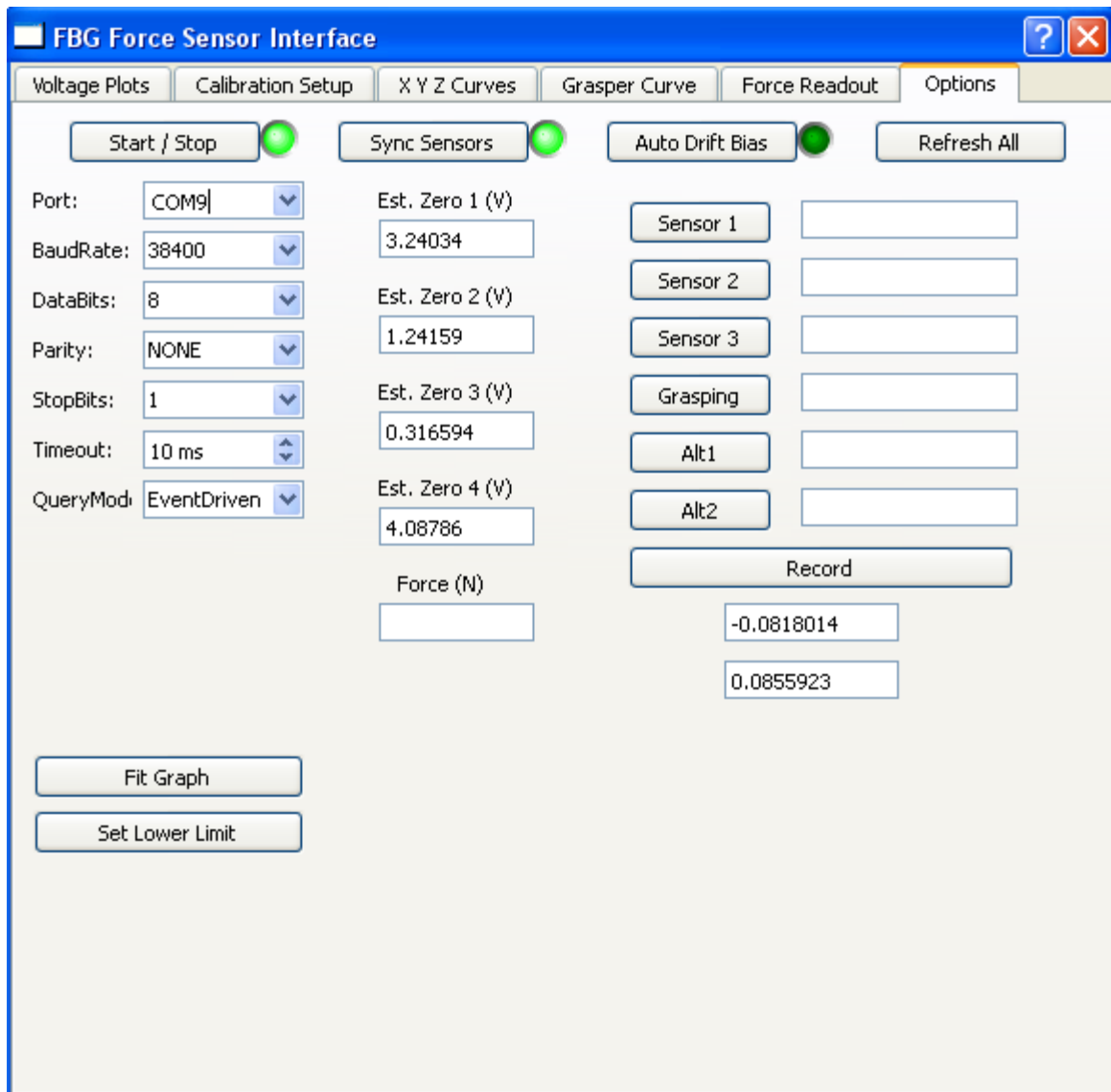


Figure A.6: Additional options for port control and zero estimation.

Appendix II: EM Tracker Design Concept

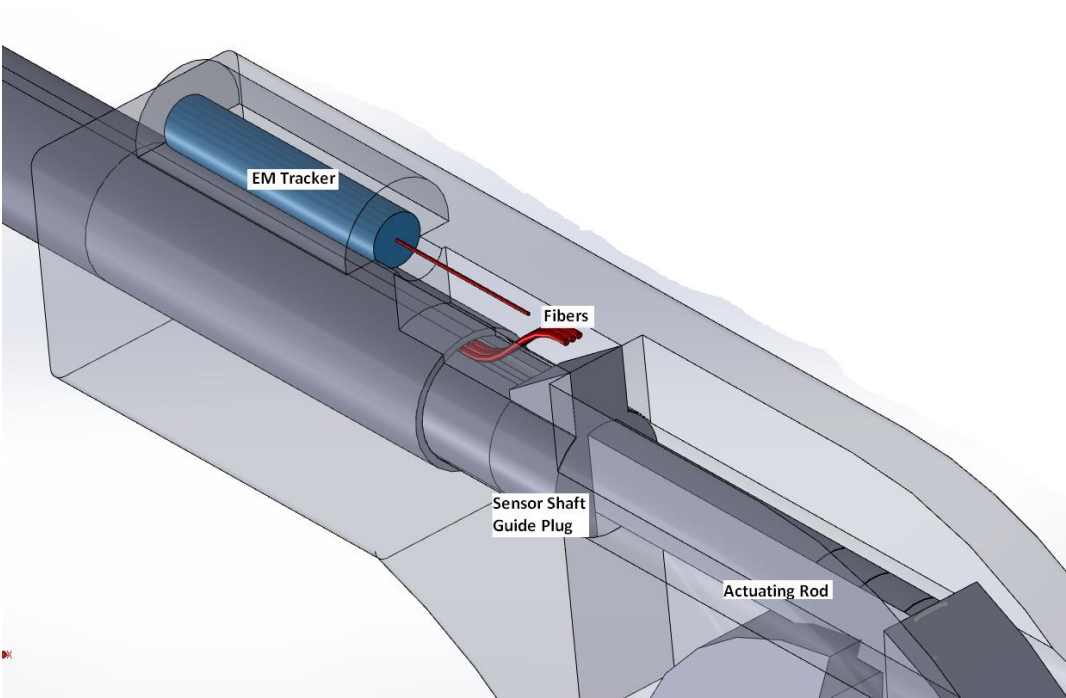


Figure A.7: EM tracker design.

Appendix III: SLD Power and Voltage Curves

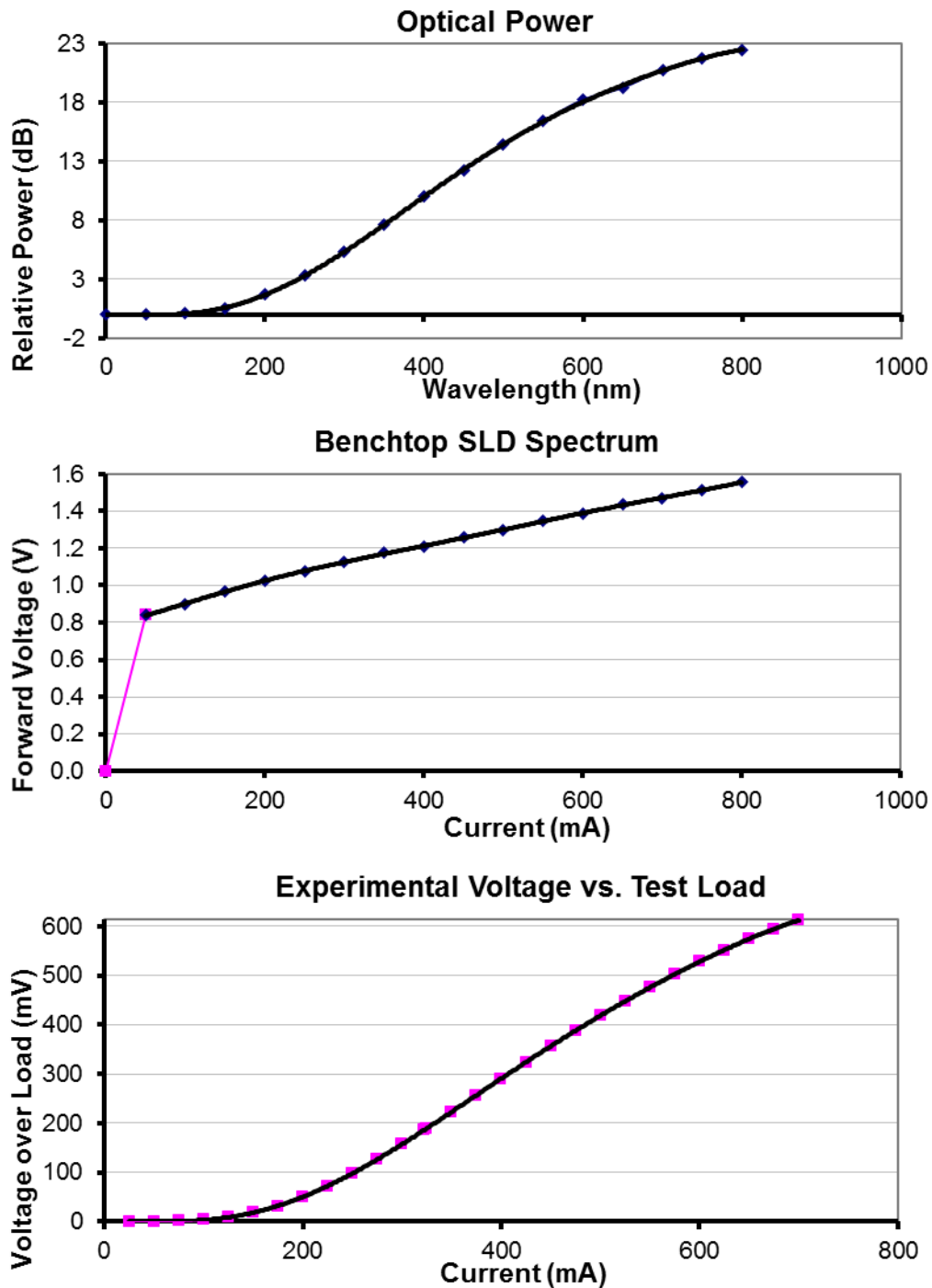


Figure A.8: Benchtop SLD power and voltage curves.

Appendix IV: Material Decision Table

TABLE A.1

BENDING AND SHEAR STRESS MATERIAL ANALYSIS

Bending Stress and Strain

proportional to strain			inversely proportional to strain					
F distrib (N/mm)	d moment (mm)	$\gamma_{NA>fbg}$ (mm)	E (MPa)	Do (mm)	Di (mm)	Strain ($\mu\epsilon$)	Stress (MPa)	Changes
0.1000	44.16	1.98	205,000	4.57	3.45	26.17	5.36	SS, 1/10 N dist load (standard)
0.1000	44.16	1.98	125,000	4.57	3.45	42.91	5.36	Ti
0.0113	44.16	1.98	205,000	4.57	3.45	2.95	0.60	SS, 1/10 N point load
0.1000	44.16	1.98	205,000	4.31	3.45	37.80	7.75	SS, decrease Do
0.1000	54.16	1.98	205,000	4.57	3.45	32.02	6.56	SS, increase d moment
0.1000	54.16	1.98	205,000	4.31	3.45	46.36	9.50	4 & 5
0.1000	44.16	1.98	205,000	4.57	0.00	17.63	3.61	SS, decrease Di to 0
26.0000	44.16	1.98	205,000	4.57	0.00	4583.25	939.57	SS, Fmax, decrease Di to 0
24.0000	44.16	1.98	205,000	4.57	2.45	4611.73	945.41	SS, decrease Di to 2.45
24.0000	44.16	1.98	205,000	4.57	4.05	11041.12	2263.43	SS, increase Di to 4.05
18.0000	44.16	1.98	205,000	4.57	3.45	4699.46	963.39	SS, dist. Load 18N
14.0000	44.16	1.98	205,000	4.57	3.45	3655.13	749.30	SS, dist. Load 14N
10.0000	44.16	1.98	205,000	4.57	3.45	2610.81	535.22	SS, dist. Load 10N
								965 MPa full hard, 760 MPa half hard
							1.55	Deflection @ 18N dist load (mm)
							1.21	Deflection @ 14N dist load (mm)

Shear Stress

0.577 Ys (MPa)	Thickness (mm)	Inertia (mm ⁴)	Area (mm ²)	\bar{Q}	Max Force(N)
118.285	0.3	8.8445	3.84	7.67	41

shear mod = 79.3

F distributed range is 0 to 10N

L grasper is fixed at 8.85 mm

d moment limit is the distance from trocar to tissue

γ_{NA} -> FBG is fixed for machineability of FBG slots

Elastic Modulus is either Stainless Steel or Titanium, however SS is less expensive and strong enough

D outer minimum is failure of the tool under 10 N

D outer maximum is fixed to a 4.5 mm tool size

D inner should be maximized to increase strain, but can go to a minimum of 0

D inner max is fixed to keep room for FBGs

1 $\mu\epsilon$ resolution would need 1 pm wavelength accuracy

Appendix V: Calculation Example using Coupling Biasing

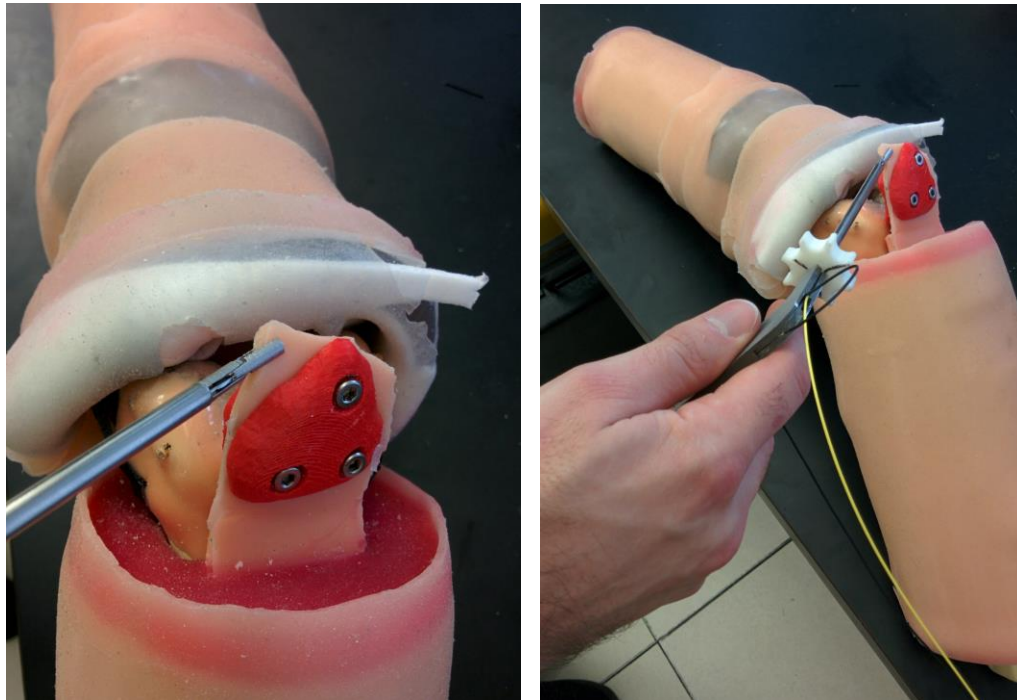


Figure A.9: Tool testing condition on knee simulator.

Description

Figure A.9 shows a sample tissue grasping test on the CSTAR knee simulator [51].

Step One – Apply Forces to Tool and Record Signals

Sensor 1 = 2.28976 (nm × 5)

Sensor 2 = -0.96115 (nm × 5)

Sensor 3 = 1.57362 (nm × 5)

Sensor 4 = -1.4473 (nm × 5)

Step Two – Calculate Grasping Force

Using the sensor 4 reading and the grasper calibration curve in Figure 5.7b:

Grasping Force = 3.7109 N

Step Three – Calculate Coupling Offsets

Using a grasping force of 8.2692 N and the coupling calibration curve in Figure 5.11, the coupling offset errors are:

$$\text{Sensor 1} = 0.7059 \text{ (nm} \times 5\text{)}$$

$$\text{Sensor 2} = 0.4084 \text{ (nm} \times 5\text{)}$$

$$\text{Sensor 3} = 0.3504 \text{ (nm} \times 5\text{)}$$

Step Four – Evaluate Resulting Signals

Subtracting the coupling offsets from the original signals:

$$\text{Sensor 1} = 1.5839 \text{ (nm} \times 5\text{)}$$

$$\text{Sensor 2} = -1.3696 \text{ (nm} \times 5\text{)}$$

$$\text{Sensor 3} = 1.2232 \text{ (nm} \times 5\text{)}$$

Step Five – Calculate Average Axial Force

Converting the resulting signals to Axial Force using the axial calibration curve in Figure 5.10b:

$$\text{Sensor 1} = -7.8484 \text{ N}$$

$$\text{Sensor 2} = 9.5933 \text{ N}$$

$$\text{Sensor 3} = -5.8323 \text{ N}$$

Average Axial Force = -1.362 N (tissue pushing)

Step Six– Evaluate Resulting Signals

To decompose the signals into axial and bending components, the average axial force can be converted into sensor signals and subtracted from the current signals. Using the axial calibration curve, the signals at the specified average axial force of -1.362 N is:

$$\text{Sensor 1} = 0.1989 \text{ (nm} \times 5\text{)}$$

$$\text{Sensor 2} = 0.29718 \text{ (nm} \times 5\text{)}$$

$$\text{Sensor 3} = 0.3088 \text{ (nm} \times 5\text{)}$$

Subtracting these values from the current signals returns the pure bending signals:

Sensor 1 = +1.3850 (nm × 5)

Sensor 2 = +0.9144 (nm × 5)

Sensor 3 = -1.6668 (nm × 5)

Step Seven– Interpolate Bending Forces

Below shows the interpolation results of the bending calibration curves in Figure 5.6. Figure A.10 displays the predicted force and angle bending method.

Bending Force = 2.5508 N

Angle of Force = 71°

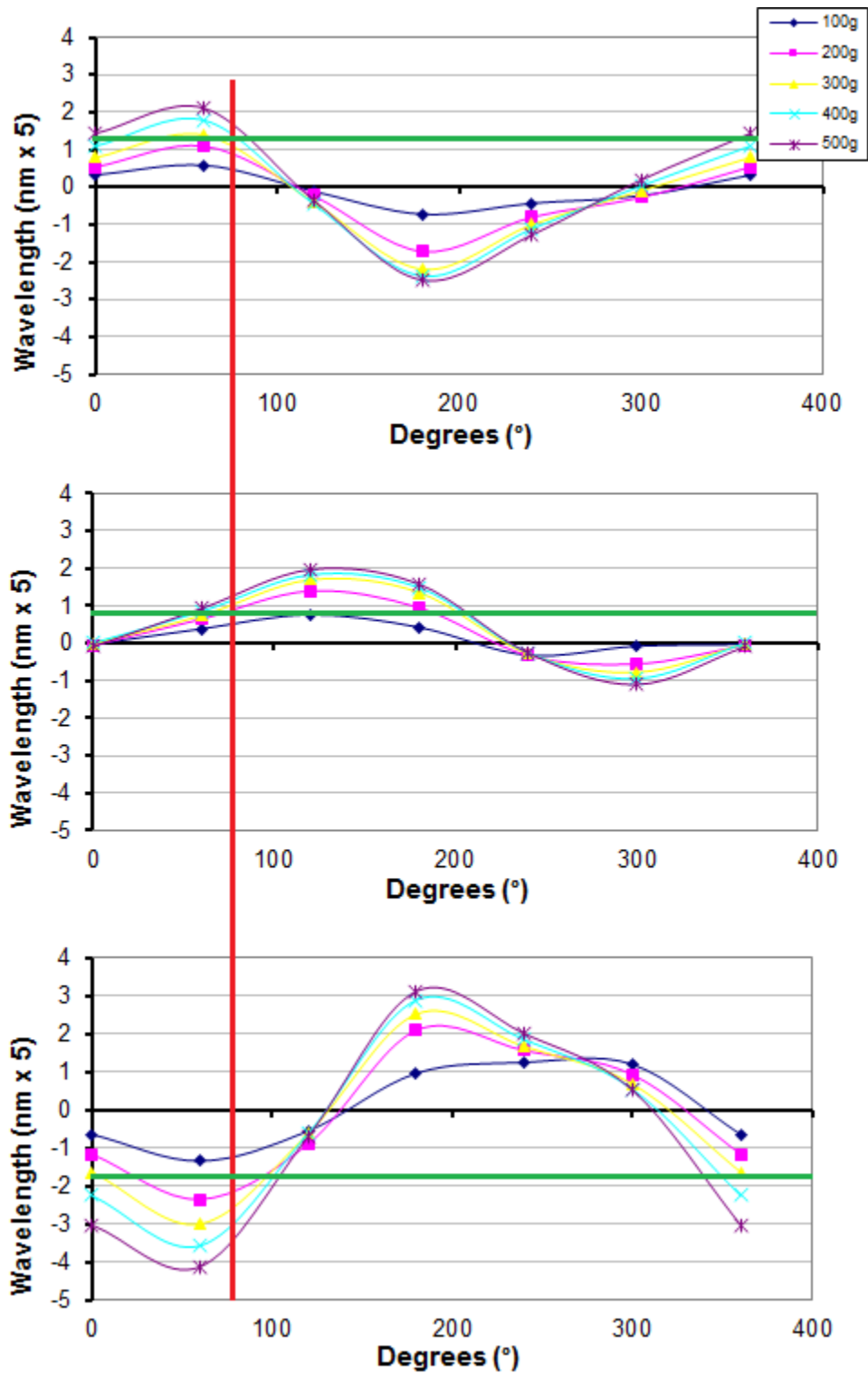


Figure A.10 Predictive bending force technique.

Appendix VI: Permissions and Approvals

The following forms and permission statements are presented in this Appendix:

- Written permission statement from SAGE Publications for Figure 2.1
- Online permission from Springer for Figure 2.2
- Written permission from IOP Publishing for Figure 2.3
 - S. Sokhanvar
- Online permission from Elsevier: Annals of Thoracic Surgery for Figure 2.4
- Online permission from Elsevier: Sensors and Actuators A: Physical for Figure 2.5
- Written permission from OSA: Biomedical Optics Express for Figure 2.6
- Written permission from SPIE for Figures 2.7-8
 - M. A. Balicki
- Online permission from Springer: International Journal of Computer Assisted Radiology and Surgery for Figure 2.9
- Online permission from Wikipedia for Figure 2.10
- Written permission from Daniele Tosi for Figure 2.12
- Online permission from IEEE: Journal of Lightwave Technology for Figure 2.14
 - Figures 2.13, 2.14, 2.15, 2.18, 2.19 are cited in text by IEEE standards
- Free Open Access License Information for Figure 2.16
- Written permission from IOP Publishing for Figure 2.17
 - J. A. R. Williams

Dear Daniel,
Thank you for your email.

Please consider this email as written permission to include figure 3 from the article 'Force sensing and its application in minimally invasive surgery and therapy: a survey.' Form our publication Proceedings of the Institution of Mechanical Engineers, Part C: Journal of Mechanical Engineering Science as part of your forthcoming Master's Thesis.

Please note:

This permission doesn't cover any 3rd party material found in the work.

The author needs to be informed of this reuse.

A full academic reference to the original material needs to be included.

Best Wishes,

Leah Griffiths

Permissions Assistant

SAGE Publications Ltd

1 Oliver's Yard, 55 City Road

London, EC1Y 1SP

UK

www.sagepub.co.uk

SAGE Publications Ltd, Registered in England No.1017514

Los Angeles | London | New Delhi

Singapore | Washington DC

Title: Design, Development, and Testing of an Automated Laparoscopic Grasper with 3-D Force Measurement Capability

Author: Gregory Tholey

Publication: Springer eBook

Publisher: Springer

Date: Jan 1, 2004

Copyright © 2004, Springer-Verlag Berlin Heidelberg

Logged in as:
Daniel Yurkewich

LOGOUT

Order Completed

Thank you very much for your order.

This is a License Agreement between Daniel S Yurkewich ("You") and Springer ("Springer"). The license consists of your order details, the terms and conditions provided by Springer, and the [payment terms and conditions](#).

[Get the printable license.](#)

License Number	3406041093388
License date	Jun 11, 2014
Licensed content publisher	Springer
Licensed content publication	Springer eBook
Licensed content title	Design, Development, and Testing of an Automated Laparoscopic Grasper with 3-D Force Measurement Capability
Licensed content author	Gregory Tholey
Licensed content date	Jan 1, 2004
Type of Use	Thesis/Dissertation
Portion	Figures
Author of this Springer article	No
Original figure numbers	figure 1
Title of your thesis / dissertation	Force Sensing in Arthroscopic Instruments Using Threaded Fiber Bragg Gratings
Expected completion date	Sep 2014
Estimated size(pages)	99
Total	0.00 CAD

CLOSE WINDOW

Copyright © 2014 [Copyright Clearance Center, Inc.](#) All Rights Reserved. [Privacy statement.](#)
Comments? We would like to hear from you. E-mail us at customercare@copyright.com

Dear Daniel Yurkewich,

Thank you for your request to reproduce IOP Publishing material.

Figures 2,3 & 4- Smart Materials and Structures, vol. 16, pp. 989–998, 2007.

We are happy to grant permission for the use you request on the terms set out below.

If you have any questions, please feel free to contact our Permissions team at permissions@iop.org.

I should be grateful if you would acknowledge receipt of this email.

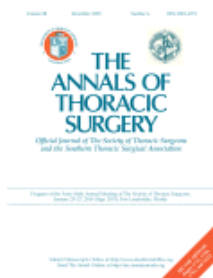
Kind regards,
Lucy Evans
Publishing Assistant
IOP Publishing

Conditions

Non-exclusive, non-transferrable, revocable, worldwide, permission to use the material in print and electronic form will be granted **subject to the following conditions:**

- Permission will be cancelled without notice if you fail to fulfil any of the conditions of this letter.
- You will make reasonable efforts to contact the author(s) to seek consent for your intended use. Contacting one author acting expressly as authorised agent for their co-authors is acceptable.
- You will reproduce the following prominently alongside the material:
 - the source of the material, including author, article title, title of journal, volume number, issue number (if relevant), page range (or first page if this is the only information available) and date of first publication. This information can be contained in a footnote or reference note; or
 - a link back to the article (via DOI); and
 - if practical and IN ALL CASES for works published under any of the Creative Commons licences the words “© IOP Publishing. Reproduced by permission of IOP Publishing. All rights reserved”
- The material will not, without the express permission of the author(s), be used in any way which, in the opinion of IOP Publishing, could distort or alter the author(s)’ original intention(s) and meaning, be prejudicial to the honour or reputation of the author(s) and/or imply endorsement by the author(s) and/or IOP Publishing.
- Payment of £0 is received in full by IOP Publishing prior to use.

Please note: We do not usually provide signed permission forms as a separate attachment. Please print this email and provide it to your publisher as proof of permission.



Title: Application of a new tactile sensor to thoracoscopic surgery: Experimental and clinical study

Author: Toshiya Ohtsuka, Akira Furuse, Tadasu Kohno, Jun Nakajima, Kuniyoshi Yagyū, Sadao Omata

Publication: The Annals of Thoracic Surgery

Publisher: Elsevier

Date: September 1995

Copyright © 1995, Elsevier

Logged in as:
Daniel Yurkewich
Account #: 3000800477

[LOGOUT](#)

Order Completed

Thank you very much for your order.

This is a License Agreement between Daniel S Yurkewich ("You") and Elsevier ("Elsevier"). The license consists of your order details, the terms and conditions provided by Elsevier, and the [payment terms and conditions](#).

[Get the printable license.](#)

License Number	3406540989726
License date	Jun 12, 2014
Licensed content publisher	Elsevier
Licensed content publication	The Annals of Thoracic Surgery
Licensed content title	Application of a new tactile sensor to thoracoscopic surgery: Experimental and clinical study
Licensed content author	Toshiya Ohtsuka, Akira Furuse, Tadasu Kohno, Jun Nakajima, Kuniyoshi Yagyū, Sadao Omata
Licensed content date	September 1995
Licensed content volume number	60
Licensed content issue number	3
Number of pages	5
Type of Use	reuse in a thesis/dissertation
Portion	figures/tables/illustrations
Number of figures/tables/illustrations	1
Format	both print and electronic
Are you the author of this Elsevier article?	No
Will you be translating?	No
Title of your thesis/dissertation	Force Sensing in Arthroscopic Instruments Using Threaded Fiber Bragg Gratings
Expected completion date	Sep 2014
Estimated size (number of pages)	99
Elsevier VAT number	GB 494 6272 12
Permissions price	0.00 USD
VAT/Local Sales Tax	0.00 USD / 0.00 GBP
Total	0.00 USD

[ORDER MORE...](#)

[CLOSE WINDOW](#)



Title: A micro optical force sensor for force feedback during minimally invasive robotic surgery

Author: Jan Peirs,Joeri Clijnen,Dominiek Reynaerts,Hendrik Van Brussel,Paul Herijgers,Brecht Corteville,Sarah Boone

Publication: Sensors and Actuators A: Physical

Publisher: Elsevier

Date: 21 September 2004
Copyright © 2004, Elsevier

Logged in as:
Daniel Yurkewich
Account #:
3000800477

[LOGOUT](#)

Order Completed

Thank you very much for your order.

This is a License Agreement between Daniel S Yurkewich ("You") and Elsevier ("Elsevier"). The license consists of your order details, the terms and conditions provided by Elsevier, and the [payment terms and conditions](#).

[Get the printable license.](#)

License Number	3406541334419
License date	Jun 12, 2014
Licensed content publisher	Elsevier
Licensed content publication	Sensors and Actuators A: Physical
Licensed content title	A micro optical force sensor for force feedback during minimally invasive robotic surgery
Licensed content author	Jan Peirs,Joeri Clijnen,Dominiek Reynaerts,Hendrik Van Brussel,Paul Herijgers,Brecht Corteville,Sarah Boone
Licensed content date	21 September 2004
Licensed content volume number	115
Licensed content issue number	2-3
Number of pages	9
Type of Use	reuse in a thesis/dissertation
Portion	figures/tables/illustrations
Number of figures/tables/illustrations	2
Format	both print and electronic
Are you the author of this Elsevier article?	No
Will you be translating?	No
Title of your thesis/dissertation	Force Sensing in Arthroscopic Instruments Using Threaded Fiber Bragg Gratings
Expected completion date	Sep 2014
Estimated size (number of pages)	99
Elsevier VAT number	GB 494 6272 12
Permissions price	0.00 USD
VAT/Local Sales Tax	0.00 USD / 0.00 GBP
Total	0.00 USD

[ORDER MORE...](#)

[CLOSE WINDOW](#)

Copyright © 2014 [Copyright Clearance Center, Inc.](#) All Rights Reserved. [Privacy statement.](#) Comments? We would like to hear from you. E-mail us at customercare@copyright.com

Dear Mr. Yurkewich,

Thank you for contacting The Optical Society.

OSA considers your requested use of its copyrighted material to be Fair Use under United States Copyright Law. It is requested that a complete citation of the original material be included in any publication.

Let me know if you have any questions.

Kind Regards,

Susannah Lehman

June 18, 2014

Authorized Agent, The Optical Society

Dear Daniel,

Thank you for seeking permission from SPIE to reprint material from our publications. Publisher's permission is hereby granted under the following conditions:

- (1) you obtain permission of one of the authors;
- (2) the material to be used has appeared in our publication without credit or acknowledgment to another source; and
- (3) you credit the original SPIE publication. Include the authors' names, title of paper, volume title, SPIE volume number, and year of publication in your credit statement.

Sincerely,
Karen Thomas for
Eric Pepper, Director of Publications
SPIE
P.O. Box 10, Bellingham WA 98227-0010 USA
360/676-3290 (Pacific Time) eric@spie.org

On 06/26/14, **Marcin Balicki** <marcin@cs.jhu.edu> wrote:
Yes that is fine,
Marcin

On Thu, Jun 26, 2014 at 1:07 PM, Daniel Yurkewich <dyurkewi@uwo.ca> wrote:
Hello Dr. Balicki,
I have contacted SPIE for permission to use Figures 1 and 2 from the following paper in my Masters Thesis at the University of Western Ontario.
X. He, M. A. Balicki, J. U. Kang, P. L. Gehlbach, J. T. Handa, R. H. Taylor, I. I. Iordachita, "Force sensing micro-forceps with integrated fiber Bragg grating for vitreoretinal surgery," *Proc. SPIE Optical Fibers and Sensors for Medical Diagnostics and Treatment Applications XII*, vol. 8218, no. 0W, pp. 1–7, 2012.

They have provided permission on the condition that I get permission from an author. Would you be kind enough to provide me with this permission?

Sincerely,
Daniel Yurkewich



Title: A sub-millimetric, 0.25 mN resolution fully integrated fiber-optic force-sensing tool for retinal microsurgery

Author: Iulian Iordachita

Publication: International Journal of Computer Assisted Radiology and Surgery

Publisher: Springer

Date: Jan 1, 2009

Copyright © 2009, CARS

Logged in as:
Daniel Yurkewich
Account #:
3000800477

[LOGOUT](#)

Order Completed

Thank you very much for your order.

This is a License Agreement between Daniel S Yurkewich ("You") and Springer ("Springer"). The license consists of your order details, the terms and conditions provided by Springer, and the [payment terms and conditions](#).

[Get the printable license.](#)

License Number	3406610987444
License date	Jun 12, 2014
Licensed content publisher	Springer
Licensed content publication	International Journal of Computer Assisted Radiology and Surgery
Licensed content title	A sub-millimetric, 0.25 mN resolution fully integrated fiber-optic force-sensing tool for retinal microsurgery
Licensed content author	Iulian Iordachita
Licensed content date	Jan 1, 2009
Volume number	4
Issue number	4
Type of Use	Thesis/Dissertation
Portion	Figures
Author of this Springer article	No
Original figure numbers	1, 5
Title of your thesis / dissertation	Force Sensing in Arthroscopic Instruments Using Threaded Fiber Bragg Gratings
Expected completion date	Sep 2014
Estimated size(pages)	99
Total	0.00 CAD

[CLOSE WINDOW](#)

Copyright © 2014 [Copyright Clearance Center, Inc.](#) All Rights Reserved. [Privacy statement.](#) Comments? We would like to hear from you. E-mail us at customercare@copyright.com

Summary

Description	A diagram of a Fiber Bragg Grating. The image shows the structure of a positive-only index change Fiber Bragg Grating. The refractive index profile of the fiber core shows the change of the refractive index along the core. The spectral response on the Fiber Bragg Grating shows how the incident broadband signal is split into the transmitted and reflected components, about the Bragg wavelength.
Source	Vectorized version of Image:Fbg.GIF
Date	2008-07-02
Author	Sakurambo
Permission <small>(Reusing this file)</small>	Original image FBG.GIF was released under a GFDL license
Other versions	* Image:Fbg.GIF <ul style="list-style-type: none">• File:Fiber Bragg Grating.svg is a language neutral version at commons

Licensing:



Permission is granted to copy, distribute and/or modify this document under the terms of the **GNU Free Documentation License**, Version 1.2 or any later version published by the Free Software Foundation; with no Invariant Sections, no Front-Cover Texts, and no Back-Cover Texts.



This work is licensed under the [Creative Commons Attribution-ShareAlike 3.0 License](#).
This licensing tag was added to this file as part of the [GFDL licensing update](#).

Hi Daniel,

[...]

Of course I give you permission to use the image and generally, all images on published papers as they're available for disclosure.

[...]

Daniele Tosi, PhD

University of Limerick
Electronic and Computer Engineering (ECE), Room E2-004
Ireland
<http://www.ofsrc.ul.ie/>

E-mail: daniele.tosi@ul.ie [or sirddt@gmail.com]
Phone: +353 (0) 87 6086787; +39 329 2071297 (ITA); +44 (0)7 415 659 163 (UK)
Skype: dan82ddt
Slideshare: <http://www.slideshare.net/SirDDT>



Title: Fast optical wavelength interrogator employing arrayed waveguide grating for distributed fiber Bragg grating sensors

Author: Sano, Y.; Yoshino, T.

Publication: Lightwave Technology, IEEE/OSA Journal of

Publisher: IEEE

Date: Jan 2003

Copyright © 2003, IEEE

Logged in as:
Daniel Yurkewich
Account #:
3000800477

LOGOUT

Thesis / Dissertation Reuse

The IEEE does not require individuals working on a thesis to obtain a formal reuse license, however, you may print out this statement to be used as a permission grant:

Requirements to be followed when using any portion (e.g., figure, graph, table, or textual material) of an IEEE copyrighted paper in a thesis:

- 1) In the case of textual material (e.g., using short quotes or referring to the work within these papers) users must give full credit to the original source (author, paper, publication) followed by the IEEE copyright line © 2011 IEEE.
- 2) In the case of illustrations or tabular material, we require that the copyright line © [Year of original publication] IEEE appear prominently with each reprinted figure and/or table.
- 3) If a substantial portion of the original paper is to be used, and if you are not the senior author, also obtain the senior author's approval.

Requirements to be followed when using an entire IEEE copyrighted paper in a thesis:

- 1) The following IEEE copyright/ credit notice should be placed prominently in the references: © [year of original publication] IEEE. Reprinted, with permission, from [author names, paper title, IEEE publication title, and month/year of publication]
- 2) Only the accepted version of an IEEE copyrighted paper can be used when posting the paper or your thesis on-line.
- 3) In placing the thesis on the author's university website, please display the following message in a prominent place on the website: In reference to IEEE copyrighted material which is used with permission in this thesis, the IEEE does not endorse any of [university/educational entity's name goes here]'s products or services. Internal or personal use of this material is permitted. If interested in reprinting/republishing IEEE copyrighted material for advertising or promotional purposes or for creating new collective works for resale or redistribution, please go to http://www.ieee.org/publications_standards/publications/rights/rights_link.html to learn how to obtain a License from RightsLink.

If applicable, University Microfilms and/or ProQuest Library, or the Archives of Canada may supply single copies of the dissertation.

BACK

CLOSE WINDOW

Title: High resolution temperature insensitive interrogation technique for FBG sensors
Authors: Q. Wu, Y. Semenova, A. Sun, P. Wang, and G. Farrell
Date: January 1st, 2009
License Location: <http://creativecommons.org/licenses/by-nc-sa/3.0/legalcode>
License Summary Location: <http://creativecommons.org/licenses/by-nc-sa/3.0/>

Changes: No changes were made to the Figure.

This Article is brought to you for free and open access by the School of Electronic and Communications Engineering at ARROW@DIT. It has been accepted for inclusion in Articles by an authorized administrator of ARROW@DIT. For more information, please contact yvonne.desmond@dit.ie, arrow.admin@dit.ie.



This work is licensed under a [Creative Commons Attribution-Noncommercial-Share Alike 3.0 License](http://creativecommons.org/licenses/by-nc-sa/3.0/)

Dear Daniel Yurkewich,
Thank you for your request to reproduce IOP Publishing material.

Figures 2 & 3- “All-fibre optical sensing system: Bragg grating sensor interrogated by a long-period grating,”
Measurement Science and Technology, vol. 9, pp. 1969–1973, 1998

We are happy to grant permission for the use you request on the terms set out below.

If you have any questions, please feel free to contact our Permissions team at permissions@iop.org.

I should be grateful if you would acknowledge receipt of this email.

Kind regards,
Lucy Evans
Publishing Assistant
IOP Publishing

Conditions

Non-exclusive, non-transferrable, revocable, worldwide, permission to use the material in print and electronic form will be granted **subject to the following conditions:**

- Permission will be cancelled without notice if you fail to fulfil any of the conditions of this letter.
- You will make reasonable efforts to contact the author(s) to seek consent for your intended use. Contacting one author acting expressly as authorised agent for their co-authors is acceptable.
- You will reproduce the following prominently alongside the material:
 - the source of the material, including author, article title, title of journal, volume number, issue number (if relevant), page range (or first page if this is the only information available) and date of first publication. This information can be contained in a footnote or reference note; or
 - a link back to the article (via DOI); and
 - if practical and IN ALL CASES for works published under any of the Creative Commons licences the words “© IOP Publishing. Reproduced by permission of IOP Publishing. All rights reserved”
- The material will not, without the express permission of the author(s), be used in any way which, in the opinion of IOP Publishing, could distort or alter the author(s)’ original intention(s) and meaning, be prejudicial to the honour or reputation of the author(s) and/or imply endorsement by the author(s) and/or IOP Publishing.
- Payment of £0 is received in full by IOP Publishing prior to use.

Please note: We do not usually provide signed permission forms as a separate attachment. Please print this email and provide it to your publisher as proof of permission.

Dear Daniel,

The copyright of the figure is assigned to the IOP. You would therefore need to contact them to get permission to reproduce. There is information on how to do this at

<http://iopscience.iop.org/page/copyright>

Regards,
Dr. John Williams

CURRICULUM VITAE

Name: Daniel Yurkewich

**Post-secondary
Education and
Degrees:** Waterloo University
Waterloo, Ontario, Canada
2007 – 2008
Advanced Honours Mathematics

McMaster University
Hamilton, Ontario, Canada
2008 – 2012 B.Eng.
Mechanical Engineering

The University of Western Ontario
London, Ontario, Canada
2012 – 2015 M.E.Sc.
Electrical and Computer Engineering

Honours and Awards: Outstanding Presentation in ECE Graduate Symposium, Western, 2013
Suma Cum Laude, McMaster University, 2012
University Senate Scholarship, Waterloo, ON, Canada, 2007
National Renee Descartes Scholarship, Waterloo, ON, Canada, 2007
Waterloo Entrance Scholarship, Waterloo, ON, Canada, 2007

**Related Work
Experience:** Teaching Assistant
The University of Western Ontario
2012 -2013

Research Associate
Canadian Surgical Technologies and Advanced Robotics
2012 – 2015

Relevant Publications:

D. S. Yurkewich, A. Escoto, A. L. Trejos, M. E. LeBel, R. V. Patel, M. D. Naish, “Low-Cost Force-Sensing Arthroscopic Tool Using Threaded Fiber Bragg Grating Sensors,” *IEEE/RAS-EMBS International Conference on Biomedical Robotics and Biomechatronics*, São Paulo, Brazil, August 12–15, pp. 28–33, 2014.

B. Poursartip, D. Yurkewich, M. E. LeBel, R. V. Patel, A. L. Trejos, M. D. Naish, “Performance Evaluation of a Sensorized Arthroscopic Grasper,” Submitted for the *Dynamic Systems and Control Conference*, Columbus, Ohio, October 28–30, 2015.